PEMFC non-invasive data-based diagnosis through external magnetic field measurements

Ali Bawab

▶ **To cite this version:**

Ali Bawab. PEMFC non-invasive data-based diagnosis through external magnetic field measurements. Other. Université Bourgogne Franche-Comté, 2022. English. NNT : 2022UBFCA013 . tel-04524732

HAL Id: tel-04524732
https://theses.hal.science/tel-04524732

Submitted on 28 Mar 2024

HAL is a multi-disciplinary open access archive for the deposit and dissemination of scientific research documents, whether they are published or not. The documents may come from teaching and research institutions in France or abroad, or from public or private research centers.

L'archive ouverte pluridisciplinaire **HAL**, est destinée au dépôt et à la diffusion de documents scientifiques de niveau recherche, publiés ou non, émanant des établissements d'enseignement et de recherche français ou étrangers, des laboratoires publics ou privés.

THESE DE DOCTORAT DE L'ETABLISSEMENT UNIVERSITE BOURGOGNE FRANCHE-COMTE

PREPAREE A L'UNIVERSITE DE TECHNOLOGIE DE BELFORT-MONTBELIARD

Ecole doctorale n°ED37

ED SPIM

Doctorat de Génie électrique

Par

Ali Bawab

PEMFC Non-invasive Data-Based Diagnosis Through External Magnetic Field Measurements

Thèse présentée et soutenue à Belfort, le 25/11/2022

Composition du Jury :

Pr. Vincent LANFRANCHI	Professeur, Sorbonne Université/UTC, Roberval	Rapporteur
Pr. Bultel Yann	Professeur, INP Grenoble, LEPMI	Rapporteur
Pr. Melika Hinaje	Professeur, Université de Lorraine, GREEN	Examinateur
Dr. Sébastien ROSINI	Ingénieur R&D, CEA	Examinateur
Pr. Daniel Depernet	MCF, HDR, UTBM, FEMTO-ST	Directeur de thèse
Dr. Stefan Giurgea	MCF, UTBM, FEMTO-ST	Codirecteur de thèse
Pr. Daniel Hissel	Professeur, UFC, IUF, FEMTO-ST	Codirecteur de thèse

Thèse de doctorat préparée à l'Institut FEMTO-ST, UMR CNRS 6174

ACKNOWLEDGEMENTS

This work is probably the most enriching experience for me scientifically and humanly because it allowed me to meet many people from different horizons and disciplines who have marked me in their own way by their compassion, their helpfulness and their good mood. Thus, the work that has been done is thanks to all the people I have met closely or from afar / at work, during this three-year period. I would also like to thank the members of my team with whom I spent most of my time during these three years, whether it was in meetings, manipulations or in the office.

I start with Mr. Stefan geuirgea, my thesis co-supervisor and research doctor at FCLAB. I will not forget your availability about instrumentation, measurements and different scenarios we imagined to validate the models. In addition to this scientific aspect, you were available to cheer up with a good mood. I also thank Mr. Daniel depernet, my thesis supervisor and research professor in FCLAB for all the ideas that you proposed to us to advance the work. Without forgetting Mr. Daniel hissel my co-supervisor and university professor at the University of Franche Compté for having trusted me to be one of his team (SHARPAC). Thank you for all your explanation on how we can place the approach in its industrial context based on your solid background in this domain. In addition, I would like to thank Vincent lanfranchi university professor at Sorbonne University and Yunn bultel university professor at Grenoble INP, for having read and reported this thesis, bringing all the questions and the possible precisions to make it relevant and original. I would like to thank my three intern students (Hugues Riberolles, Loqmane Recham, and Mattéo GANTZER) for your robust help in building up the experimental test bench and make all the measurements needed during my three years.

I continue to thank all those who, apart from the laboratory, make Belfort one of the most pleasant cities to live in. Thank you Hachem, the kitchen genius and incredible engineer. Thank you Mira the future optimization doctor for your good communicative mood and for your support. Thank you Rim the future agriculture doctor for setting the mood. Thank you friends for all the nice exchanges we had.

Before finishing with my family, I would give a special thanks to the future biology doctor, my partner Lama. Thank you for being beside me since the day I know you. Thank you for your unlimited support to make me feel well and happy, thank you very much.

Finally, I thank the people, who have always been there since my birth, my dear parents Majed and Maha, for the sacrifices you have made for to bring us the best education and push us to succeed. I would like to thank my brother and my sisters (Bilal, Nour, Fatima, and Aya) for their support and especially my brother who will soon become a doctor in the field of electrochemistry.

ABSTRACT

The normal and abnormal behavior of fuel cells can be determined by their internal current density distribution. Magneto tomography is applied to localize the 3D fault position by studying the external magnetic field around the stack, which is produced by the current density flow inside each cell of the stack. To evaluate the external magnetic field distribution, in this work we propose a new design of the magnetic field analyzer. This analyzer amplifies the magnetic field around the cell to perform an accurate detection of the fault position. This work focuses on 3D multi physical modeling and experimental validation of the magnetic field during operation of a polymer electrolyte membrane fuel cell emulator. A new concept of polymer electrolyte membrane fuel cell emulator has been especially designed to emulate the magnetic field of a real fuel cell stack. This emulator has been simulated and tested experimentally to prove the ability of the system in detecting 3D fault.
As a main branch of data-driven fault diagnosis, this work also deals with an offline fault diagnosis of 2D polymer electrolyte membrane fuel cell stack emulator. A data-driven strategy is proposed for this emulator diagnosis. This strategy, features are extracted from the external magnetic field at the ferromagnetic circuit analyzer level which is produced by the experimental design of the current density flow variation inside the stack emulator. In the proposed approach, a set of feature extraction and classification models in machine learning were used to recognize the system diagnosis accuracy. This work focuses on an experimental and numerical training datasets. The proposed diagnosis strategies has been verified using the experimental data which covers a set of representative faults of the fuel cell.

Key words: Fuel cell, Magnetic field, Fault Diagnosis, Multi physical coupling, Experimental designs, Feature extraction, Classification

RÉSUMÉ

Le comportement normal et anormal des piles à combustible peut être déterminé par la distribution de leur densité de courant interne. La magnéto tomographie est appliquée pour localiser la position du défaut en 3D en étudiant le champ magnétique externe autour de la pile, qui est produit par le flux de densité de courant à l'intérieur de chaque cellule de la pile. Pour évaluer la distribution du champ magnétique externe, nous proposons dans ce travail une nouvelle conception de l'analyseur de champ magnétique. Cet analyseur amplifie le champ magnétique autour de la cellule pour effectuer une détection précise de la position du défaut. Ce travail se concentre sur la modélisation multi physique 3D et la validation expérimentale du champ magnétique pendant le fonctionnement d'un émulateur de pile à combustible à membrane électrolyte polymère. Un nouveau concept d'émulateur de pile à combustible à membrane électrolyte polymère a été spécialement conçu pour émuler le champ magnétique d'une pile à combustible réelle. Cet émulateur a été simulé et testé expérimentalement pour prouver la capacité du système à détecter les défauts 3D.
En tant que branche principale du diagnostic de panne piloté par les données, ce travail traite également du diagnostic de panne hors ligne d'un émulateur de pile à combustible 2D à membrane électrolyte polymère. Une stratégie basée sur les données est proposée pour le diagnostic de cet émulateur. Dans cette stratégie, les caractéristiques sont extraites du champ magnétique externe au niveau de l'analyseur de circuit ferromagnétique qui est produit par le plan expérimental de la variation du flux de densité de courant à l'intérieur de l'émulateur de pile. Dans l'approche proposée, un ensemble de modèles d'extraction de caractéristiques et de classification en apprentissage automatique a été utilisé pour reconnaître différentes singularités de densité de courant. Ce travail se concentre sur un ensemble de données d'entraînement expérimentales et numériques. Les stratégies de diagnostic proposées ont été vérifiées en utilisant les données expérimentales qui couvrent un ensemble de défauts. représentatifs de la pile à combustible.

Mots clés: Pile à combustible, champ magnétique, diagnostic de panne, couplage physique multiple, plans d'expérience, extraction de caractéristiques, classification.

TABLE OF CONTENTS

ILLUSTRATIONS

TABLES

GENERAL INTRODUCTION

Hydrogen is becoming undeniable energy and can replace the conventional fossil sources. Indeed, these sources almost cover 80 percent of the word energy use and considered as the main factors of the greenhouse effects. On another hand, the emissions of the electrochemical reactions involving hydrogen do not produce greenhouse gases. In addition, hydrogen is reasonable by its abundance and high energy density compared to the fossil fuel sources. Hence, most of the current technologies consider hydrogen energy in their advanced applications. Fuel cell in its various forms covers the most industrially advanced uses in hydrogen energy applications. Despite of their advantages for energy storage and conversion, these systems are still suffering from certain imperfections. Among different types of the fuel cells, Proton Exchange Membrane Fuel Cell (PEMFC) is the mostly used type and has interesting performance for an embedded and transportation applications. However, cost, and reliability and durability are still the obstacles which inadequate the PEMFC process. To improve the system operation using PEM fuel cells, the reliability and durability of the cell could be increased by an efficient and early fault diagnostic. To do so, several techniques are developed and classified according to their diagnostic efficiency while not disturbing the operating of the fuel cell systems. These sophisticated methods can be separated into two broad categories: "invasive methods" and "non-invasive methods". The measurement of the external magnetic field appears to be a significant indicator of the health of the stack. The advantage of this non-invasive tool is that it provides a lot of information about the internal condition of a fuel cell stack. Thus, analysis of a differential measurement of the external magnetic field relative to a healthy reference can characterize abnormal PEMFC operation. Most previous studies focus on mapping the current draw from external magnetic field measurements. Identifying the internal current distribution inside the fuel cell using the external magnetic field measurements is sorted to direct and indirect models. Most of the existing direct models uses multi-physical coupling on a specific number of cells. In addition, the indirect model characterized by a complex mathematical problem with a rarely unique solution and extremely sensitive to the measurement's errors. On another hand, feature extraction and classification in data-driven diagnosis have shown their superiority in fault diagnosis in the last two decades. In [1], this approach is based on original variables like individual cell voltages to identify the water managements faults (flooding, drying). In addition, using the external magnetic field difference obtained in the data-driven diagnosis strategy can identify the fault position inside the stack.

The research work of ISITE PEM-DIMAG project carried by the FEMTO-ST (Energy department) chosen through this work and others already completed to develop a non-invasive diagnosis method based on the external magnetic field measurements. The new diagnostic tool proposed here is based on optimization and development of the magnetic field measurements system based on existing prototype implemented by FCLAB. The main contribution of this work is represented by a 3D current density emulator of a PEMFC. Supplied by a current source, this emulator reproduces an equivalent current distribution in a similar geometrical domain, as the current distribution inside a Fuel Cell domain, during steady state operation. The magnetic field generated by the current distribution in the emulator will also reproduce the magnetic field of a real FC. Multi physical modeling of a FC

involving couplings between electrochemical, electric and magneto static models has been realized in normal and faulty operation and integrated in the physical description of the emulator regions. Then an updated design for the magnetic field analyzer and the methodology have been validated for realistic 3D local faults inside the FC stack emulator. The novelty of the method explained in this work is the ability to detect the local and global fault position inside the stack.

This work is divided into three main parts: After a literature state of arts, the third part explains in detail the 3D current density emulator of a PEMFC. The third part applies data based diagnosis algorithm on the external magnetic experimental and numerical datasets. In the last part, a new geometrical design of the magnetic analyzer is proposed and optimized with respect to the geometrical parameters according to the external magnetic field produced. Around these three parts, four chapters will be presented.

In the first chapter, the PEMFC technologies and systems are introduced. The diagnosis methods for PEMFC are also reviewed. The dependence of the current density distribution on the fault is then highlighted. We detail the interest of the magnetic field measurements for the detection of failures likely occur inside these systems. In addition, we state most of the diagnosis methods by classifying them into "invasive" and "non-invasive" techniques.

Chapter 2 represents the updated circuit analyzer design with various fuel cell emulator models which explains the current density distribution inside the fuel cell. First, we present the multi-physical modeling by a Finite Element Model (FEM) that made it possible to determine the 2D and 3D homogeneous and heterogeneous current flow inside the fuel cell active area. Then, the ferromagnetic circuit analyzer is positioned around these models to detect the global and local faults positions based on the fabricated external magnetic field difference at the analyzer level. The global fault explains the faulty cell in PEMFC stack whereas the local fault identifies the fault position inside the affected cell. Finally, we validate the results obtained by the FEM by comparing the simulated magnetic field to the measurements obtained by the experimental testbench.

Following the 2D emulator results obtained in chapter 2, chapter 3 is dedicated to verifying the multi fault position detection of the data-driven diagnosis strategy. In this strategy, pattern classification based diagnosis approach is proposed. This approach concerns 3 faults based on there size and position inside the fuel cell active area. Magnetic field difference measured by the magnetic sensors are selected as the original variables for diagnosis. Feature extraction techniques, namely PCA, KPCA and LDA, and classification techniques, namely SVM, kNN and DT are used successively to extract diagnosis oriented features and classify the features into different classes related to the fault position. The performance of several feature extraction and classification are compared based on diagnosis accuracy. As the classification techniques used belongs to a supervised learning method, the data driven used was labeled based on the current supplied by the current sources to the different regions of the 2D emulator.

In the last chapter, a new design of the ferromagnetic circuit analyzer was presented. First, within the same number of sensors, this design was compared with the design used in chapter 2 to study the influence of magnetic sensors distribution around the stack. Then, some geometric parameters variations effects of these analyzers were studied like air gap width, design dimension and number of sensors inside the circuit analyzer. Based on the obtained results, a new technique for external magnetic field measurements were proposed to apply it on the FEM and validate on the experimental testbench.

CHAPTER 1

PEMFC SYSTEM DESCRIPTION

A fuel cell is a device which converts the chemical energy (hydrogen and oxygen) into electrical energy plus byproducts like heat and water. The Fuel Cell (FC) is known since 1839 [2] but it wasn't commercially used until the space race began in the late 1950s. Since the late 90's, the scientific research on the FC has increased [3] and recently, many companies starts to commercialize this technology due to their high efficiency and in-situ near zero-emission operation. Different FC types can be classified based on their electrolyte types, operation temperature and their working area [4]. Basic information about these fuel cells is summarized in Tab(1.1).

Table 1.1: Different Fuel Cell types

Fuel Cell Types	Mobile Ions	Operating Temperature	Application and Notes
Alkaine (AFC)	OH^-	$50 - 200°C$	Used in space vehicle, e.g Apollo shuttle.
Proton Exchange Membrane (PEMFC)	H^+	$50 - 100°C$	Vehicles, mobile applications, and For lower power CHP systems.
Phosphoric Acid (PAFC)	H^+	$220°C$	Suitable for portable electronic systems of low power, large numbers of 200 kW CHP in use.
Molten Carbonate (MCFC)	${CO_3}^{2-}$	$650°C$	Suitable for medium to large scale CHP systems, up to MW capability.
Solide Oxide (SOFC)	O^{2-}	$500 - 1000°C$	Suitable for all sizes of CHP systems, 2 kW to multi MW

1.1 PEMFC Stack Structure

A stack is defined as a group of cells connected in series which are bounded by an end plates at both sides see (Fig(1.1a)). As shown in Fig(1.1b), the middle of both Bipolar Plates (BP) of a single cell of PEM consists of following components [5].

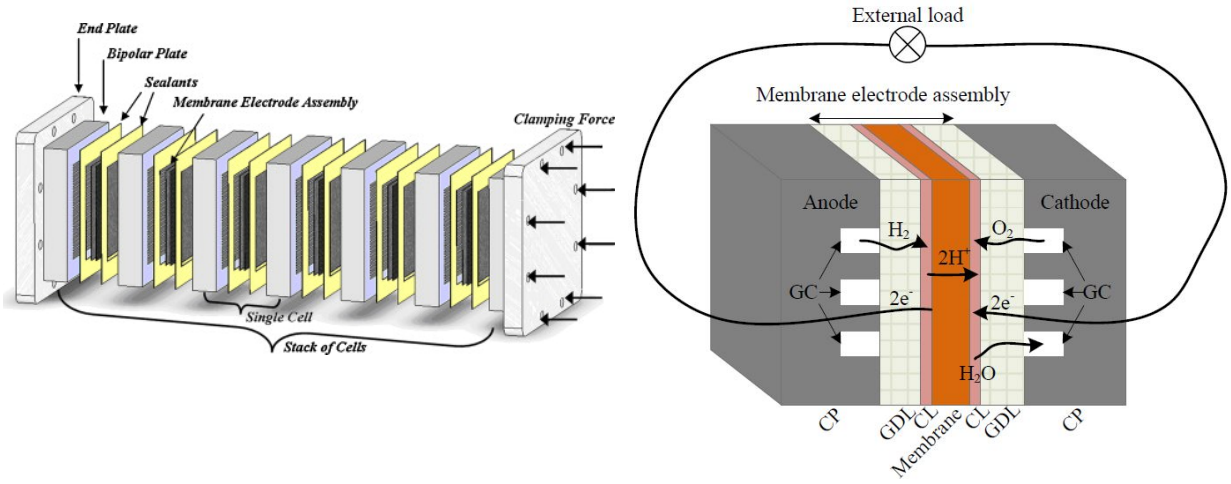

(a) (b)

Figure 1.1: (a) PEMFC stack structure [6] , (b) Single PEM cell components [1]

- *Membrane*

Polymer membrane is the heart of PEMFC that conducts protons due to the chemical reaction which can occur at the anode and cathode side of the electrolyte.

- *Catalyst Layer (CL)*

The catalyst layers exist on both membrane sides. In the early days PEMFC platinum catalyst layers development was used. These layers are formed from a very small platinum particles which are distributed over a larger particles of carbon powders surface.

- *Gas Diffusion Layer (GDL)*

GDL is carbon paper or cloth which diffuses the gas onto catalyst. Once the catalyst is fixed on the two sides of membrane, the both components are then sandwished between the two carbon cloth. It also forms a protective layer over CL, which forms an electrical connection between membrane, CLs and BP. The combination of membrane, CLs and GDLs is usually named as Membrane Electrode Assembly (MEA).

- *Collector Plates (CP)*

These plates are settled on both external sides of PEMFC. On each side the plate is grooved which provides the structural support of FC and facilitate the gas flow on one or both cell sides. It can also acts as an electric and heat conductors.

1.2 PEMFC System Ancillaries

Without using ancillaries supports for PEMFC system, the stack by itself would not be useful even if fuel cell stack is the heart of the PEMFC system. Managing these ancillaries prevents membrane fracture, stack degradation and extends fuel cell life time. In Fig(1.2) all the ancillaries needed to build PEMFC system is involved as following:

- Air supply subsystem
- Hydrogen supply subsystem
- Water management subsystem
- Thermal subsystem
- Power management subsystem

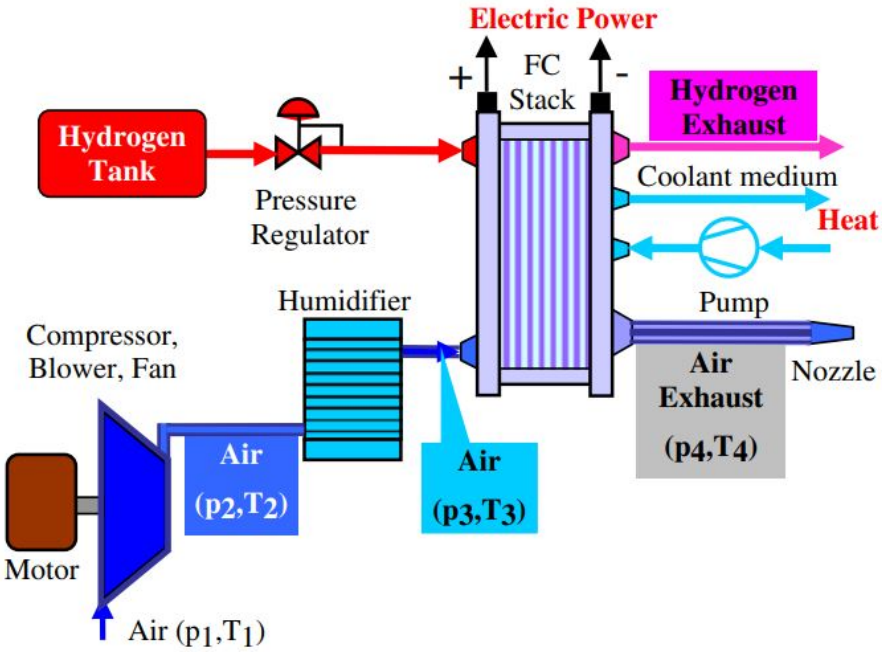

Figure 1.2: PEMFC structure

1.2.1 *Air supply subsystem*

This system is one of the most important elements that certify an enough amount of oxygen in the cathode by regulating the compressor located at the air inlet with a proper air pressure which generally pressurized slightly above the atmospheric pressure 2.5 bar[7]. Controlling cathode stoichiometry S_c and the air pressure are mostly coupled in which the appropriate S_c makes the stack operates in an optimal state whereas deficient air flow amount can cause stack degradation and increasing power losses of the system.

1.2.2 *Hydrogen supply subsystem*

Hydrogen is usually compressed and stored in a tank which supply the stack. Controlling the flow rate and hydrogen pressure is turned out through the valve, pressure regulator and flow regulator. Hydrogen can be applied in three general operation modes: flow through mode, re-circulation mode and dead-end anode mode. In the flow through mode there is an excess of hydrogen flow inside the stack and the unreacted hydrogen is liberated directly from the outlet leading to a low hydrogen pressure utilization phenomena. In recirculated anode mode uses a re-circulation devices including electrochemical pump, ejector and compressor to recycle the unreacted hydrogen at the anode outlet in order to improve the hydrogen utilization efficiency [8]. In dead-end mode the hydrogen outlet is closed and

the hydrogen is consumed by the stack. When using dead-end mode, water and other impurities are gathered at different MEA layers leading to a voltage drop [9]–[13] of the stack. Therefore, cleaning the anode channel is necessary to limit stack degradation.

1.2.3 *Water management subsystem*

Water helps proton transportation through the membrane and the catalyst layer of MEA. Water production occurs at the cathode catalyst layer due to the hydrogen and oxygen electrochemical reaction. Water management in the stack improve the membrane conductivity and prevent the membrane to be dried. On another hand, too much water leads to a flooding phenomena which can be due to low air flow and low temperature [14], or reduction of GDL porosity by water [15]. Water management main role is to keep the stack membrane hydrated. There are two main approach for this management: external and internal humidification systems. In external humidifier, the reactant gases humidity is controlled by using the contact time of the reactant gas with the water and the humidification temperature [16]–[18]. In the internal humidifier, the moisture of the membrane is maintained by injected directly a hydration level within the proper range [19].

1.2.4 *Thermal subsystem*

More than half of the produced energy by the electrochemical reaction is a heat energy and not an electrical energy. Since a chemical reaction is highly dependent on temperature, then regulating PEMFC temperature within a proper range will provide the optimal electrochemical reaction inside the stack and prevent material degradation. Moreover, temperature variation can affects the condensation of water and gases inside the stack. For example, at a high temperature membrane will dry due to the water vaporisation making ohmic resistivity high which leads to a voltage drop at the membrane level. Similar to the water managements, the thermal subsystem main role is to keep membrane moisture by adapting the temperature in the optimal operating range [20], [21]

1.2.5 *Power management subsystem*

Power conditioning subsystems are used to control the non stable electric power flow inside the stack and the power of the load. Some factors like cost, efficiency and electric isolation to protect the overload in the system are used to determine the power management subsystem which will be used [22]. A certain power electronics subsystems can be used in PEMFC system. For example, buck converter decreases the stack voltage, boost converter increases it or using the both power electronics subsystems (buck-boost) converters [23], [24]. In vehicle applications, the more commonly known converters are DC/DC converters, which are used in auxiliary subsystems and main power chain in order to control the stack voltage at a static value. In addition to the DC/DC converter, the power inverter and electric motor are normally the main components of the power chain.

1.3 PEMFC Degradation

Among the components of the PEMFC cell, the MEA component is the most affected compared to the others due to the different mechanical, thermal and chemical stresses of the PEMFC system. Apart from the stresses and the effect of aging, some degradations may be due to malfunctioning or manufacturing process of the PEMFC cell.

1.3.1 *Reversible Degradation*

Reversible failures can lead to temporary system shutdown due to sub-optimal operating conditions that can affect the performance of the PEMFC cell. Water management is the main critical issue in these failures such as cell flooding due to water accumulation at the cathode and membrane drying resulting from insufficient wetting at the membrane.

1.3.1.1 Flooding of the stack

Cell flooding is a buildup of liquid in the diffusion layer, which blocks the flow of gas produced by the electrochemical reaction at the electrolyte to move throughout the channel area of the cell. Since water production is primarily generated on the cathode side, flooding usually occurs on the cathode side of the cell. [25].

1.3.1.2 Membrane drying

Membrane drying defects result in blocking proton access to the catalyst surface and increasing membrane resistance. In addition, heat management defects lead to high temperature due to inefficient cooling causing liquid evaporation which dehydrates the membrane. Most of the time, membrane drying takes place on the anode side when liquid is produced at the cathode. [25].

1.3.2 *Irreversible Degradation*

Irreversible damage directly affects the MEA. Carbon erosion in the catalyst layer and platinum allocation cause the membrane to lose its mechanical properties due to aging.

1.3.2.1 Platinum catalyst degradation

With time, the platinum can dissolve inside the membrane, so the active surface tends to decrease [26]. In [27], "Crossover" phenomena identify whether the platinum generated in the membrane is ionic or metallic. The metallic platinum may be due to the loss of carbon during surface erosion.

1.3.2.2 Membrane degradation

The change of the cell's operating mode can cause a pressure variation peak to appear instantaneously during a stop/start operation. This variation creates a mechanical stress leading to a degradation of the membrane. In addition, the appearance of cracks in the membrane and fluctuations in the water content can be due to the cyclic variation of the inlet gases.

1.3.2.3 GDLs degradation

The degradation of the GDLs plays a fatal role in the decrease of the PEMFC performance. It leads to a heterogeneous distribution of the current density on the surface, some areas being more stressed than others. Three main degradations can be observed in GDLs: loss of hydrophobicity, carbon erosion and variation of electrical and thermal resistance. Of these three mechanisms, loss of hydrophobicity is the main cause of the decrease of PEMFC performance. High current density has the most impact on the degradation of GDL during battery operation [28]. Finally, it is very difficult to distinguish between GDL and membrane degradation. [29].

1.4 Magnetic field and current density inside PEMFC

The distribution of current density within the fuel cell can provide important information about the health of the cell. Bio-Savart's law clearly shows the proportional relationship between the current and the magnetic field produced, so the evaluation of the magnetic field produced can also give important information about the health of the cell. The analysis of the current distribution can be done by a direct method, such as the immediate measurement of the current flow using current sensors inside the cell, which is an invasive technique, or the indirect method that measures the magnetic field produced from the internal current density, , which is a non-invasive technique.

1.4.1 *Current distribution measurement techniques*

As a rule, the measurement technique (MAPPING) of the current density flow inside the fuel cell is mainly invasive technique. In this method, the fuel cell component like bipolar plates and MEA involves several modifications. The main configurations for method utilize a segmented and non-segmented fuel cell. In a segmented cell approach, current collectors are mainly segmented to create a collecting terminals for the local current measurements [30] of a single cell or the final cell located at the end of the stack, see Fig(1.3).

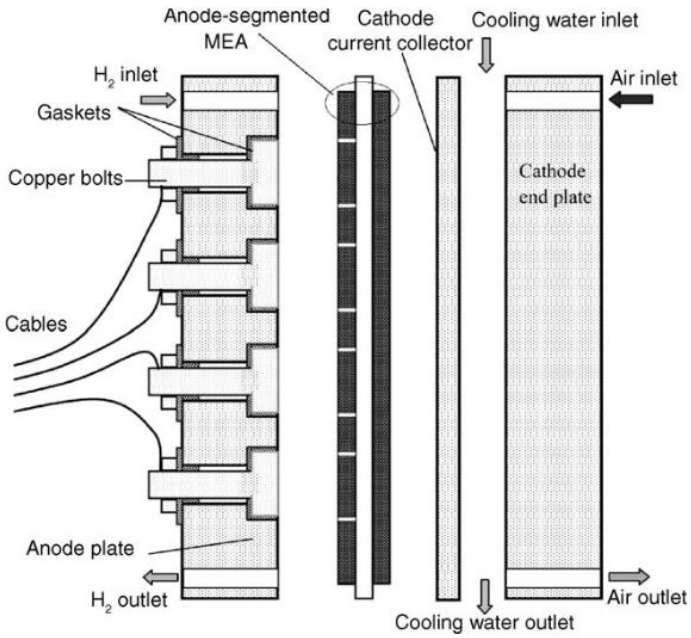

Figure 1.3: Segmented Cell [30]

Segmentation can be avoided in systems by using the sensor plate printed circuit board (PCB). This technology is widely used with non-segmented [31] and segmented [32] bipolar plates, see Fig(1.4). In addition, [32] studies three different local current distributions (co-flow, counter-flow, cross-flow) of several physical parameters such as stoichiometric air/hydrogen ratio, cell pressure, cell temperature and relative humidity. It was found that the counter-flow of the local current distribution gives an optimal performance of the cell compared to the other flows that lead to a larger variation of the local current under the effect of the variations of the physical parameters. For example, Fig(1.5) shows the three flows under the effect of pressure variation.

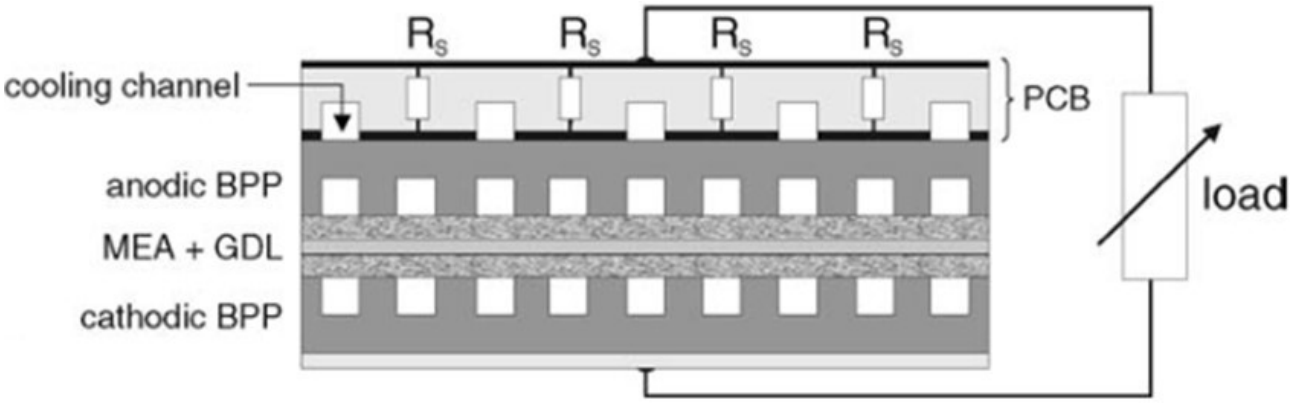

(a)

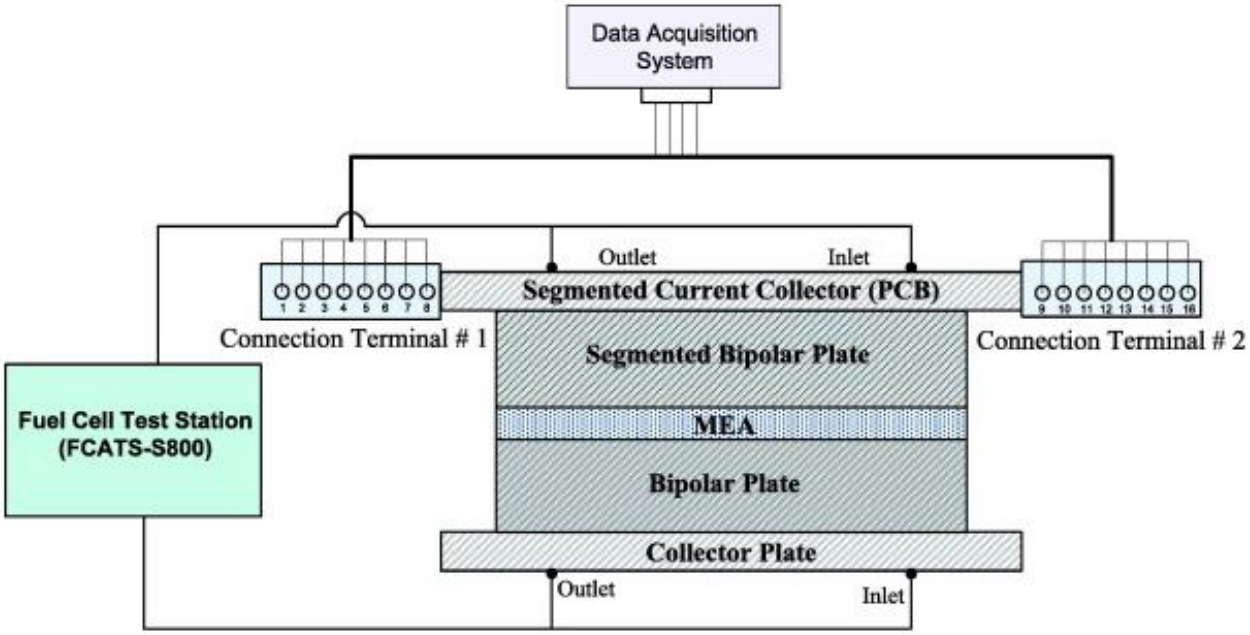

(b)

Figure 1.4: (a) Non-Segmented Bipolar Plate (BP) [31], (b) segmented Bipolar Plate [32]

Moreover, current density distribution (CDD) can be determined using the PCB technology under several cell performances, like rapid cold start [33], effect of micro porous layer [34], and low temperature shunt resistors [35].

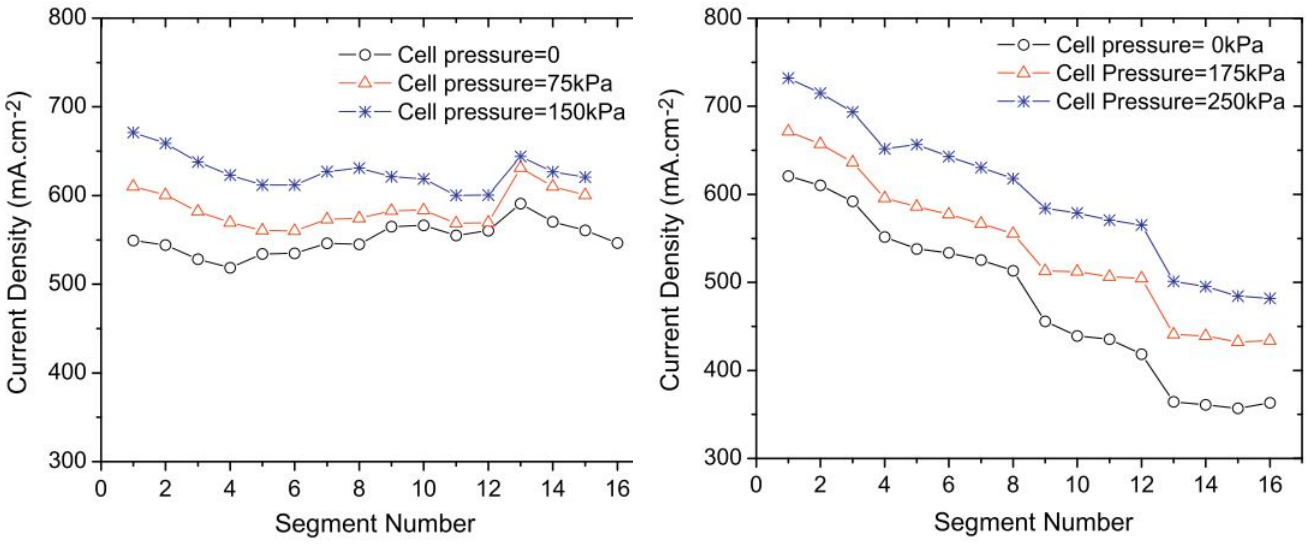

(a) (b)

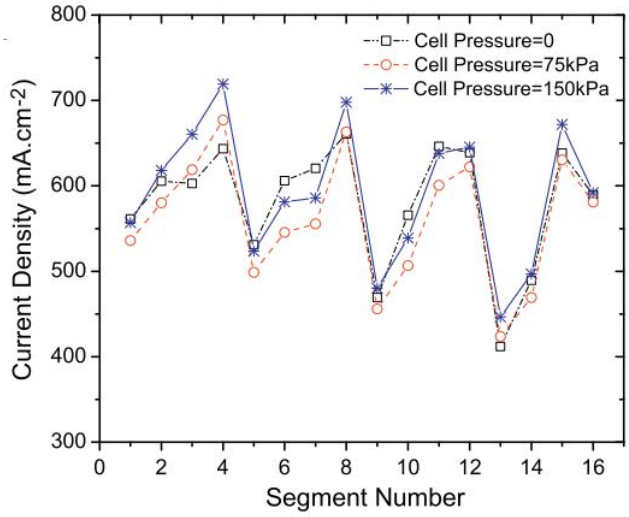

(c)

Figure 1.5: Pressure variation on a single fuel cell for (a) Counter-flow (b) Co-flow (c) Cross-flow [32]

1.4.2 *Magnetic field measurement techniques*

The mapping of the current distribution inside a fuel cell can be inversely calculated by measurements of the magnetic field inside or outside the cell. In general, the magnetic measurement technique is mainly non-invasive. This indirect method can be classified into two categories: internal and external magnetic measurements.

1.4.2.1 Inside magnetic measurements

This study focuses on the analysis of current density flow using a magnetic probe. The magnetic field device is located inside the cooling holes of the fuel cell so that the electrical behavior of the cell is not affected. Due to the lack of contact between the grid circuit and the fuel cell, the internal magnetic measurement technique Fig(1.6) has the advantage over the segmented and non-segmented cell.

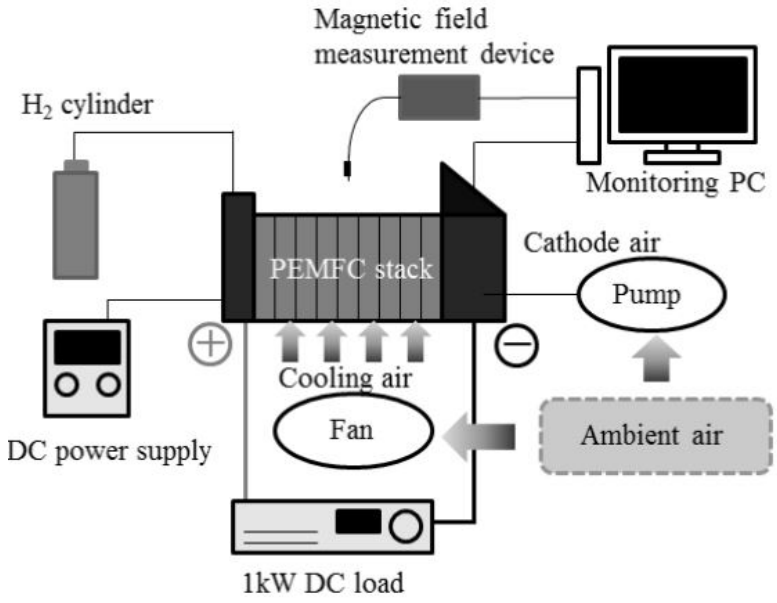

Figure 1.6: Magnetic sensor probe inside cooling holes of the fuel cell [36]

1.4.2.2 Outside magnetic measurements

This technique (magnetotomography) uses the external magnetic field produced by the internal current flow density inside the fuel cell. A series of studies have been carried out on this technique because of its high accuracy and lesser side effects on the fuel cell operation compared to other techniques. The first magnetotomography technique was presented in [37] when a three-axis magnetic sensor is installed in a moving robotic arm. Moreover, Fig(1.7) shows another method to verify the current distribution from the external magnetic field using a hall sensor and Magneto-Impedance (MI) at 121 points around the stack. These tools solves the problem of current mapping but still suffers from the computational time required for acquisition. Increasingly, interest in improving this technique has grown and in [38], an optimized problem is solved by minimizing the difference between the magnetic field produced by the stack and that produced by the ground and random combinations of current density.

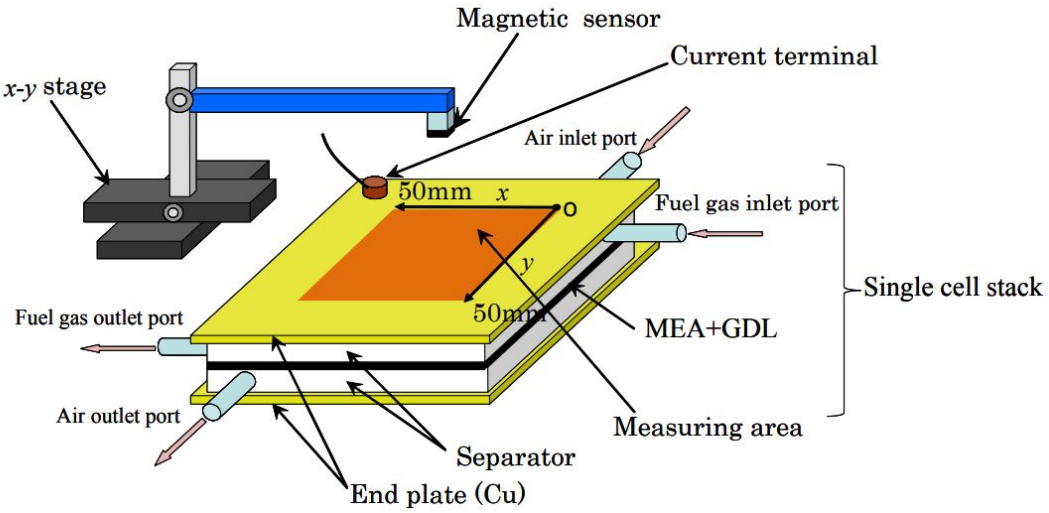

Figure 1.7: Schematic view of measuring magnetic field [39]

Current density mapping using magnetotomography technique can be classified into two categories: 2D and 3D current mapping. In the 2D mapping expresses the local fault while the 3D expresses the global fault. The 2D mapping expresses the local fault adopted based on the consistent current across its main direction. On another hand, the 3D current mapping expresses the global current fault created based on a heterogeneous current flow across its main axis. For this heterogeneity, [40] demonstrates two current flow methods applied on a 4 parts segmented stack Fig(1.8).

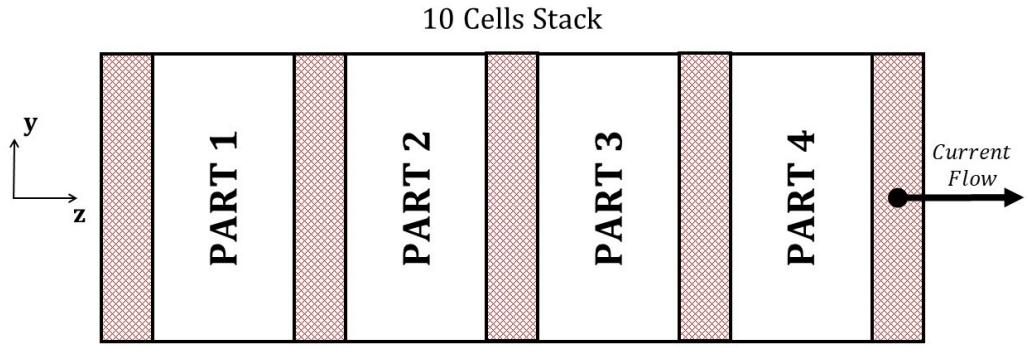

Figure 1.8: . Stack divided into four parts

The 2D duplicated method was explained by imposing a current density in each part of the stack. However, the 3D method was described by imposing a vector potential for the electrical conductivity of each part of the cell (Bipolar Plates (BP), membrane electrolyte assembly (MEA)). Moreover, in this study, the current is mapped based on the measured radial (B_u) and axial (B_w) external magnetic field components. To improve the observation of the heterogeneous current distribution, the magnetic sensors array was placed at three different positions of each part of the stack, see Fig(1.9).

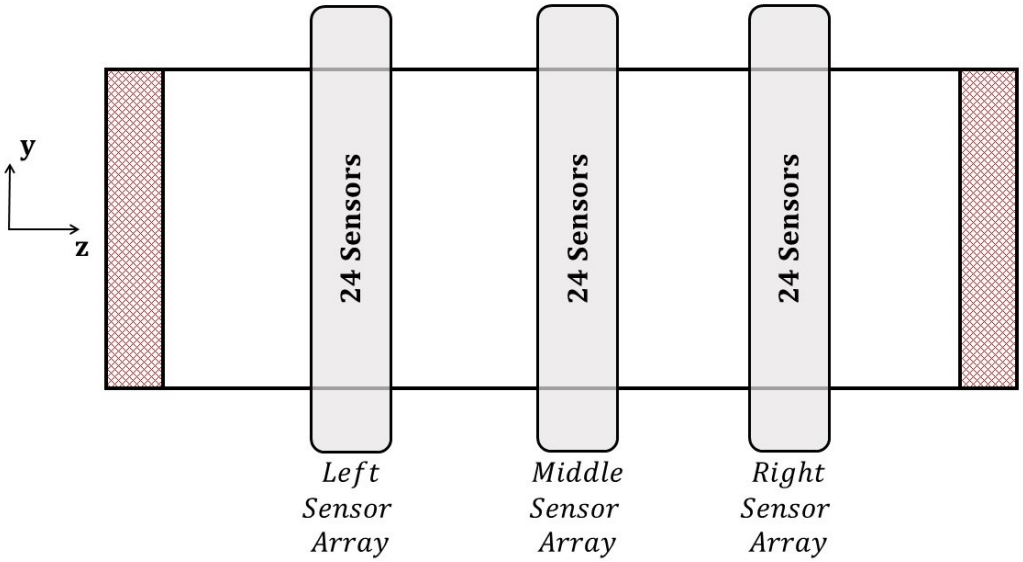

Figure 1.9: Array location around the stack single part.

In Fig(1.10), The blue chart depicts the produced magnetic field components by the whole current distribution and the red chart explains the magnetic field fabricated by each part using the 2D duplicated method.

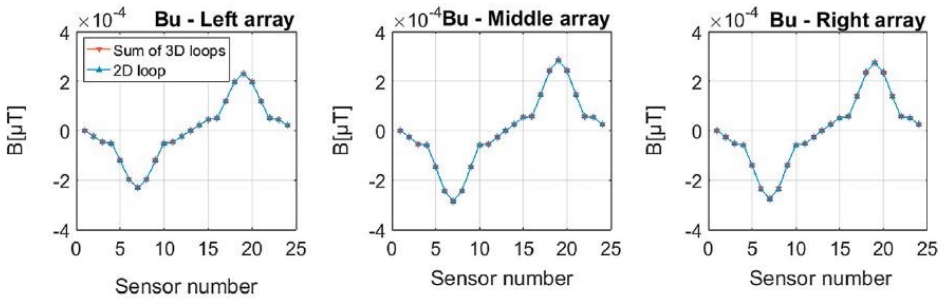

(a)

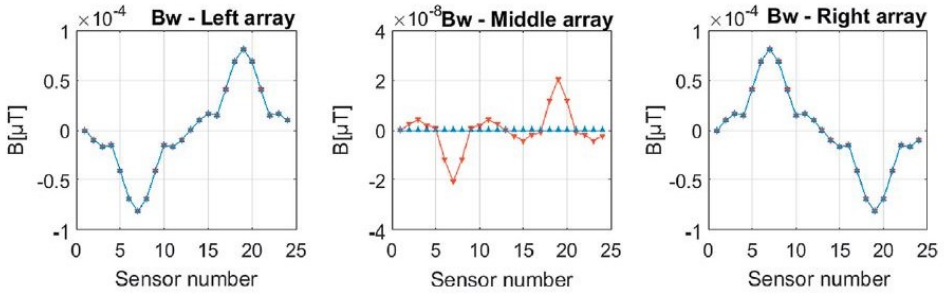

(b)

Figure 1.10: (a) Radial and axial magnetic field for 2D current vectors and (b) its equivalence of a sum of 3D current vectors using the 2D duplicated method.[40]

Similarly, Fig(1.11) demonstrates the locale and global generated external magnetic field using the 3D method.

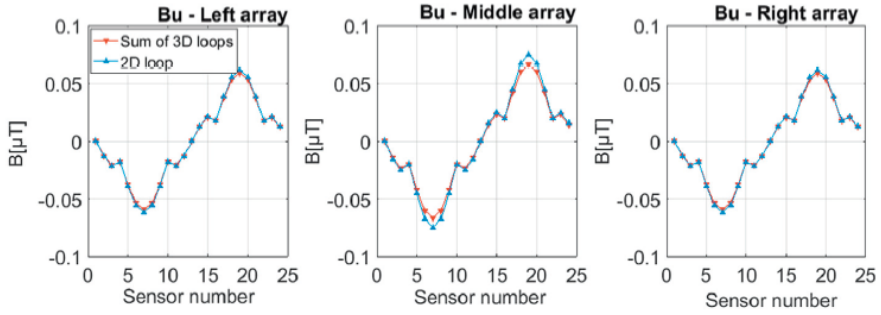

(a)

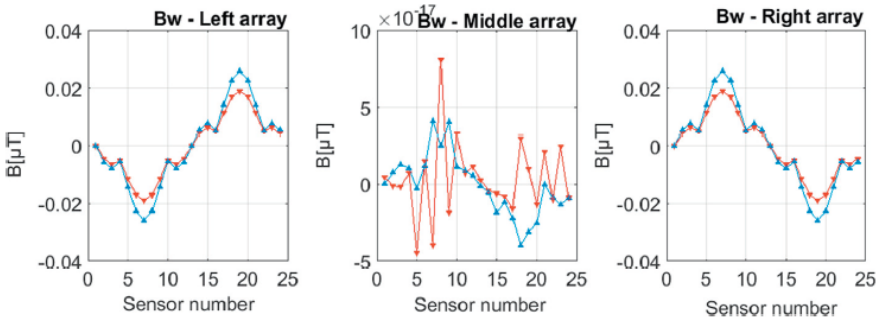

(b)

Figure 1.11: (a) Radial and axial magnetic field for 2D current vectors and (b) its equivalence of a sum of 3D current vectors using the 3D method.[40]

Therefore, from the results obtained, the external magnetic field generated by the 2D fault is equivalent to the sum of the produced magnetic field fabricated by the 3D fault.

Furthermore, current distribution identification in fuel cell from external magnetic field measurements is improved a lot by simplifying the measurement system and reducing the time computation. In Fig(1.12), the presented approach requires a small number of sensors (30 sensors) are fixed around the stack to enable instantaneous measurements in 1 min. This timing in this approach have the advantage over the one presented in [37] since the internal state of health does not vary during 1 min compared to 15 min. However this approach solve complexity and time computation problem but still suffer from localizing the fault position inside the stack. This is due to the fixed magnetic measurements at a single sensors positions which gives a global signal about the fault image.

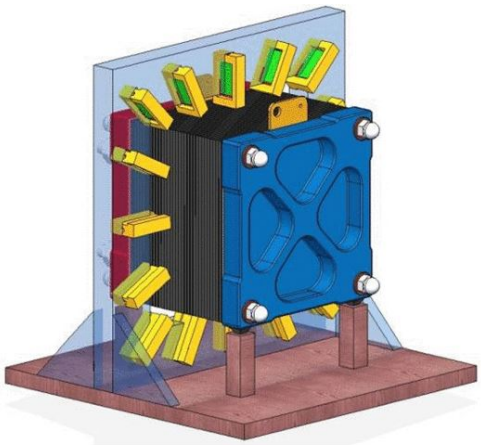

Figure 1.12: Magnetic measurements: stack (blue, red, and black) and sensors (yellow and green)[41]

A step forward have been taken in [42] by adapting the previous approach into more localized fault by proposing a 3D identification method. Fig(1.13) explains the 3D method used by locating the 24 sensors array at 3 different positions around the stack. This approach over determined a 144 equations for a magnetic measurements (number of sensors$\times$three positions$\times$ B_r, B_a), where B_r is the radial and B_a is the axial magnetic at each sensor level.

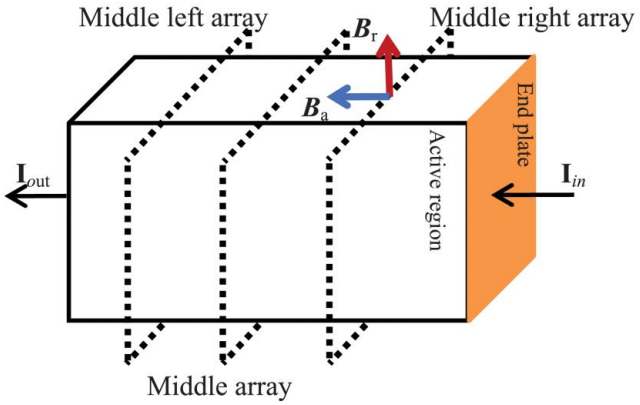

Figure 1.13: Sensors arrays locations around a fuel cell stack[42]

1.4.3 *Analysing current density and magnetic field distribution*

In the previous sections 1.4.1 and 1.4.2, current mapping can be analysed directly through an invasive and indirectly through non-invasive (Magnetotomography) techniques.

1.4.3.1 Direct Model

In this model the current is provided inside to produce the magnetic field outside the fuel cell. The direct model is divided in two steps: first to compute the current flow by solving the electric conduction problem. The second step is to compute the produced magnetic field around the fuel cell by solving the magnetostatic problem.

1.4.3.1.1 Finite Volume Method (FVM)

First, current density conduction was demonstrated in the steady-state behaviour of the PEMFC stack to investigate on one hand the material conductivity, electrical configuration and on another hand the effect of contact resistance (anomalies) [43]. In this approach the model covers all the physical phenomena that takes place in the MEA region (cathode, anode and membrane). Modeling the electrical behaviour of the stack is performed by solving numerically the transport equation in a steady-state current conduction with the electromotive force Eq.(1.1), in addition to considerations on the nonlinear behavior of the material in order to expose the actual non linearity of the electrochemical behavior of the PEMFC Eq.(1.2) by using the Finite Volume Method (FVM) [44]. The 3D microscopic distribution of the current density in the stack was determined after applying the New-Raphson algorithm to couple Eq.(1.1) and Eq.(1.2)

$$\mathbf{div}\sigma\mathbf{grad}V - div\sigma E_m = 0 \tag{1.1}$$

$$\Delta V(j) = U_{mo} - R_{so}j - A\ln(\frac{j}{j_{eq}} + 1) \tag{1.2}$$

where E_m is the electromotive force, U_{mo} is the Open Circuit Voltage (OCV) of one cell, R_{so} the total resistance of MEA and A and j_{eq} are fitted parameters that represent the over potential of the electrochemical reaction.
Second, after analysing the current distribution in the MEA region the generated magnetic field around the stack is then calculated using Biot Savart Law Eq.(1.3) for a static current distribution and when there is no ferromagnetic material parts in the near environment.

$$B(r) = \frac{\mu_0}{4\pi}\iiint_{\Omega}\frac{j(r_s)\times(r-r_s)}{|r-r_s|^3}d\Omega_s \tag{1.3}$$

where **B** is the magnetic induction at point **r**, **j** is the current density at integration point r_s, μ_0 is the permeability of the free space and Ω is the volume of the stack where current flows. To supply the cell by a current, an electric circuit model should be coupled with the fuel cell.

1.4.3.1.2 Finite Element Method (FEM)

In this section, the electrokinetic problem is solved by the finite element method. This method is mainly explained by 3 steps, geometry, mesh and physics. The geometry explains the elements of the regions where the current density flows. The mesh discriminates these regions into a set of

nodes so that j is conserved between two adjacent elements. In physics, the fundamental properties of the materials needed to create the electrical circuit are defined. The formulations in [45] explain the discrimination of the elements and how this approach is easily coupled with the external electric circuit to obtain an accurate calculation of the external magnetic field. For this reason, the FEM is preferred to the FVM presented in [41]. As in the FVM, once the electrokinetic problem is solved, the current density distribution inside the stack is well known to perform the magnetic calculation using equation (1.3).

1.4.3.2 Inverse Model

In this model, estimating the current density inside the stack is done through measuring the external magnetic field. Assessing the current inside cannot be directly calculated, it requires an inverse of Biot Savart law Eq.(1.3) which considered an ill post problem since it is very sensitive for noise.

1.4.3.2.1 Finite Volume Method (FVM)

Solving this problem by classical optimization problem is forbidden due to the high complexity problem. So, in [41] a regularization technique was used to filter out the noise produced by the ill post problem. This technique properly choose ϕ_P (current basis) and ψ_K (sensor projection) functions. For a proper ϕ_P, a 2D duplicated method completed with 3D model Fig(1.14) were used to define the current basis in a faulty condition in a limited length for the fuel cell (bipolar, membrane and end plate).

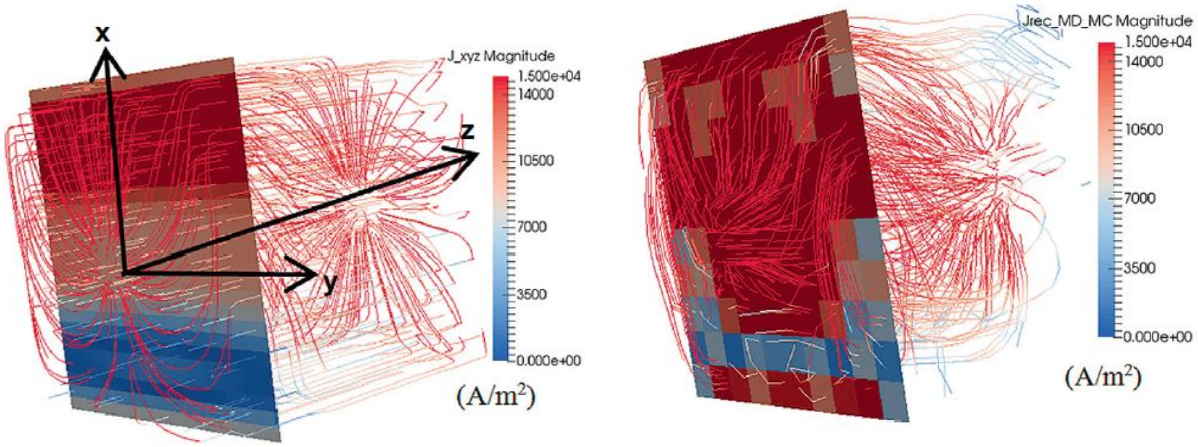

(a) (b)

Figure 1.14: Reconstructed current density. (a) With the 2D duplicated approach, (b) with the purely 3D approach

Moreover, for a proper ψ_K is performed by optimizing the magnetic sensor location around the stack so that signal to noise ratio is minimum (SNR). The first solution of this regularized technique is not unique, so S^+ Eq.(1.4) should be truncated to keep only the singular values of S^+ matrix Fig(1.15).

$$J = S^+ B \tag{1.4}$$

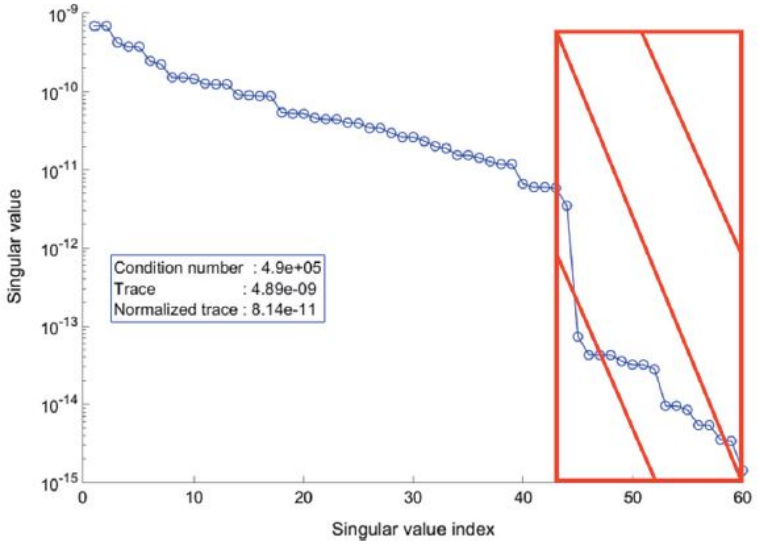

Figure 1.15: Matrix spectrum obtained for the 2D duplicated method, the hatched part illustrates the truncation level.[40]

1.4.3.2.2 Finite Element Method (FEM)

In the forward model, the electrokinetic model is solved by FEM to simulate the conductivity faults in a fuel cell stack and obtain virtual measurements. In the second step, the external magnetic field is used to reconstruct the internal current density distribution by obtaining the inverse discriminated Biot Savart matrix S^+ using singular value decomposition (SVD). In [45] a new model is studied to create the approach in which the current flow deviation was studied considering the z-axis as an original direction of current flow and the x-y axes are the directions where the current can deviate. For this reason, the current base and the magnetic field base are calculated. The current base was calculated using the curl operator of the vector potential [45]. On the other hand, the magnetic field basis was computed on 3 different positions around the stack instead of placing the sensor array in the middle of the stack [41]. This approach guarantees the S^+ matrix in a 3D domain.

1.4.4 *Influence of degradations on current density distribution inside PEMFC*

The in-homogeneous distribution of current inside a fuel cell is due to induced anomalies that can affect the operating conditions of the cell. These anomalies can be classified into two categories: local anomalies (flooding, resistivity) and global anomalies (drying, air stoichiometry).

1.4.4.1 Flooding anomaly

In this anomaly, the fault is localized at the cathode part leading to a local distribution due to the diffusion of the water production from the cathode to the anode part. The variation of the fuel cell temperature is proportional to the percentage of flooding. The approach [46] is based on the analysis of the effect of flooding phenomena on the local current distribution. The figure (1.16) shows the current density in a single cell as a function of the cell voltage under the effect of partial and complete flooding. To summarize the flooding in a single cell, the process starts at the output region and then deviates to the input region of the cell.

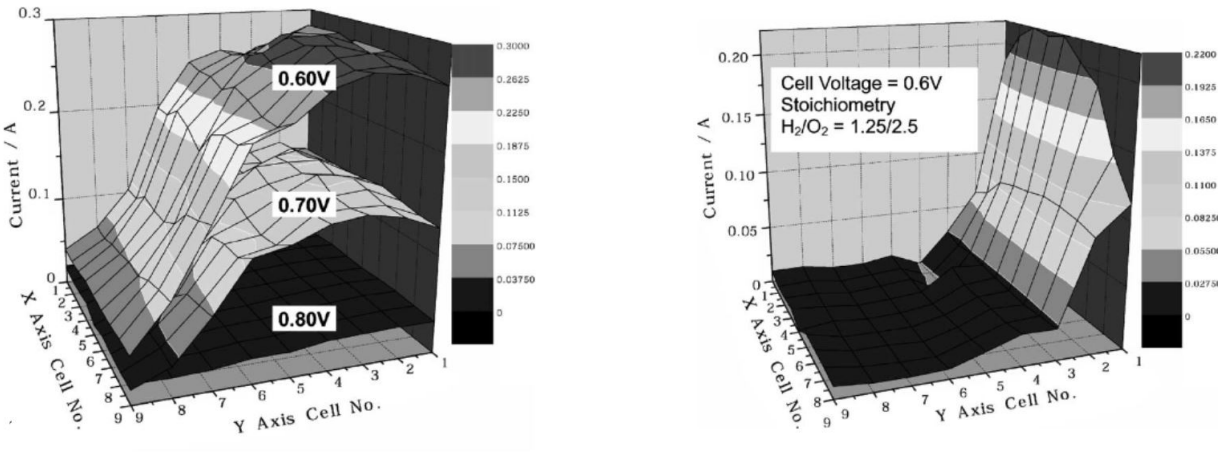

(a) (b)

Figure 1.16: Distribution of current with respect to a single cell voltage under (a) a partial flooding (b) complete flooding [46]

1.4.4.2 Resistance anomaly

This anomaly directly affects the voltage inside the faulty cell and the current flow distribution due to the Ohmic law. A non-uniform resistance of one of the cells inside the stack has been demonstrated in[44]. This type of fault induces a voltage drop of the cell Fig(1.17a) in the faulty region and, due to the cell-to-cell electrical coupling, the cell's neighbors will also be affected. It is important to note that the neighboring cell has a higher cell voltage near the defective region. This higher cell-induced voltage accelerates the degradation process at the MEA. On the other hand, the conservation of the current distribution before and after the defective operation leads to an increase in the current distribution near the abnormal region Fig(1.17b).

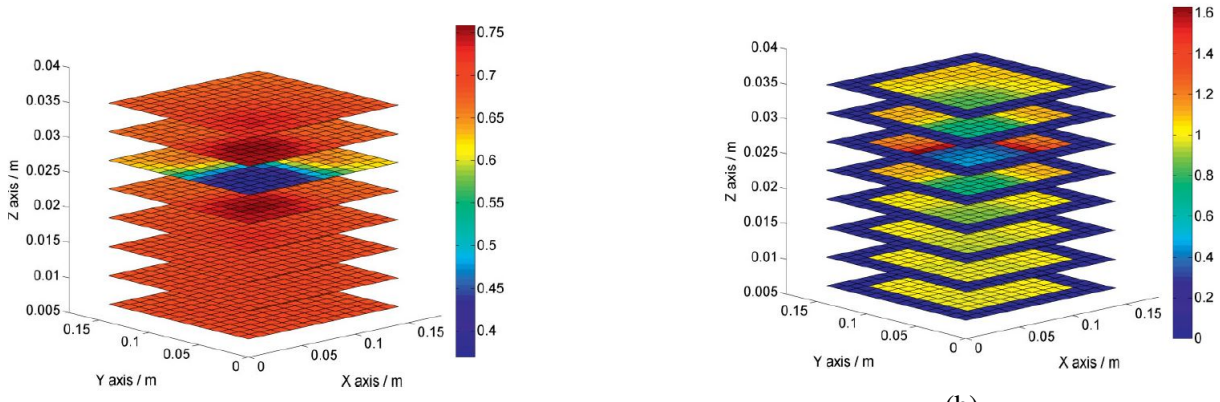

(a) (b)

Figure 1.17: Cell voltage in V (a) current density in Acm^{-2} (b) in case of resistive anomalous [44]

1.4.4.3 Drying anomaly

This type of anomaly affects the faulty membrane, the faulty area is not bounded in a specific area like the flooding and resistivity anomalies. The variation of the air stoichiometry creates two types of

anomalies. A decrease in its value results in oxygen deprivation while an increase produces membrane dehydration.

1.4.4.3.1 Oxygen starvation

This anomaly occurs when the air stoichiometry decreases on the cathode side. Fig (1.18) shows the variation of the current density distribution as a function of the level of air stoichiometry drop. This anomaly clearly shows an increase in the current density value near the air inlet, which means a lower current density at the gas outlet due to the drop in air stoichiometry along the gas channel.

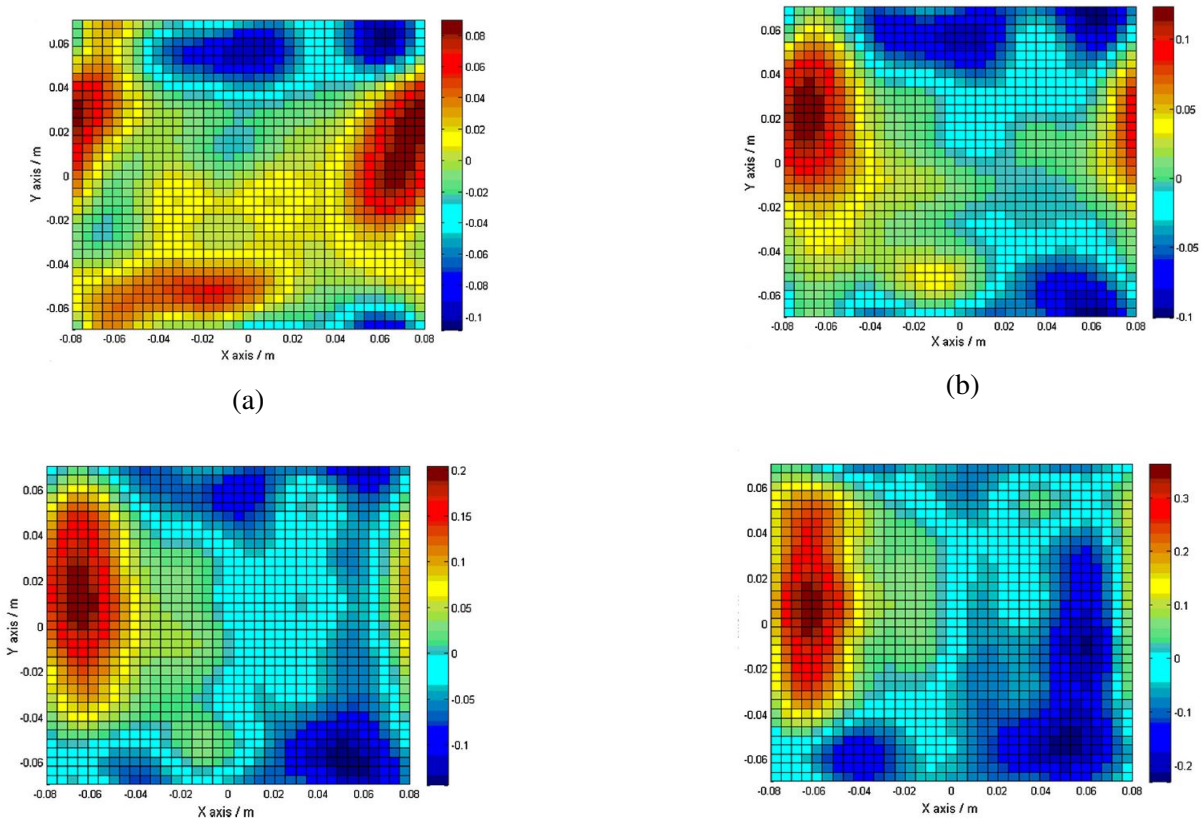

Figure 1.18: Reconstructed current density change from magnetic field measurement for air stoichiometry ranging from 2 down to 1.7 (a), 1.5 (b), 1.3(c) and 1.15 (d) [43]

1.4.4.3.2 Membrane dehydration

This anomaly is directly affected by the increase in air stoichiometry see(Fig(1.19)), resulting in a decrease in current near the air inlet and, conversely, an increase in current near the air outlet. The behavior of the fuel cell membrane is due to the effect of strong water removal at the cell inlet and hydration of the membrane along the gas channel on the cathode side.

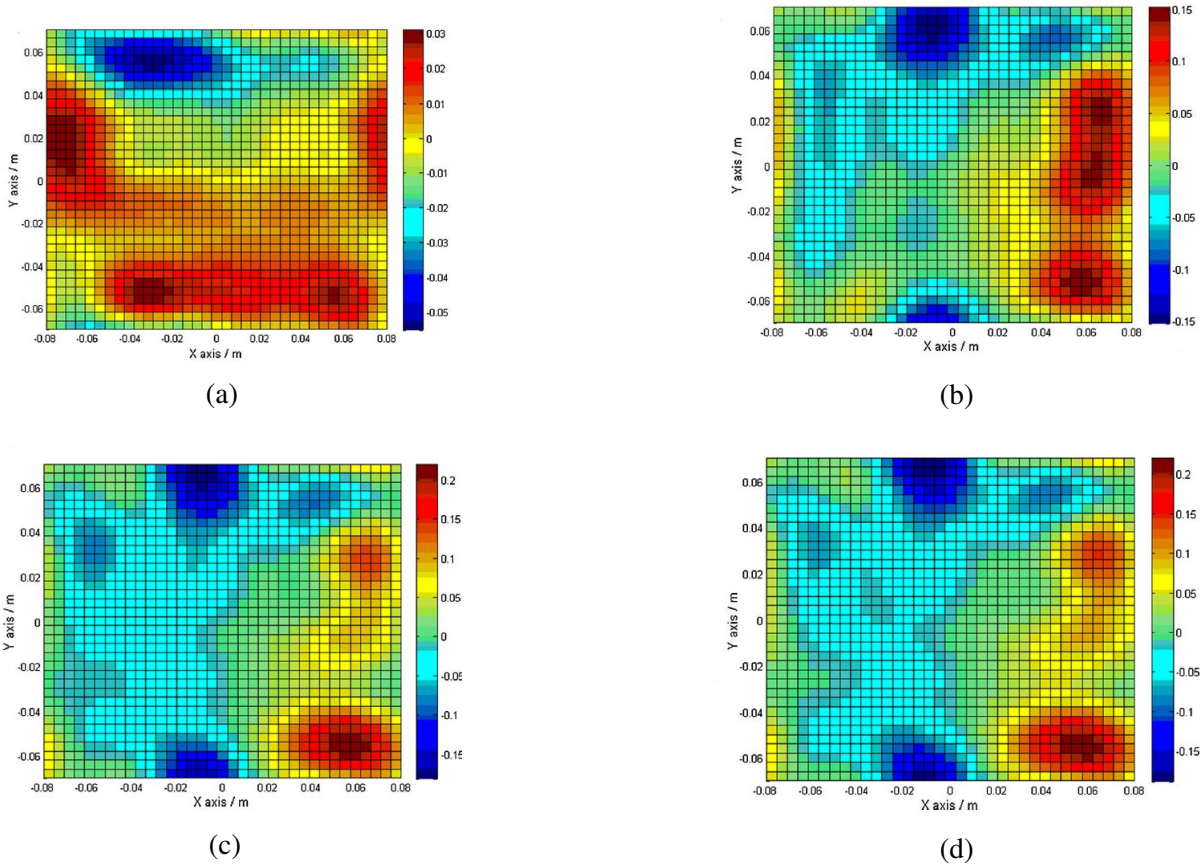

Figure 1.19: Reconstructed current density change from magnetic field measurement for air stoichiometry ranging from 2 to 2.2 (a), 3 (b), 4 (c) and 4.5 (d) [43]

1.4.5 *Measured variables used in diagnostic*

Different variables that impact the operating conditions of the fuel cell can be taken into account in a crucial way to establish a data-based diagnosis for a system. For PEMFC systems, cell voltage, air pressure, cell temperature are considered regular values that can be easily measured. On the other hand, more specific measurements have been used to obtain a useful variable for diagnosis.

1.4.5.1 Electric variables

Data-based diagnosis is based on regular measurements of the current density distribution, PEMFC voltage, or cell voltages. A more specific measurement is to study the cell polarization curve that relates the current density to the cell voltage to characterize the electrochemical performance of the cell [47]. As shown in Fig(1.20), the output voltage of the cell decreases as the current density increases, this is due to the different voltage losses (active, ohmic and concentration).

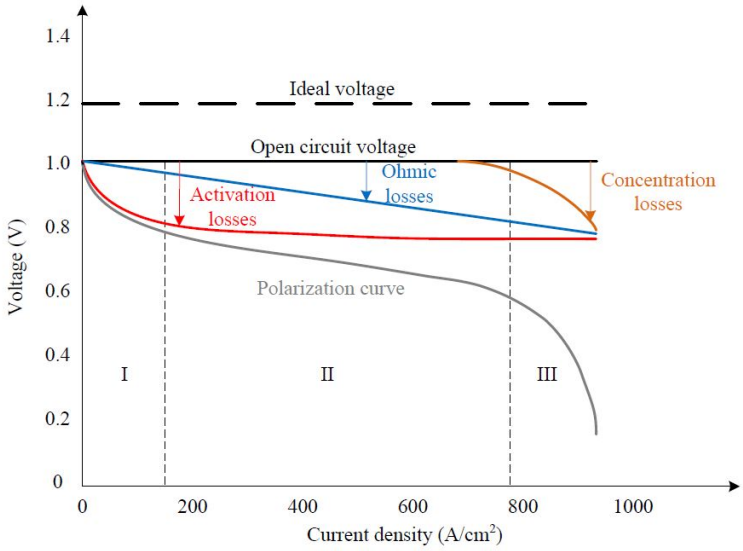

Figure 1.20: Various voltage losses and polarization curve of an operating PEMFC. [1]

In addition, line scan voltammetry (LSV) is a special measurement method that provides diagnosis based on cross-current and short-circuit resistance. Figure (1.21) shows an example of an LSV test result obtained on a 3-cell stack [48].

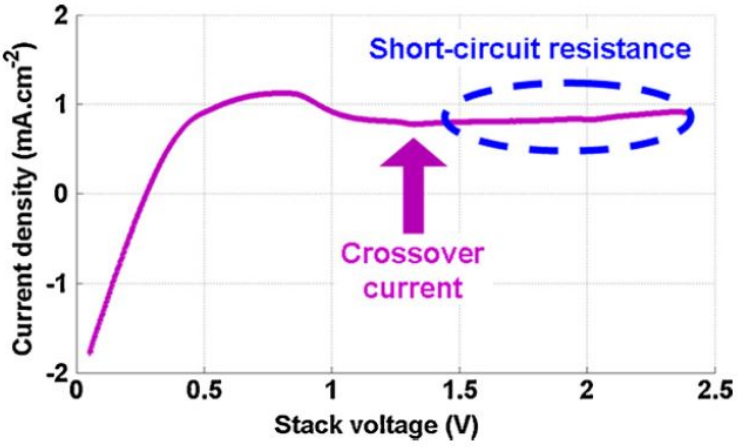

Figure 1.21: LSV test result obtained on a 3-cell stack. [48]

1.4.5.2 Fluidic variables

Fluidic variables are based on regular measurements of temperature, pressure, flow and humidity. These variables are generally used to diagnose degradations related to the operation of a system.

1.4.5.3 Magnetic field variables

Mapping the current density distribution from the external magnetic field measurements using the indirect model allows the external magnetic field to be a significant variable in the data-driven diagnosis, so that the position of the aging and degradation within the cell membrane [41] or stack [42] is identified.

1.4.6 *Conclusion*

This chapter introduced the working principle of PEMFC, the composition of PEMFC cell and PEMFC system. Then, the different types of failures on fuel cells and the art of diagnostic methods were presented. These methods focus on monitoring the affected cell within the stack by a current mapping analysis technique presented in an electrokinetic problem. Particular attention is paid to the diagnostic technique which has the advantage of providing the necessary information without disturbing the operation of the stack. This non-invasive diagnostic approach is discussed, and existing challenges are listed.

CHAPTER 2

MODELING OF PEMFC CURRENT DISTRIBUTION AND MAGNETIC FIELD

If the current distribution within the MEA can be considered homogeneous in normal FC operation, several faults like flooding, drying, reactant starvation or local membrane degradation generates a heterogeneous specific current density distribution. Consequently, assessing the current density inside the cell can provide important information about the health of the cell. Several invasive methods for current density measurement have been discussed in the literature, but they still suffer of the direct influence on the operation of the FC. Moreover, direct current distribution measurements are implying also high costs. Therefore, analyzing the magnetic field generated around the operating FC is important for the diagnostic process. As the source of this magnetic field is given by the current distribution, such magnetic field allow to observe faults influence on the external magnetic field around the FC. In this chapter, different 3D finite element models (FEM) have been presented to model the current density distribution that can be generated by 2D and 3D conduction faults.

2.1 2D conduction fault Model

This model considers a typical PEMFC stack with a current density distribution. This approach emulates the homogeneous/heterogeneous of the 2D current density flow within the active region of the fuel cell using a 3D magnetostatic application model.

2.1.1 *Geometry*

The simplified geometry of the 2D stack emulator model is presented in Fig(2.1a). The length of the emulator model is 200 mm divided in 16 equal parts (Z1 to Z16) emulates a homogeneous FC current in a conductive zone having a transversal section about 100 cm^2 (10×10 cm^2) see Fig (2.1b).

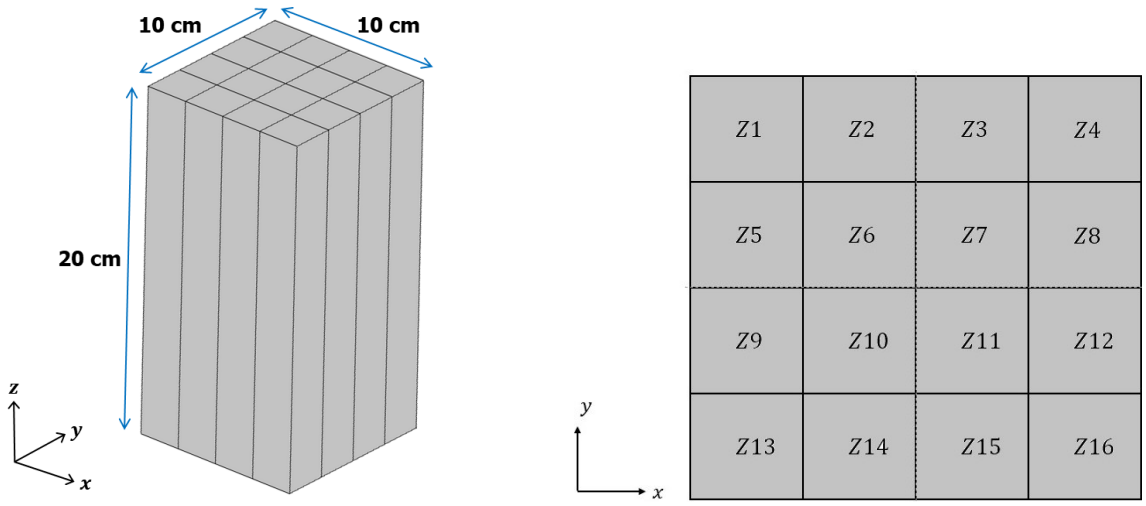

(a) (b)

Figure 2.1: Emulator dimensions (a) Emulator bars labeling (b)

2.1.2 *Current distribution inside the model*

Inside each bar the current density is considered homogeneous, so the total current I_{FC} flowing through the bars from the anode to cathode side is considered constant. In the normal model operating condition, the current density distribution between the bars are considered homogeneous. On another hand, Fig (2.2) shows the inhomogeneity current density distribution that can be explained by different operating problems like hot spot, degradation of the membrane, non-homogeneity of the hydration of the electrolyte membrane, etc.

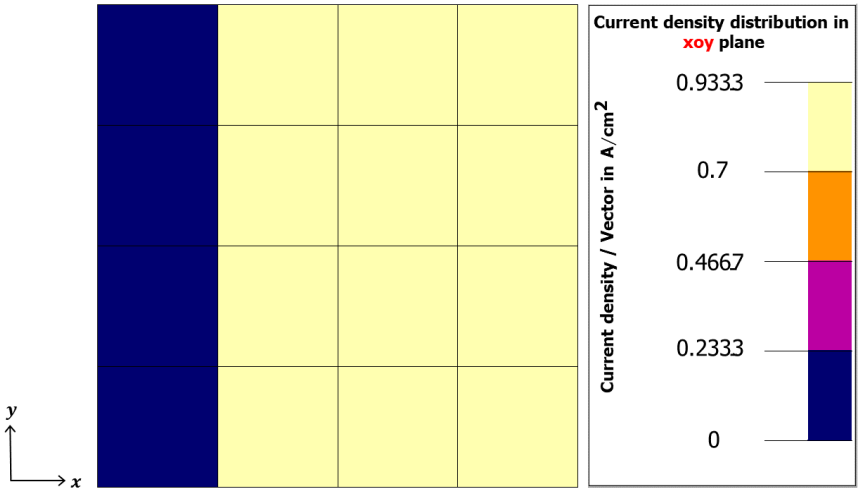

Figure 2.2: Heterogeneous 2D current flow distribution

2.1.3 *Magnetostatic Application*

Considering the conductive volume presented in the geometry , a magnetostatic formulation is used to compute B and H in the study domain around the FC emulator. The magnetic field is created from the DC current flow inside the conducting non-magnetic medium. Some quantities such as the distribution of the magnetic field strength (H), the magnetic flux density (B), which describes the magnetostatic problem in the 3D FEM solver, cover the following elements.

➤ *Boundaries of the studied domain*

The boundary condition is defined by a boundaries or frontiers which explains magnetic potential of the domain. These conditions uses even the infinite box with null magnetic potential at infinity or by symmetries which define the magnetic field at the geometry borders if they are normal or tangential magnetic field. In our model the boundary conditions are defined by a symmetrical default tangential magnetic field.

➤ *Material description of the media*

Material media are modeled by material regions. These regions are explained by there physical properties of the medium Tab(2.1)

Table 2.1: Physical properties of the medium

A region	**Physical Property**
Air or Vacuum	$\mu_r = 1$
Magnetic non Conducting	Hard or soft material $(\mu_r > 1)$
Coil Conductor	Conducting with source non magnetic $(\mu_r = 1)$

In our model, the air region is defined between the conducting medium and the boundary condition frontiers. On the other hand, the coil conductor defines the conductive medium where the current density flows inside each bar of the emulator. In addition, the non-conductive magnetic region explains the ferromagnetic circuit analyzer which will be explained in the following chapters.

➤ *Sources description*

Magnetic and electric types of sources such as permanent magnets, direct electric current and imposed magnetic flux can be used in the magnetostatic application. In our approach, the electric current source DC was considered as a conductive coil type electric current providing a continuous uniform distribution of current density flux inside the emulator bars. The current density flux J generated in the conductive region of the model is considered to be homogeneously distributed in the healthy operating condition of the model. The generated magnetic field is modeled based on steady-state magnetostatic formulations, including Gauss's law for magnetic flux Eq(2.1) and Ampere's theorem Eq(2.2). Furthermore, Eq(2.3) considers the flux density proportional to the magnetic field as a function of the influence of the magnetization of the material that creates the region. Further still, Eq(2.4) presents the boundary condition equation to ensure the uniqueness of the magnetic field calculation in the domain (an external box Γ_B, on which it can be considered that no magnetic flux line passing through).

$$div(\mathbf{B}) = 0 \tag{2.1}$$

$$curl(\mathbf{H}) = \mathbf{J} \tag{2.2}$$

$$\mathbf{B} = \mu_0 \mu_r \mathbf{H} \tag{2.3}$$

$$\mathbf{B}.\mathbf{n} = 0 \quad on \ \ \Gamma_B \tag{2.4}$$

2.1.4 *Ferromagnetic circuit analyzer brief description*

The previous design [49] has the characteristics of a 142×142 mm ferromagnetic analyzer. This geometry still suffers from the problem of experimental adaptation on a 140×140 mm PEMFC in addition to the dimensions of the stack current collectors that can touch the analyzer. Therefore, in our approach the size of the analyzer increases from 142×142 mm to 160×160 mm (see Fig(2.3a)), where $L1 = 24$ mm and $L2 = 40$ mm. This facilitates the implementation of the analyzer around the 140×140 mm PEMFC stack without touching the current collectors of the stack. Furthermore, in our approach, the previous analyzer model has been improved with respect to the sensor air gap area (see Fig(2.3b)).These modifications reduces the implementation of experimental complexity for sensors inside the analyzer.

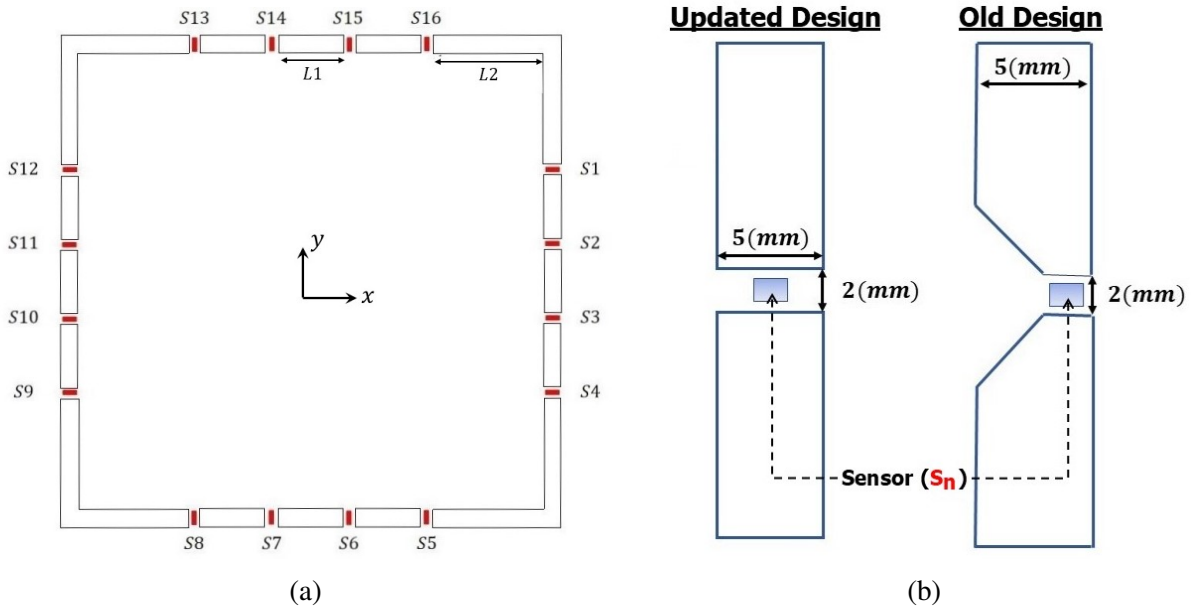

(a) (b)

Figure 2.3: Updated circuit analyzer (a) sensor air gap, and (b) dimensions with sensors distribution

2.1.5 *Numerical and Experimental results*

This model explains the homogeneous and heterogeneous 2D current density flow inside the PEMFC. Thus, regardless of the position of the circuit analyzer around this emulator model, the magnetic field measurement by the magnetic sensors will read the same value. In order to express the homogeneous current distribution (normal operation), each bar of the emulator is supplied with 4.375 A to obtain an overall current of 70 A. On the other hand, the heterogeneous distribution (faulty operation) is explained by blocking the current flow through the bars $(Z1, Z5, Z9, Z13)$ Fig (2.1b) and based on the conservation law of current flow, the remaining normal bars are supplied with 5.833 A to keep the overall current flow equal to 70 A. The external magnetic field generated by the two current density behaviors is measured by the magnetic sensors positioned clockwise with respect to the fault position inside the emulator, see Fig(2.3)).

2.1.5.1 Numerical results

After explaining the 2D fuel cell emulator model, the external magnetic field is computed using the ferromagnetic circuit analyzer in normal and faulty emulator operation conditions. Fig(2.4) demonstrates the magnetic field distribution inside the circuit analyzer and the current distribution inside the emulator in both operation conditions.

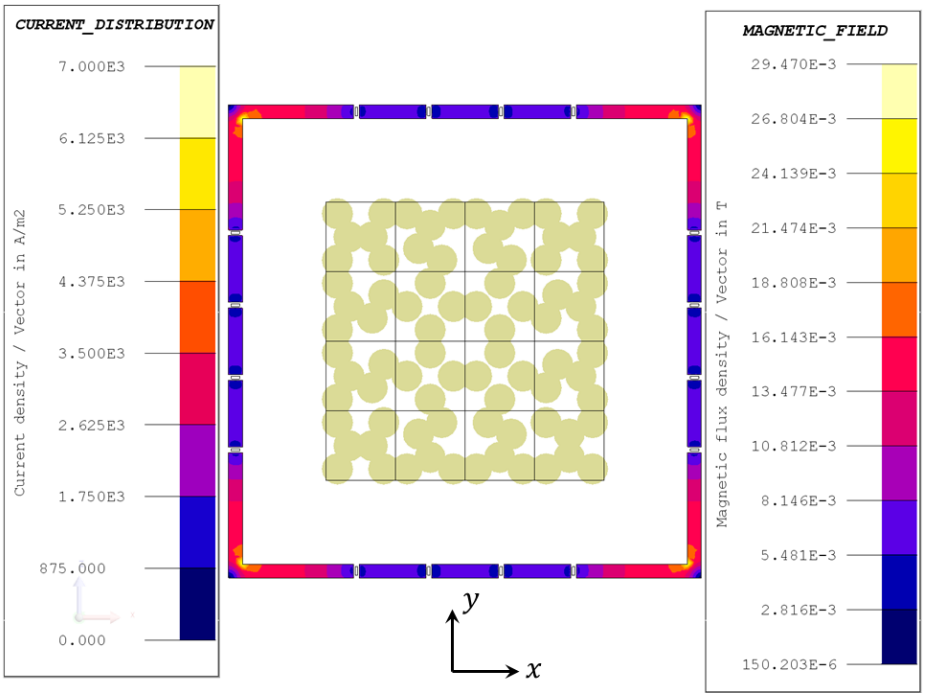

(a)

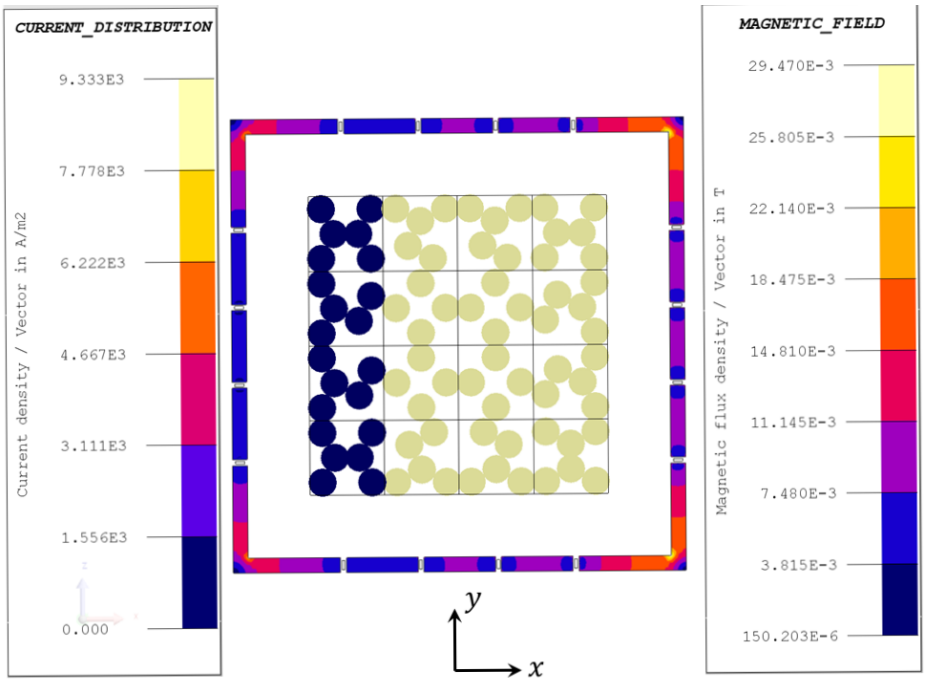

(b)

Figure 2.4: Current distribution inside the emulator with the magnetic field inside the circuit analyzer in both model operation conditions (a) Normal and (b) faulty

Moreover, to illustrate the influence of the circuit analyzer, the magnetic field difference results between both emulator operations at the magnetic sensors level have been presented in Fig(2.5), where Fig(2.5a) and Fig(2.5b) shows the normal and faulty operations conditions with and without the ferromagnetic circuit analyzer.

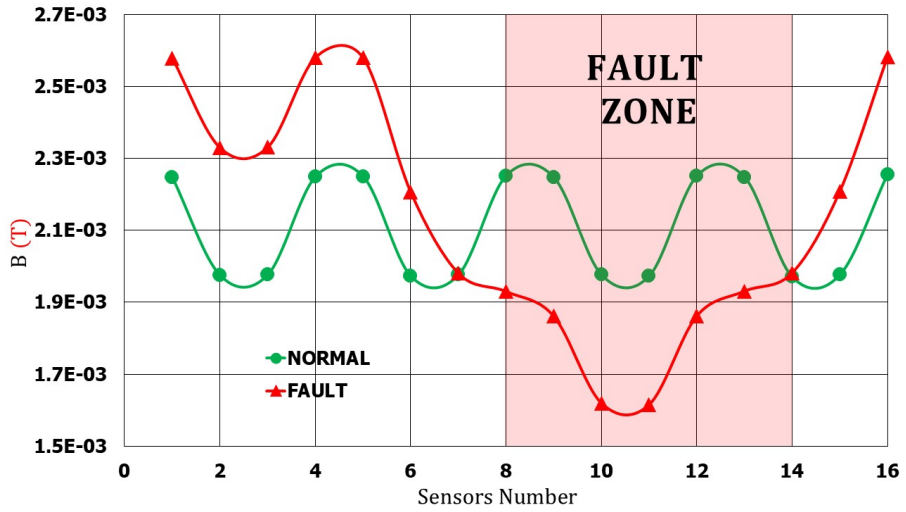

(a)

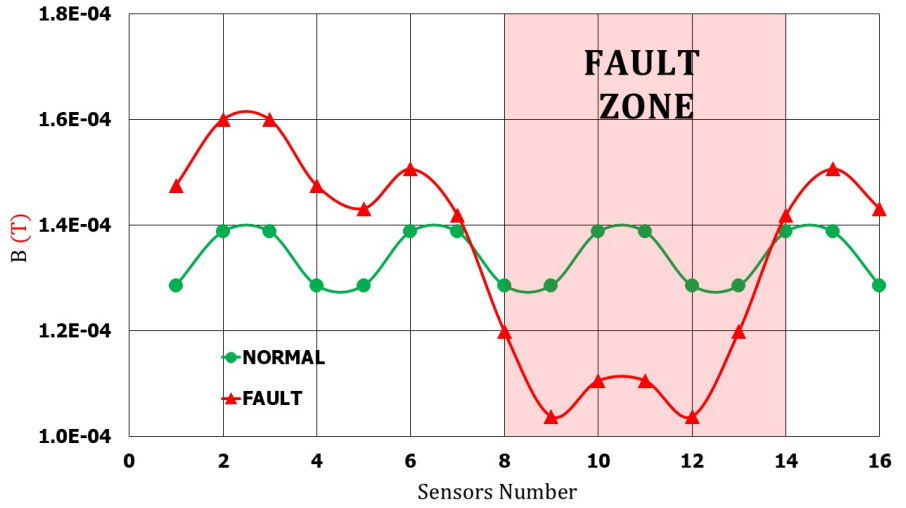

(b)

Figure 2.5: Normal and faulty 2D emulator behaviors (a) with and (b) without circuit analyzer

The magnetostatic analysis shows that the use of the ferromagnetic circuit improves the distribution of the magnetic field produced by the stack operation. The opposite behavior of the sensors between Fig(2.5a) and Fig(2.5b) are due to the different locations of the sensors near distinct volumes of the ferromagnetic material parts. Moreover, Figure (2.6) shows the sensors distribution with and without circuit analyzer around the FC stack. Now based on Ampere's law in current carrying conductor, Eq.(2.5) shows the inversely proportional relation between the measured magnetic vector B at specific sensor and the distance d between the current density vector I at point C Fig(2.6) and the sensor position in case no circuit analyzer is used. In Fig(2.6) the magnetic measurement at S1 is lower than S2, this is due to the distance variation between the two sensors so that d1 in Eq.(2.6) is lower than d2 Eq.(2.7).

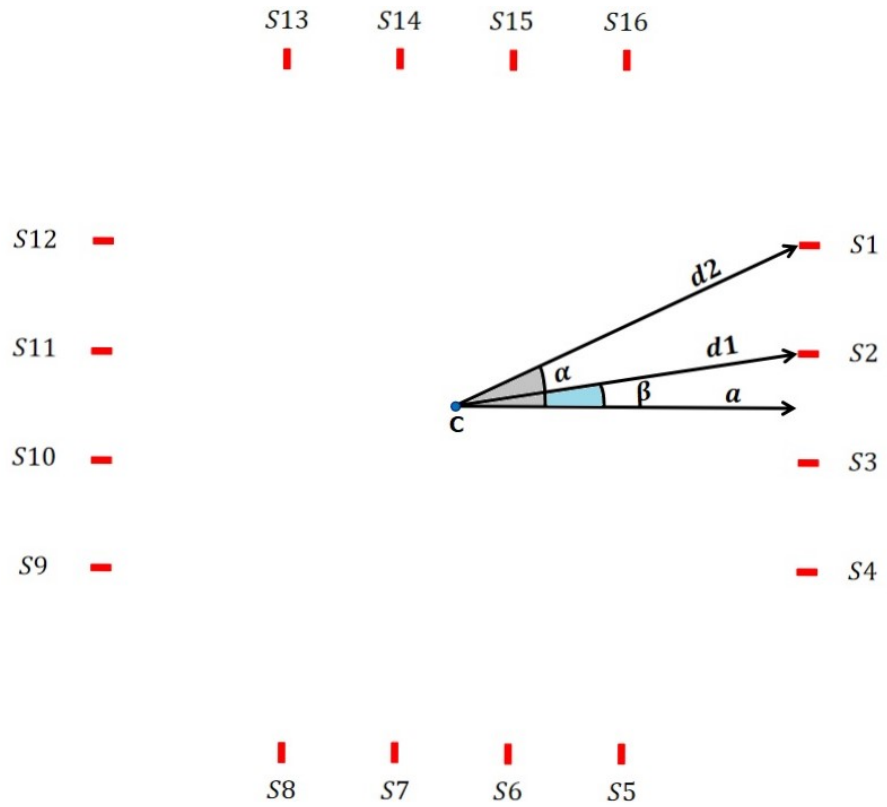

Figure 2.6: Sensors distribution around the FC stack.

On another hand, measuring the magnetic field using the circuit analyzer will inversely affect the magnetic sensors so that the sensors located near the center side of the analyzer (S2, S3) Fig(2.3a) read a lower magnetic value compared to (S1, S4) located near the edges of the analyzer. This phenomenon is due to the presence of the ferromagnetic material (Ni-Fe family) of a bigger volume near (S1, S4) compared to (S2, S3).

$$B = \frac{\mu_0 I}{2\pi d} \tag{2.5}$$

$$d_1 = \frac{a}{\cos(\beta)} \tag{2.6}$$

$$d_2 = \frac{a}{\cos(\alpha)} \tag{2.7}$$

After explaining the circuit analyzer effect on the FC stack external magnetic field measurements, Fig(2.7a) shows a 10 times higher magnetic field difference Δ_B=B_{normal}-B_{Fault} between the two stack operating conditions using the circuit analyzer compared to the Δ_B produced without using the analyzer (see Figure (2.7b)). The fabricated Δ_B decreases the influence of the environmental effect on the magnetic sensors. This phenomenon is only possible when the normal and faulty FC states are measured in the same environment. The positive ΔB is explained by the drop of the magnetic field for the sensors located close to the conduction fault in which the current is 0 A and the negative ΔB values are obtained for the sensors close to the normal part of the active zone. Therefore, in addition to the external magnetic field amplification in both FC stack operation, the circuit analyzer enhances the magnetic field difference Δ_B used for FC stack diagnostic process.

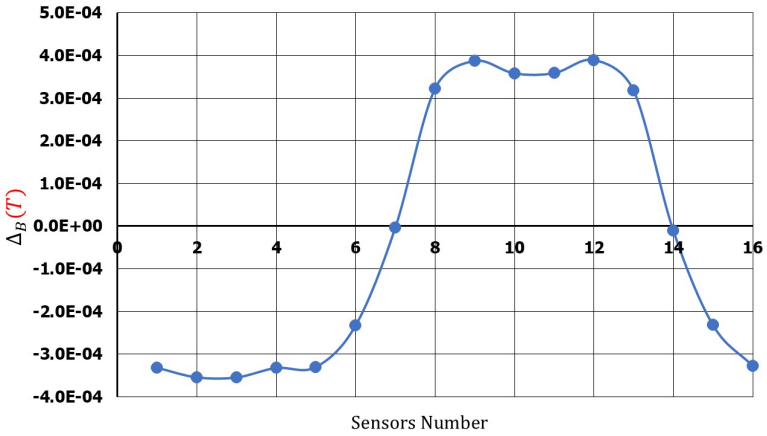

(a)

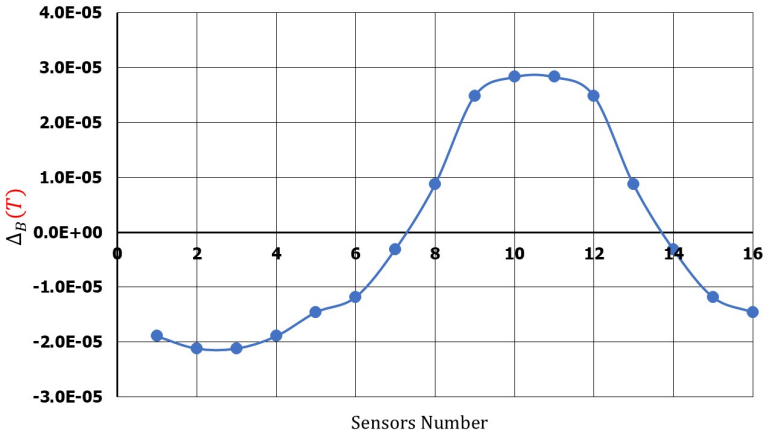

(b)

Figure 2.7: Produced Δ_B (a) with and (b) without circuit analyzer

2.1.5.2 Experimental results

As the effect of the circuit analyzer on Δ_B is explained numerically, the experimental test bench is created to hold the ferromagnetic circuit analyzer around the FC stack emulator Fig(2.8).

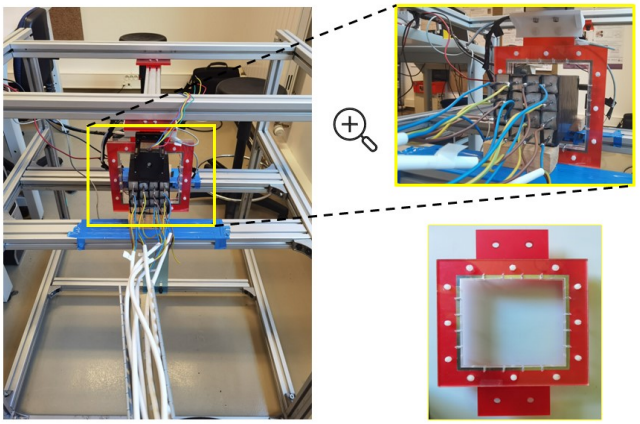

Figure 2.8: 2D emulator experimental test bench

This emulator consists of 16 aluminum bars controlled by a power source to generate the current density flowing through the bars. On another hand, the 16 output voltages proportional to the magnetic field magnitude measured by the sensors, are collected by a National Instrument NI 9205 data acquisition system and LabView software. This data acquisition provides 32 analog inputs with an input ADC (Analog to Digital Converter) resolution of 16 bits. The normal behavior of the FC stack was emulated by a homogeneous distribution of the current among the 16 bars while the faulty operation was emulated by reducing the conductive area by 25% by blocking the current flow through ($Z1, Z5, Z9, Z13$) bars Fig (2.1b), similar to the fault used in the simulated model. To detect the position of the fault, it is necessary to calculate Δ_B at the Hall effect sensors. Figure (2.9a) shows the magnetic field distribution calculated in the two operating conditions of the model. Further, the faulty area is detected by presenting Δ_B (see Fig(2.9b)). Finally, to prove the effectiveness of the model, figure (2.9b) shows the closeness of Δ_B values between numerical and experimental results.

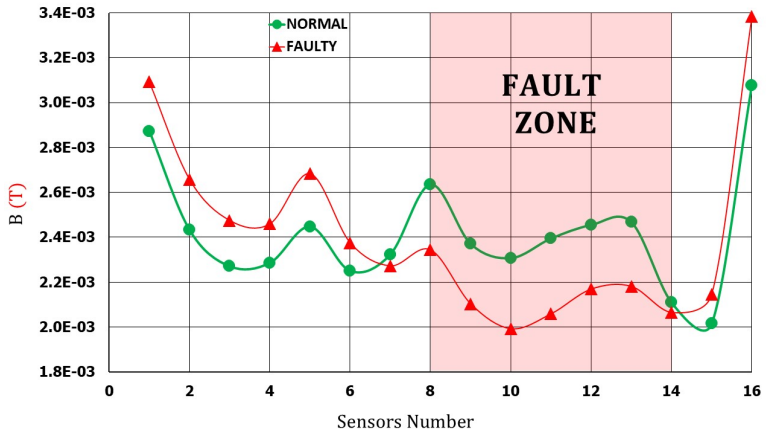

(a)

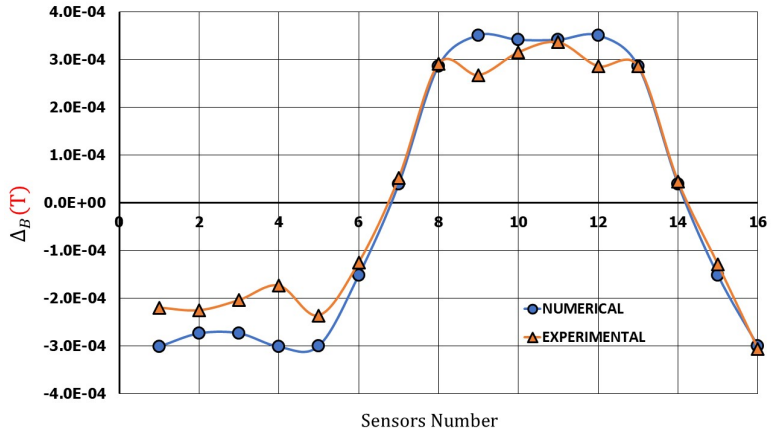

(b)

Figure 2.9: Experimental validation for (a) both FC stack emulator operation conditions (Normal, Faulty), (b) Δ_B compared with the simulated

2.2 3D Passivized PEMFC Model

This model considers a typical PEMFC cell with a current distribution of 70 A. This approach emulates the homogeneity/heterogeneity of the 3D current density flow inside all the plates of the fuel cell using a 3D Transient magnetostatic application model.

2.2.1 *Geometry*

Due to the high resistivity (low conductivity) of the membrane of a FC, our approach was explained by a passivated cell considering that the anodic and cathodic bipolar plates are separated by two GDLs instead of the MEA. The geometrical dimension of each plate inside the stack is presented in Fig(2.10).

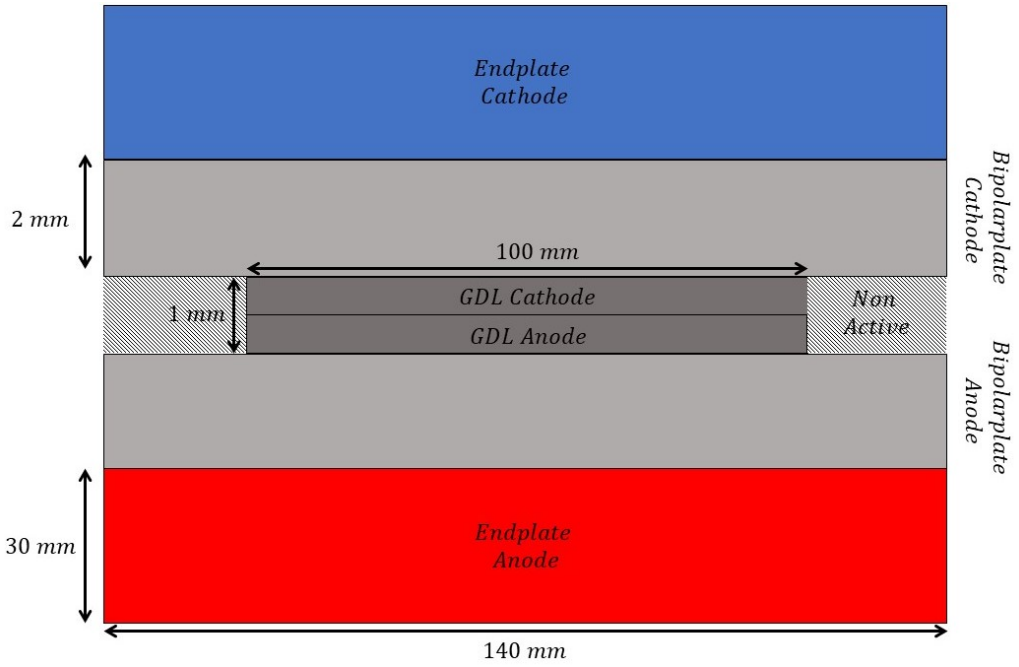

Figure 2.10: Passivized fuel cell dimensions and specifications

2.2.2 *Transient Magnetostatic Application*

The transient magnetostatic application allows to study the magnetic field created as a function of time. The magnetic field produced is due to a variable current density flow inside the model. This application can be applied to different types of devices. In 3D modeling, the interest is to produce a current flow distribution inside the model by using a circuit coupling to provide current between the two end plates of the model. The description of the model in a transient magnetic application follows the same steps as magnetostatics, but with some modifications with respect to the description of materials, conducting media, and source providers.

2.2.2.1 Material description

For the material, a solid coil conductor region is considered in addition to the regions defined in the Tab(2.1), this region is physically explained by a magnetic permeability μ_r and a resistivity ρ. Since the proposed model consists of a set of plates, each with a specific resistivity, then each plate is defined as a solid coil conducting region.

2.2.2.2 Conducting media description

The current density distribution in the transient magnetic application is not uniform compared to the magnetostatic application. This is due to the presence of a skin effect in the conductors used. In this approach, the conductor presented is an active conductor in order to directly feed the model defined

by a solid conductor in a coil by a current source Fig(2.11a). To analyze the current density inside the FC stack, an electric conduction FEM model supplied by a current source has been implemented as shown in Fig(2.11b). In this model, the geometry and the structure of a passivized FC have been used. The physical properties, such as the resistivity of the BP and End Plates (EP), are the same as for the FC materials.

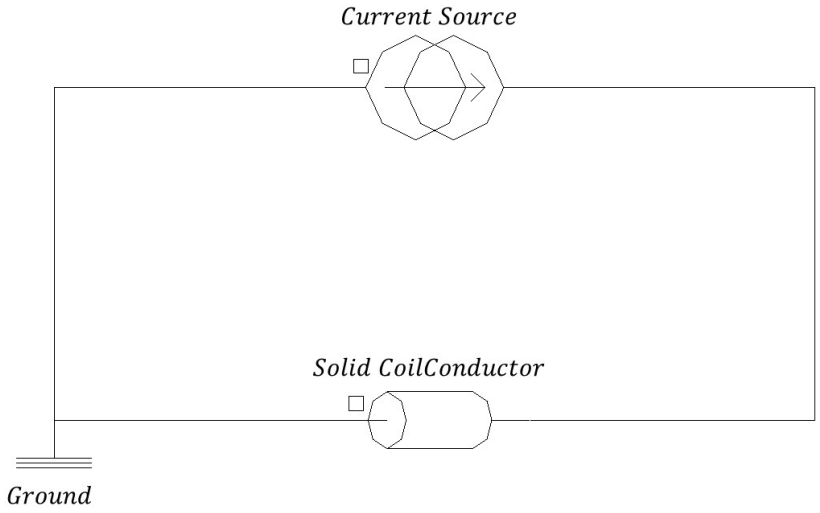

(a)

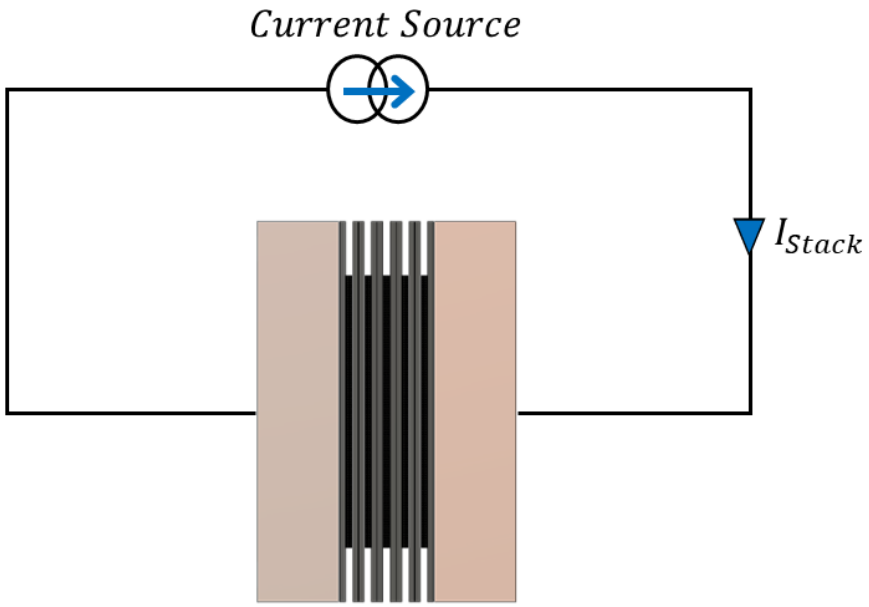

(b)

Figure 2.11: (a) Transient Magnetic application electric circuit, (b) Equivalent electric circuit of the passivated FC stack

2.2.2.3 Coupled Electric conduction and Magnetic formulations

The numerical model of the FC emulator conductive domain is coupled in a circuit with a current source to compute the magnetic flux density distribution B inside and around the conductive domain.

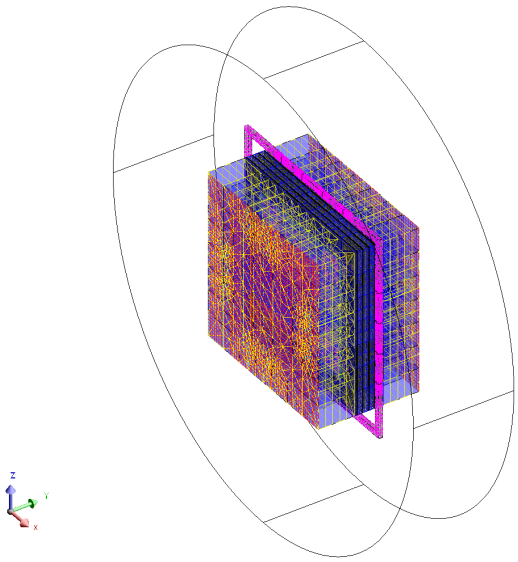

Figure 2.12: Finite element model with boundary conditions

A cylindrical domain has been considered around the FC emulator and external to the magnetic circuit analyzer (see Fig(2.12)). To solve the problem using the FE (Finite Element) method, on the domain borders, two boundary conditions were specified: tangent magnetic field and normal electric field.
A 3D FEM formulation based on magnetic scalar potential, included in Altair Flux software, has been chosen to solve the coupled electric conduction and magnetic equations. As shown in [50], magnetic scalar has good performance for solving problems containing nonlinear massive conductors coupled with circuit equations. Therefore, this method is adapted as we consider 3D conduction defaults included in the conductive domain of the FC emulator.

2.3 A FC realistic 3D current density emulator

The main concept of this model represents a 3D current density emulator model of a FC powered by a current source. This emulator reproduces an equivalent current distribution in a geometric domain similar to the current distribution inside a FC during steady state operation.

2.3.1 *FC structure and electrochemical consideration*

A hydrogen fuel cell generates electrical energy from a redox reaction between hydrogen and oxygen. In the case of a PEMFC (Proton Exchange Membrane Fuel Cell), the electrolyte is a solid polymer allowing the protons mobility. The structure of a PEM single cell is shown in Fig(2.13a): the anode and cathode bipolar plates (1) separated by a membrane electrolyte assembly (MEA). MEA is structured in five layers: the polymer electrolyte membrane (2), two thin conductive catalyst/electrode layers in direct contact with each side of the electrolyte membrane (3) and two porous conductive gas diffusion layers (GDL) ensuring the distribution of gas reactants at the catalyst/electrode level (4). The GDL also forms an electrical connection between the electrodes and the bipolar plates [44]. Bipolar plates design includes gas channels to supply gas reactants at the anode and cathode side. As shown in Fig(2.13b), the hydrogen is oxidized at the anode electrode and releases H^+ ions that migrate through the electrolyte membrane. At the cathode, the oxygen is reduced and combines with H^+ ions forming water. Water is therefore a by-product of the redox reaction. Besides electrical energy, it is worth mentioning that thermal power is also generated by this exothermic reaction.

In a FC stack, multiple single cells are packed in series, to increase the global voltage. The FC stack is bounded by two conductive plates used also to connect the FC stack with the external electric circuit.

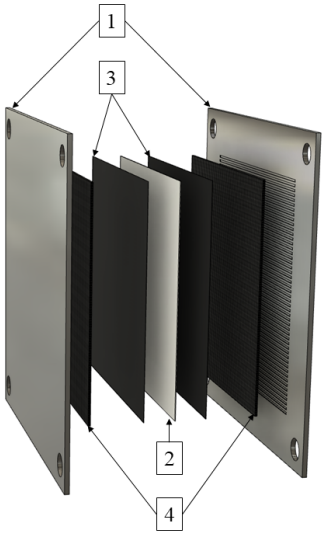

(a)

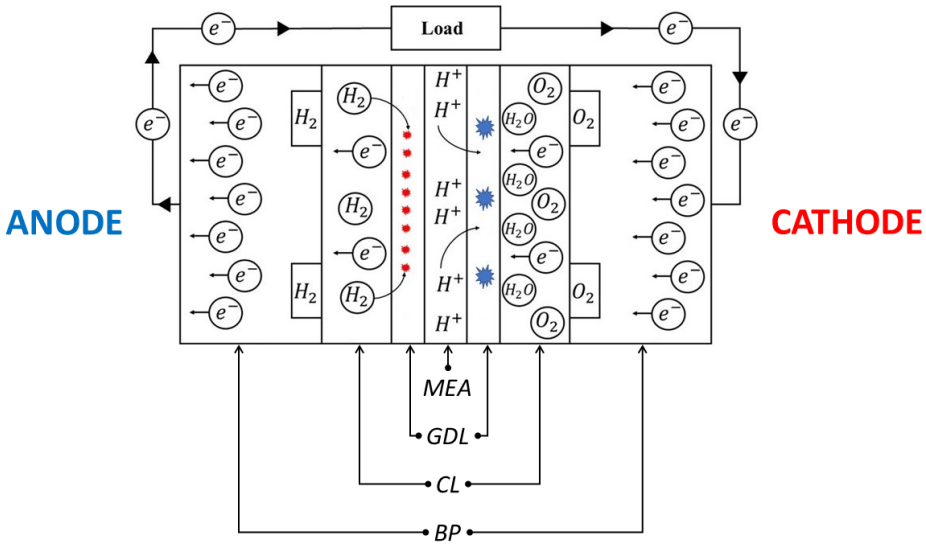

(b)

Figure 2.13: FC structure (a) with the electro-chemical representation (b)

At the level of each single cell, an electrochemical model provides the relationship between the voltage and the global current density at the cell membrane level, $V = f(J)$. This relationship, that can lead to the representation of a polarization curve Fig(2.14), depends on many physical parameters like pressure, temperature, gas stoichiometry, and humidity. This voltage-current density dependency is explained by Eq.(2.8) in literature [5].

$$v(J) = \quad E_{rev} - \quad v_{act} - \quad v_{ohm} - \quad v_{con} \tag{2.8}$$

In Eq.(2.8) E_{rev} represents the reversible voltage given by Nernst equation, depending on cell temperature and on the reactant's partial pressures, v_{act} the activation drop voltage caused by slow reaction at the electrode surface level [5], usually approximated by Tafel equation Eq.(2.9).

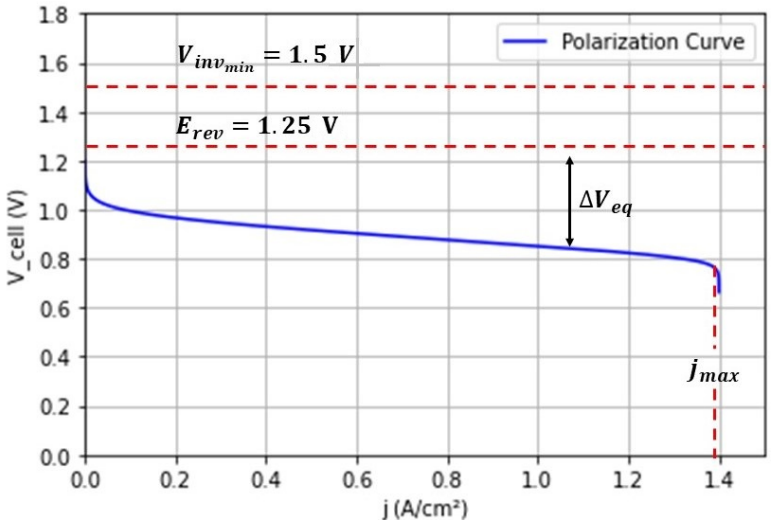

Figure 2.14: FC polarization curve. The dotted red lines indicate the limits of $V_{inv_{min}}$, E_{rev}, and J_{max}

$$v_{act} = \frac{RT}{2F\alpha} \ln(\frac{J}{J_0}) \tag{2.9}$$

Where α is the charge transfer coefficient, R the universal gas constant, T the cell temperature, J_0 the exchange current density at which the over voltage begins to move from zero and F the Faraday constant.

v_{ohmic}, the ohmic voltage drop can be expressed in Eq.(2.10) where ρ_m is the specific ionic resistivity of the membrane, ρ_{GDL} the GDL resistivity, t_m and t_{GDL} represent the membrane and the GDL thickness.

$$v_{ohmic} = J(t_m.\rho_m + 2.t_{GDL}.\rho_{GDL}) \tag{2.10}$$

v_{con}, the concentration voltage drop Eq.(2.11) in [5] results from the reduction of concentration of the reactants on the electrodes. The influence of v_{con} can be observed in Fig(2.14) when the current density J is close to the maximum value J_{max} causing a failure in the transport of enough reactant to the electrode surface.

$$v_{con} = \frac{RT}{2F\alpha} \ln(1 - \frac{J}{J_{max}}) \tag{2.11}$$

Inside the FC, at the level of the MEA, the current flow is ensured by the electrons flow at the level of the conductive GDL and by the hydrogen ions flow inside the membrane electrolyte. Electron-ion exchange occurs at the electrodes (catalyst layers) level. The electrolyte membrane, coated by electrodes, is covered by a GDL on both sides as shown in Fig(2.13a).

If ρ_{GDL} can be considered constant, the ionic resistivity of the membrane ρ_m depends on the current density, temperature and membrane hydration. In Fig(2.14) the dependence $V = f(J)$ has been obtained from Eq.(2.8) to Eq.(2.11) using the parameters presented in Table(2.2) given by experimental study presented in [51].

Table 2.2: Main parameters for the polarization curve [51]

$E_{rev}(V)$	$J_{max}(A/cm^2)$	$J_0(A/cm^2)$	$T(°C)$	α
1.25	1.4	8.8×10^{-8}	60	0.5

Another electrochemical aspect considered in this analysis consists in the impossibility of an inverse current density at the level of the electrolyte membrane, even for a fault zone of the electrolyte membrane producing a lower reversible voltage than the overall cell voltage. As shown in Fig(2.14), a reverse current in the electrolyte assumes a voltage between the electrodes of the cell,$V_{inv_{min}}$, exceeding the activation losses in addition to the reversible voltage, which is not possible. For example, in the conditions mentioned in Tab(1), even for a very low current density value $V_{inv_{min}} = 1.5(V)$.

2.3.2 *Current density distribution inside the real FC and the proposed emulator*

The aim of this work would be to be able to diagnose a sampled selection of fuel cell stacks coming out of a production line, reducing therefore time-to-market times for fuel cell manufacturers. Before being able to consider the evaluation of the proposed diagnosis methodology on actual fuel cell stacks, it is to generate a current distribution current distribution similar to FC in a similar geometry and structure, in a passivated device powered by an external current source. Fig(2.15) illustrates the homogeneous and heterogeneous current density distribution that can arise in the PEMFC stack. Since the current density distribution is directly related to the ionic flux inside the fuel cell electrolyte, its evaluation gives important information about the health of the cell. The distribution of this current density over the surface of the fuel cell has attracted the interest of many fuel cell designers. In this approach, the current flow distribution inside a real PEMFC and our passivated FC emulator is presented.

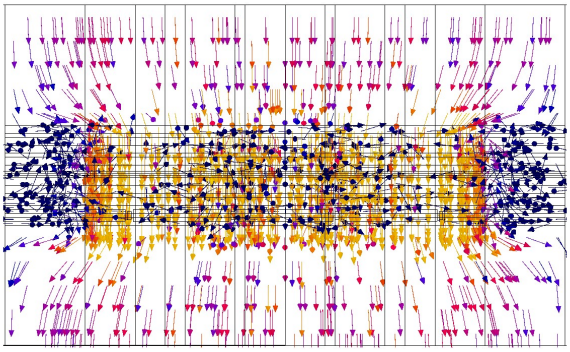

(a)

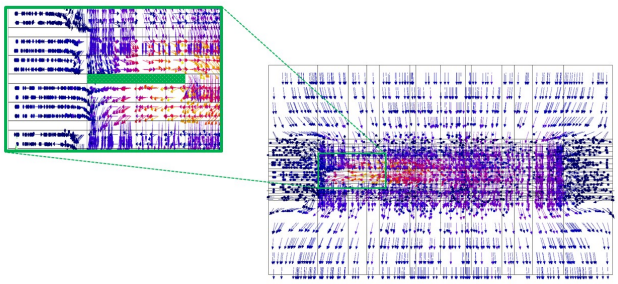

(b)

Figure 2.15: Homogeneous and heterogeneous current density distribution in both (a) Normal and (b) Faulty stack operation conditions

2.3.2.1 Inside a real PEMFC stack

In Fig(2.16a), the electrolyte surface of the cell discretized into n elements explains the heterogeneous distribution of current flow due to the difference in conductivity on the electrolyte surface. For each

surface element i, an equivalent circuit (see Fig(2.16b)) corresponds to the equation (2.8) which explains the polarization curve of the fuel cell is associated with the series connection of the three parts of the resistive curve with one linear (Ohmic) and two non-linear (active, conduction) resistivities.

Even if there is a significant voltage drop between the operating conditions of the fuel cell, the conduction of a reverse current is not possible. Then, only a positive current density is possible at the electrolyte membrane, for each surface element, a diode was also added in the equivalent electrical circuit of the MEA. To analyze the current for n surface elements of the FC, once we can observe two situations in Fig(2.16b) circuit:

- If $E_{rev_i} < V_{cell}$ then $I_i = 0$ which can be equivalent with a very high resistivity of $R_{eq_i} = R_{act_i} + R_{ohm_i} + R_{con_i}$
- If $E_{rev_i} > V_{cell}$ then $I_i > 0$

In the FC circuit Fig(2.16a) the current $I_1, I_2, \ldots, I_n$ can be expressed by:

$$I_i = \begin{cases} \dfrac{E_{rev_i} - V_{cell}}{R_{act_i} + R_{con_i} + R_{ohm_i}}, & \text{if } E_{rev_i} > V_{cell} \\ 0, & \text{if } E_{rev_i} \leq V_{cell} \end{cases}$$

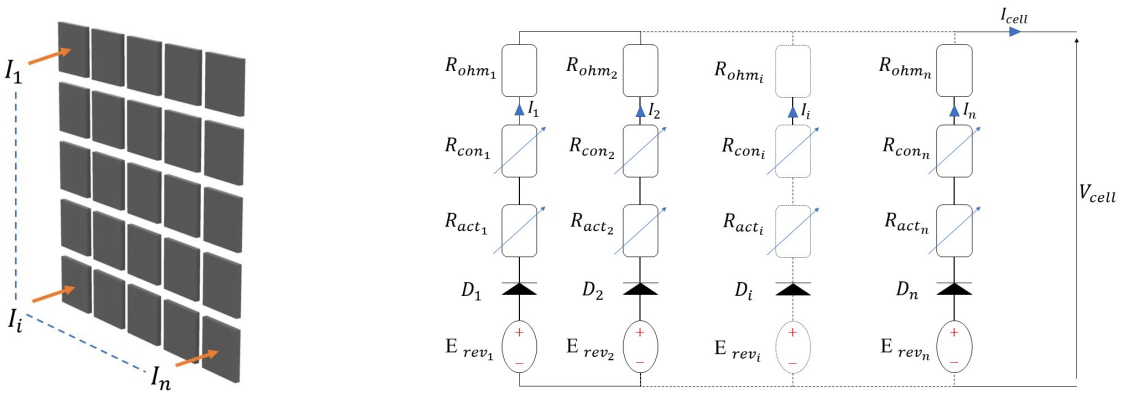

(a) (b)

Figure 2.16: Descretized current density corresponding to n surface elements at the electrolyte level (a) electric circuit representation for the current density distribution inside real FC (b)

2.3.2.2 Inside the 3D emulator model

As the currents $I_1, I_2, \ldots, I_n$ have the same direction, identical values can be obtained in the equivalent circuit presented in Fig(2.17) by passivizing the cell model given in Fig(2.16b).

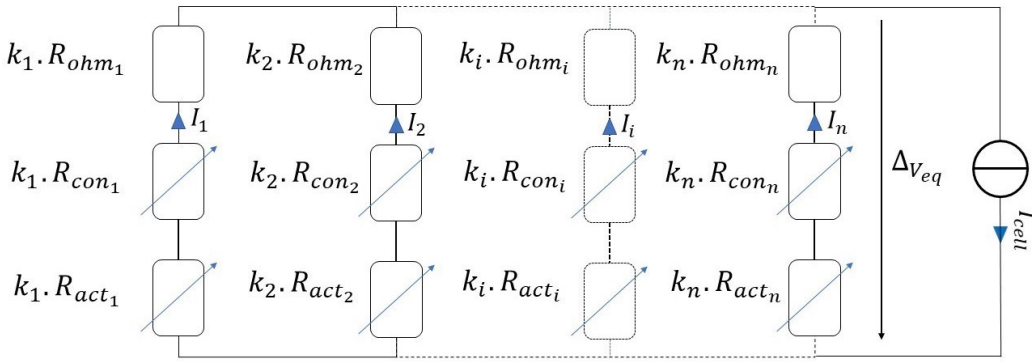

Figure 2.17: Passivized FC Electric circuit

This model keeps resistive components multiplied by a corrective constants $k_1, k_2, \ldots, k_n$. These factors can be obtained using the FC circuit and the passivized circuit.

Identical current values can be obtained in the passivized FC emulator Fig(2.17) circuit after expressing the corrective constant k_i by:

$$k_i = \begin{cases} \dfrac{\Delta V_{eq(normal)}}{E_{rev_i} - V_{cell}}, & \text{if } E_{rev_i} > V_{cell} \\ \infty, & \text{if } E_{rev_i} < V_{cell} \end{cases}$$

Where $\Delta V_{eq(normal)}$ is the supplying voltage source that can be considered by the difference between the cell reversible voltage and the considered value of the cell given in Eq.(2.12), when Temperature (T) and Pressure (P) are considered at a homogeneous value for the part of the cell in normal operation.

$$\Delta V_{eq}(J) = E_{rev}(T, P) - V_{cell}(J) \tag{2.12}$$

Creating a simplified current density distribution, similar to that inside actual FC, makes it easier to study the magnetic field generated by the PC, and implicitly by the FC operation.

2.3.2.3 Electric conduction problem of the passivized FC

In this model, the geometry and the structure of a passivized FC has been used. The physical properties such as the resistivity of the BP and EP are the same as for the FC materials. Two approaches have been used to analyze the current density distribution inside the FC emulator: a realistic FC behavior, and a simplified FC behavior.

A realistic behavior is obtained by using the electric field characteristics at the membrane level. $E(J)$ computed by Eq.(2.13) ,where $\Delta V_{eq}(J)$ characteristics is given by Eq.(2.12) to obtain the non-linear active area behavior represented in Fig(2.18) where d_{mem} [51] is the membrane thickness and satisfies Eq.(2.13).

$$E(J) = \frac{\Delta V_{eq}(J)}{d_{mem}} \tag{2.13}$$

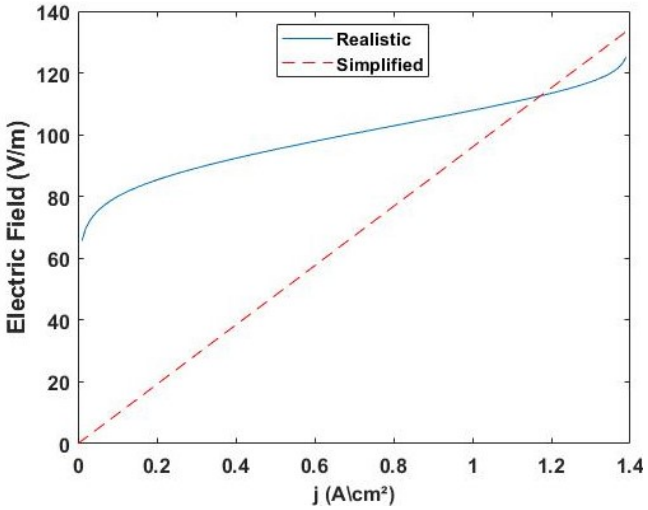

Figure 2.18: Membrane electric field characteristics of the realistic and simplified emulator

In the simplified approach, a linearized $E(J)$ is considered by the means of an average resistivity MEA presented in [51] as shown in Fig(2.18) . In this paper, the simplified model is explained by the Passivized Cell PC where the active area is considered by only two GDLs. This GDL resistivity has been computed depending on an experimental test done which measures ΔV_{normal} between two BP after supplying our emulator with 70 A to calculate after that ρ_{GDL} using ohms law and equation Eq.(2.14) respectively.

$$R = \rho_{GDL} \frac{t_{GDL}}{A_{GDL}} \tag{2.14}$$

Where t_{GDL} is the GDL thickness and A_{GDL} is the surface area of the GDL.
Table(2.3) represents the main physical and geometric features of the emulator as well as for the ferromagnetic circuit analyzer. The value of the $\mu_{r_{Ferro}} = 741$, has been measured experimentally for very low magnitude of the flux density , lower than 10 (mT).

Table 2.3: Features of the FC stack emulator and ferromagnetic analyzer

Plates	Materials	Resistivity ($\Omega.m$)	μ_r	Dimension (mm^2)	Thickness (mm)
End plate	Aluminium	2.65×10^{-8} [52]	1	140×140	30
Bipolar Plate	Graphite	3×10^{-5} [52]	1	140×140	2
GDL	Carbon cloth	Normal: 6.0571×10^{-3}	1	100×100	0.5
		Fault: Insulator Infinite			
Ferromagnetic	Ni-Fe Family	___	741	160×160	3

To prove the effectiveness of the simplified emulator, the next paragraph will analyze and compare simulation and experimental results. For experimental and simulation results, the difference between the external magnetic field obtained for different behaviors of the emulator, in normal and faulty operating conditions, was evaluated. These measurements are performed with the ferromagnetic analyzer at different positions around the emulator through the 5-cell fuel cell stack Fig(2.19).

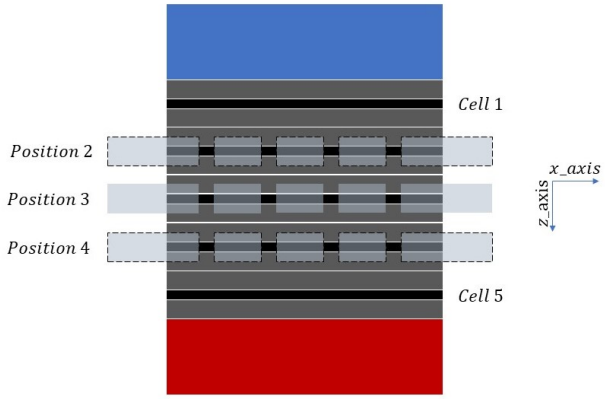

Figure 2.19: Different analyzer positions across z-axis

2.4 Experimental and numerical modeling results

Based on the electrochemical characterizations and the current density distribution inside the FC, this section presents the experimental measurements of the external magnetic field used for the diagnostics of the passivated FC model. The experimental results were compared with the simulation results to validate the effectiveness of the used diagnostic method.

2.4.1 *Experimental setup and results*

In order to obtain a current distribution comparable to that inside the FC volume, Fig(2.20a) presents the test bench created in order to hold the ferromagnetic analyzer around the simplified emulator which have a similar geometry and structure as an actual FC stack. This emulator consists of a passivized PEMFC stack of 5 cells connected with two copper bars at both end plates levels (see Fig(2.20b)). These bars are used to supply the emulator by $I_{stack} = 70$ A.

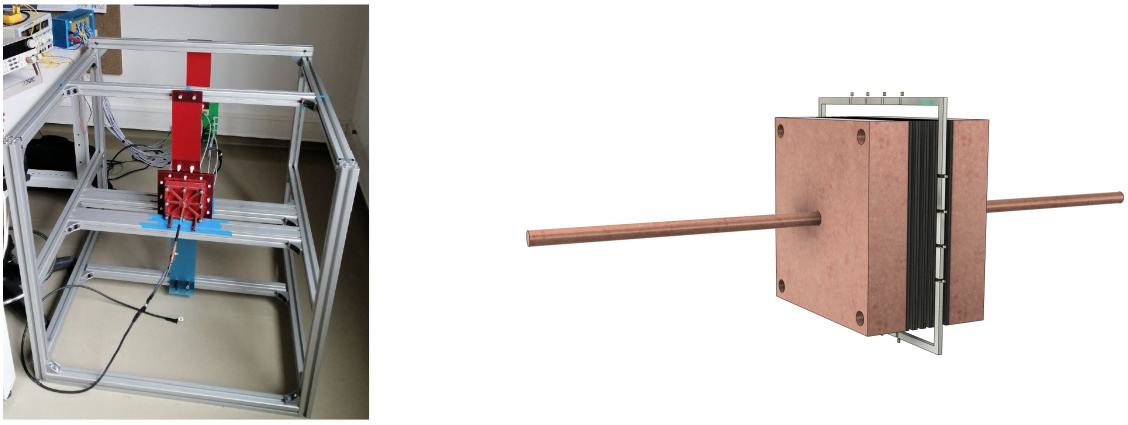

(a) (b)

Figure 2.20: Passivized FC (a) test bench, (b) FC stack emulator and magnetic analyzer

In this experiment, the conduction fault covering 25% of the third cell active area is realized by three polyethylene insulator foil positioned to the left of the GDL of the third cell of the stack. These insulators have been inserted at the front, middle and back of the two GDLs to ensure that the current will not flow through this faulty area (see Fig(2.21c,2.21d)).

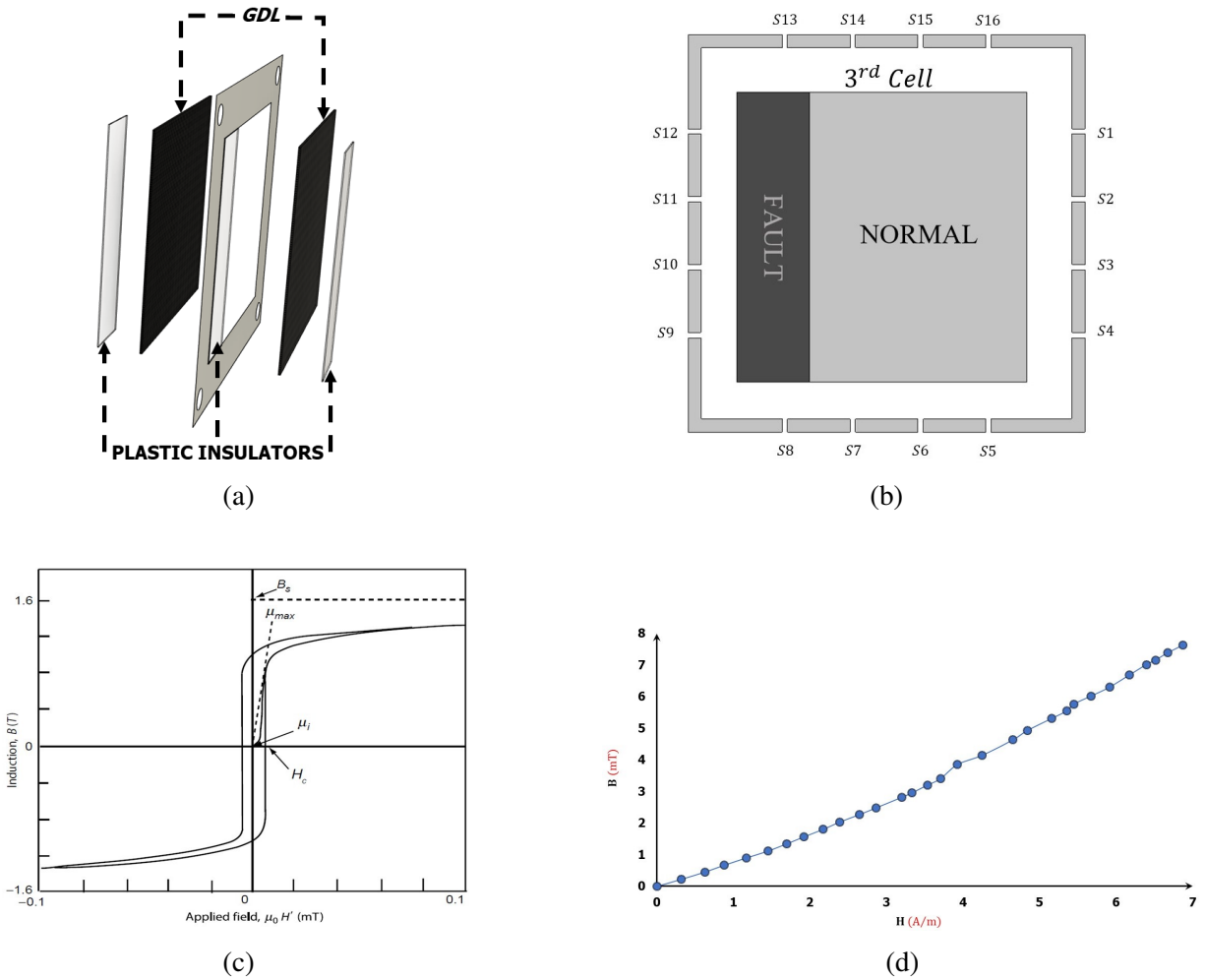

Figure 2.21: (a) Active area with the fault type, (b) circuit analyzer with sensors, (c) difference between μ_i and μ_{max} for soft magnetic materials [53], and (d) characterization of the ferromagnetic material used in the analyzer.

One important aspect to model the magnetic field analyzer was to take into consideration the specific magnetic behavior of a soft ferromagnetic material, especially for a low magnitude of the internal magnetic field intensity. As shown in Figure(2.21c) [53], the initial permeability, μ_i, at the origin of the hysteresis loop is smaller than the maximum permeability value, μ_{max}, attained for a slightly larger intensity of the magnetic field. Therefore, the real characteristic of the mumetal material composing the ferromagnetic circuit of the analyzer has been experimentally characterized, by measuring the magnetic flux density in the airgap of a toroidal core, with a helical winding. The obtained characteristic $B(H)$ shown in Figure(2.21d) has been realized for a very low magnitude of the flux density, lower than $10mT$, which is in the range of the magnetic analyzer measurements. In this interval, the $B(H)$ can be considered linear $B = \mu_0\mu_r H$ with an average value of the relative permeability μ_{rFerro} = 741, much lower than the maximum value of the mumetal relative permeability catalog value μ_{max} = 10^5.

Using the ferromagnetic analyzer presented in 2.1.4, this magnetic analyzer is placed at three different positions, around *cell* 2, *cell* 3 and *cell* 4 (see Fig(2.19)) to measure the external magnetic field generated. This analyzer is based on a high permeability material, Mu-metal ferromagnetic which is a soft material nickel-iron alloy with 16 non-magnetic air gaps in which the linear Hall effect (SS94A1F-type) sensors are inserted. This type of sensors is characterized by an output voltage 4 V at zero magnetic flux density with a high sensitivity of 25 mV/G. The 16 output voltages proportional to the

magnetic field magnitude measured by the sensors, are collected by a National Instrument NI 9205 data acquisition system and Lab-VIEW software. This data acquisition provides 32 analog inputs with an input ADC (Analog to Digital Converter) resolution of 16 bits. The experimental measurements recorded the magnetic field magnitude measured by the magnetic sensors $B = [B_1, B_2, ..., B_{16}]$ placed in the ferromagnetic analyzer air gap.
The stack was powered by a power source controlled at EP levels to ensure an overall stack current of 70 A. Magnetic field measurements are performed in both operating modes for the emulator, the normal behavior as $B_{Normal} = [B_{N1}, B_{N2}, ..., B_{N16}]$ and conduction fault behavior as $B_{Fault} = [B_{F1}, B_{F2}, ..., B_{F16}]$ at the different analyzer positions. Fig(2.22a) represents the magnetic field magnitude of the passivized stack behavior under normal and faulty conditions when the ferromagnetic analyzer is around the affected cell (Position 3). In order to test the change in the internal J between normal and faulty operation, $\Delta B = B_{Normal} - B_{Fault}$ must be analyzed.

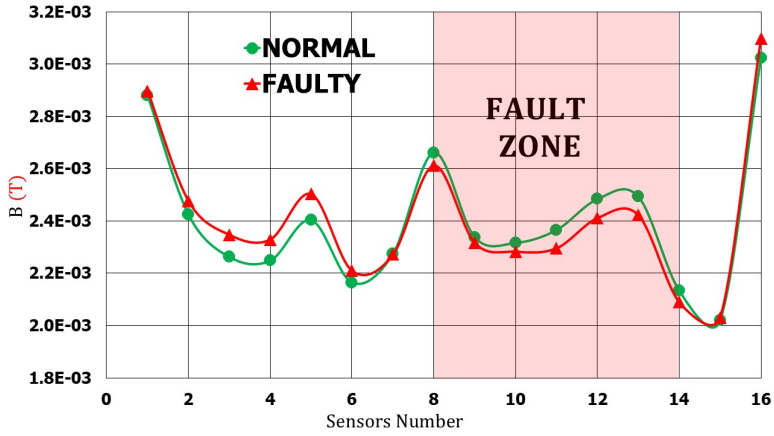

(a)

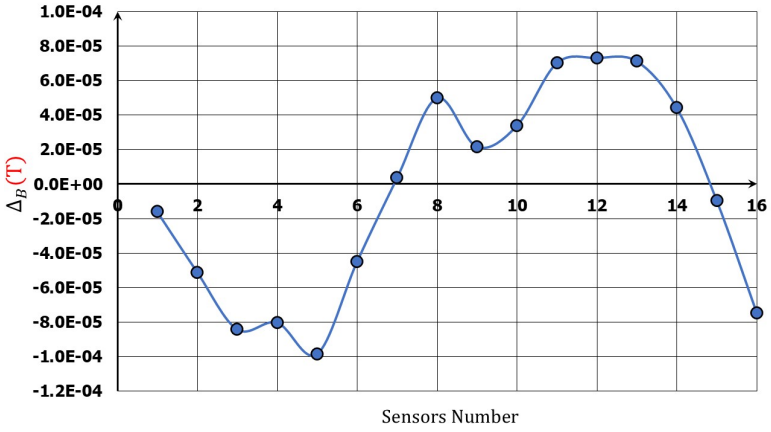

(b)

Figure 2.22: Experimental representation for (a) normal and fault emulator, (b) 3D Δ_B

2.4.2 *Numerical modeling and results*

Based on the experimental findings, the numerical model is developed to justify the 3D fault detection using. During the faulty conditions, the external field is measured with different analyzer positions, around cell 2, cell 3 and cell 4. Subsequently, the experimental result of ΔB is fairly compared with the simulation when the circuit analyzer is around cell 3 to highlight the accuracy of the proposed emulator. This numerical model is based on the strong coupling between the electrical conduction application that solves the current density flow inside the FC emulator and the magnetic application

that calculates the internal and external magnetic field generated from the internal current density flow in the emulator domain.

2.4.2.1 Fault cell detection using 3D magnetic field measurements

In this section, a fault of the simplified model like the one explained in experimental section has been used by considering an affecting 25% of the left active area of the third cell in the stack (see Fig(2.23a)) , and a ferromagnetic analyzer around the stack with 16 air-gap to attach the magnetic sensors, to measure the external magnetic field around each cell Fig(2.21d) across different z-axis positions Fig(2.19). The fault was considered as an insulator to block the current flow through the affected part of the active area. This fault may affect neighboring cells (cell 2 and cell 4) due to the short distance between these cells and the position of the fault, resulting in a more heterogeneous current density within these cells compared to the other cells (see Fig(2.23b)) .

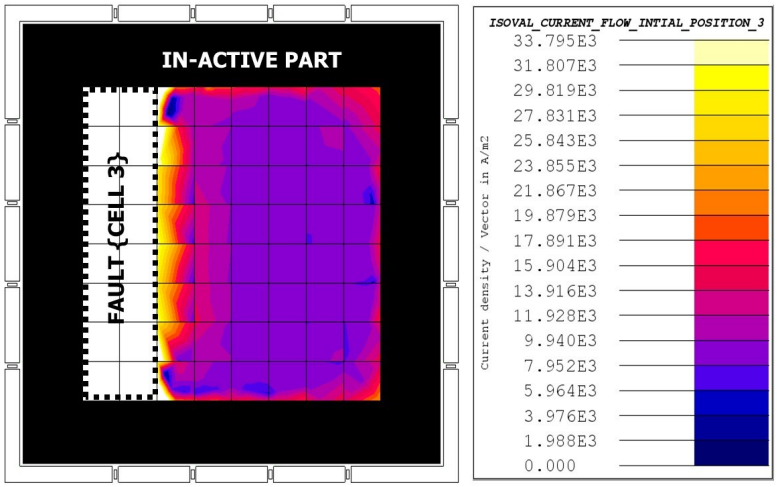

(a)

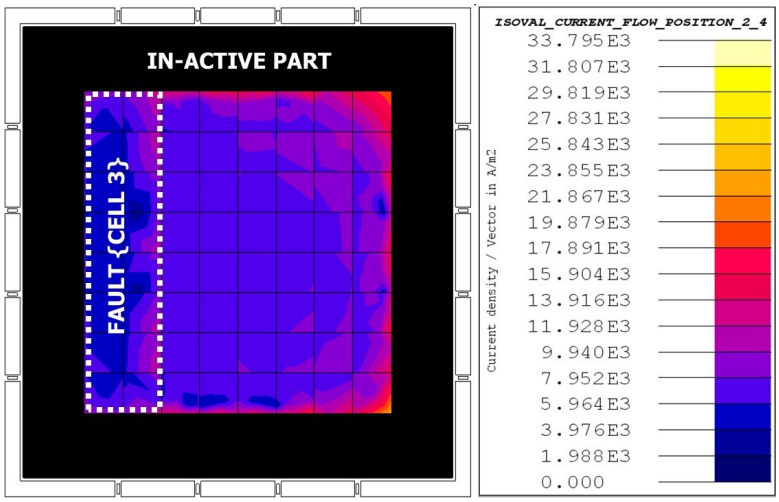

(b)

Figure 2.23: Fault design in (a) 3^{rd} cell and its effect on the current density distribution on the neighbors cells (b) 2^{nd} and 4^{th} cells.

In this study, Fig(2.24a) illustrates the magnetic fields obtained in simulation with explains the simplified model in the two behaviors of the emulator, normal and faulty. Furthermore, the Δ_B result of comparing the simulation (simplified and realistic) and experimental at Position 3 Fig(2.19) of the

circuit analyzer is presented in Fig(2.24b). We can observe that Δ_B has a similar shape between simulations and the experimental emulator.

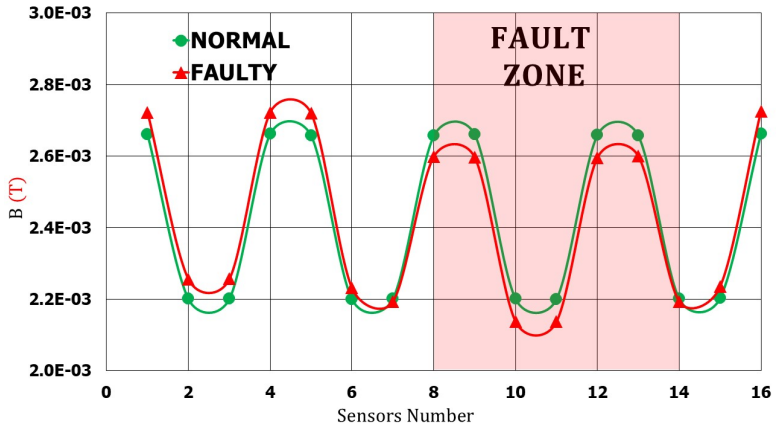

(a)

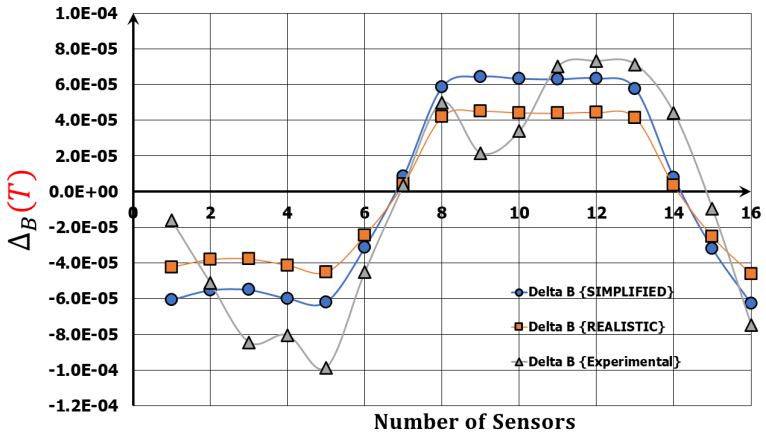

(b)

Figure 2.24: Passivized FC model (a) numerical Normal and Faulty operation condition and the Δ_B simulation (simplified and realistic) and experimental at the level of the 3^{rd} cell

The positive ΔB represents the magnetic field drop for the sensors located near the fault line zone, where the current in the affected part drops, resulting an increase in the current density flux producing a negative ΔB in the remaining unaffected part. On another hand, the multivariate observations between different analyzer positions are given by a vector of ΔB_s measured by the magnetic sensors in both emulator behaviors and the Euclidean distance exposed in Eq.(2.15), where $n_s = 16$, the number of the magnetic sensors inside the analyzer.

$$\mathcal{E} = \sqrt{\sum_{i=1}^{n_s} (\Delta B_{s_i})^2} \tag{2.15}$$

The experimental and simulated 3D magnetic field faulty detection for $\mathcal{E}$ experimental and $\mathcal{E}$ simulated are presented in Fig(2.25a) and Fig(2.25b) respectively. The maximum value of the average $\mathcal{E}$ is around the fault position (cell 3) in both simulated and experimental results, and starts to decrease at the near the affected neighbor cells which become far from the position of the fault. This is due to the current drop in the fault region at the third cell which affects also the flow of the current inside the near cells.

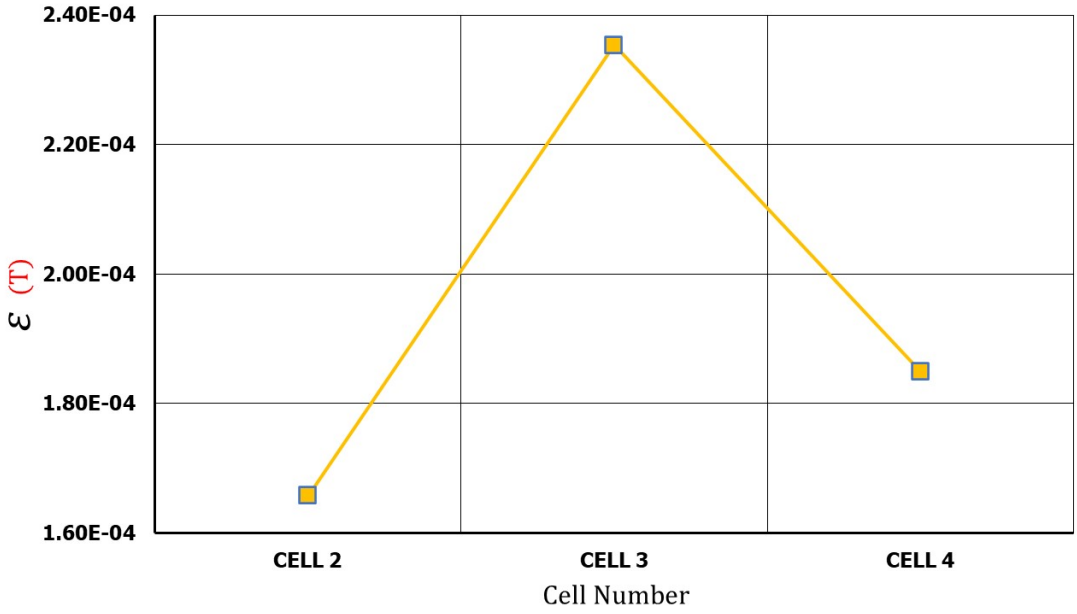

(a)

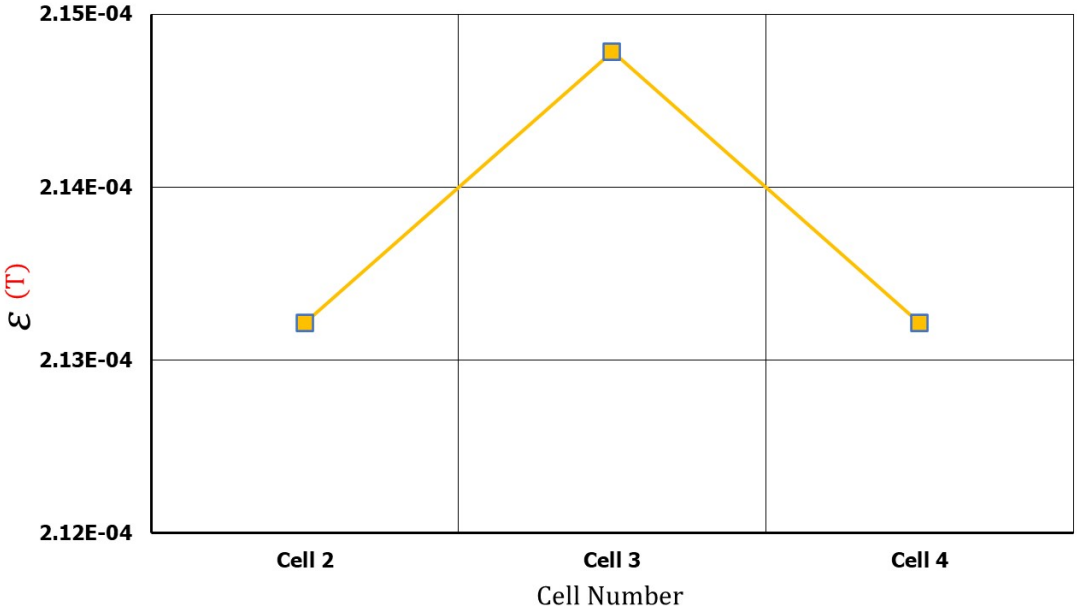

(b)

Figure 2.25: Passivized FC model 3D fault detection (a) experimentally measured and (b) numerically proved.

2.5 3D aluminium bar PEMFC model

Based on the real current density flow inside PEMFC stack, the proposed emulator explains a 3D current density within $100cm^2$ active cell surface area of the stack. The FC emulator was explained by two aluminum bars of , the first one was considered as uniform Fig (2.26a), which expresses the normal behavior of the active area of the FC stack, while the second bar is to explain the faulty FC stack by cutting 25% of the width of the aluminum bar in the middle of the emulator through the z-axis Fig (2.26b).

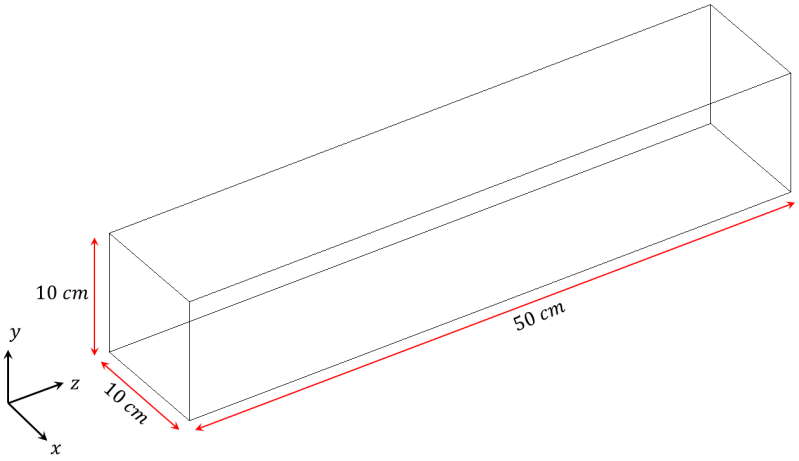

(a)

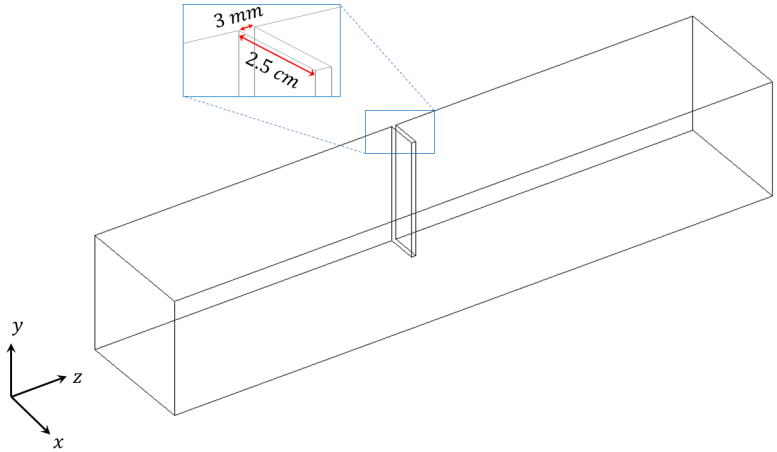

(b)

Figure 2.26: Finite Element Simulation (FES) aluminium bar model in (a) Normal, (b) Faulty states.

2.5.1 *Current flow behavior inside the proposed emulator*

As the local current is directly related to several physical and geometrical parameters of the FC, its evaluation can give significant information on the health status of the FC. A non-homogeneous distribution of the current density of a FC can be the cause of various operating problems such as membrane degradation, non-homogeneity of hydrogen in the electrolyte and clogging of the gas channels. In our study, to emulate the homogeneity/heterogeneity of the current distribution, a constant total current equal to $I_{AL-BAR} = 70A$ is supplied to the aluminum bar in normal and faulty bar behavior. In the normal situation, the current density inside this bar is considered to be homogeneous Fig (2.27a). On the other hand, the heterogeneous current distribution in the faulty condition was explained by cutting 25% of the width of the aluminum bar to create an air gap that generates a small deviation of the current flow along the z-axis.

2.5.2 *Numerical measurements*

In this model, using the square analyzer design, the external magnetic field produced by the current flow Fig(2.27) in both model operating conditions. First, the circuit analyzer was positioned around the fault level. Then, a 3D magnetic fault detection was applied by moving the analyzer to different positions along the length of the aluminum bar.

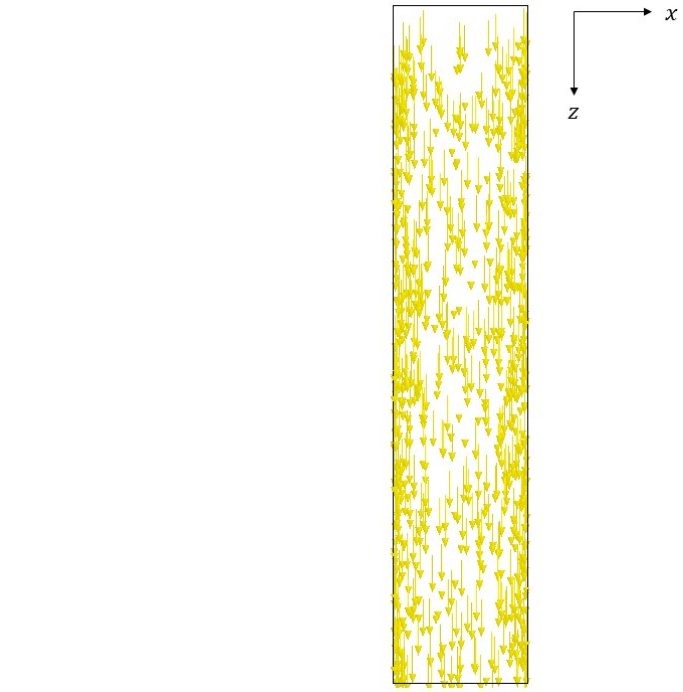

(a)

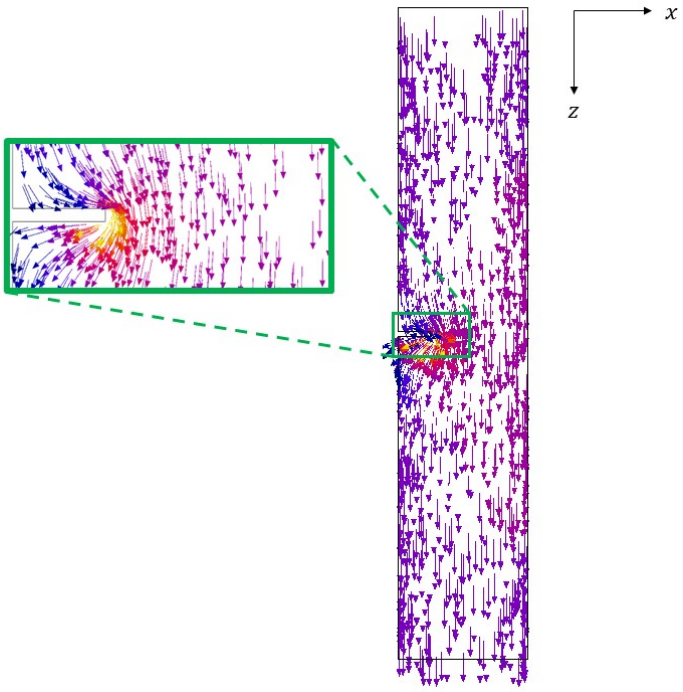

(b)

Figure 2.27: FES Homogeneous and heterogeneous current flow inside (a) Normal and (b) Faulty emulator bar behaviors.

To prove how much the magnetic sensors inside the circuit analyzer designs are accurate in detecting the current flow deviation presented in Fig(2.27), first, it is important to make a 2D external magnetic field measurements around the stack emulator, see Fig(2.28).

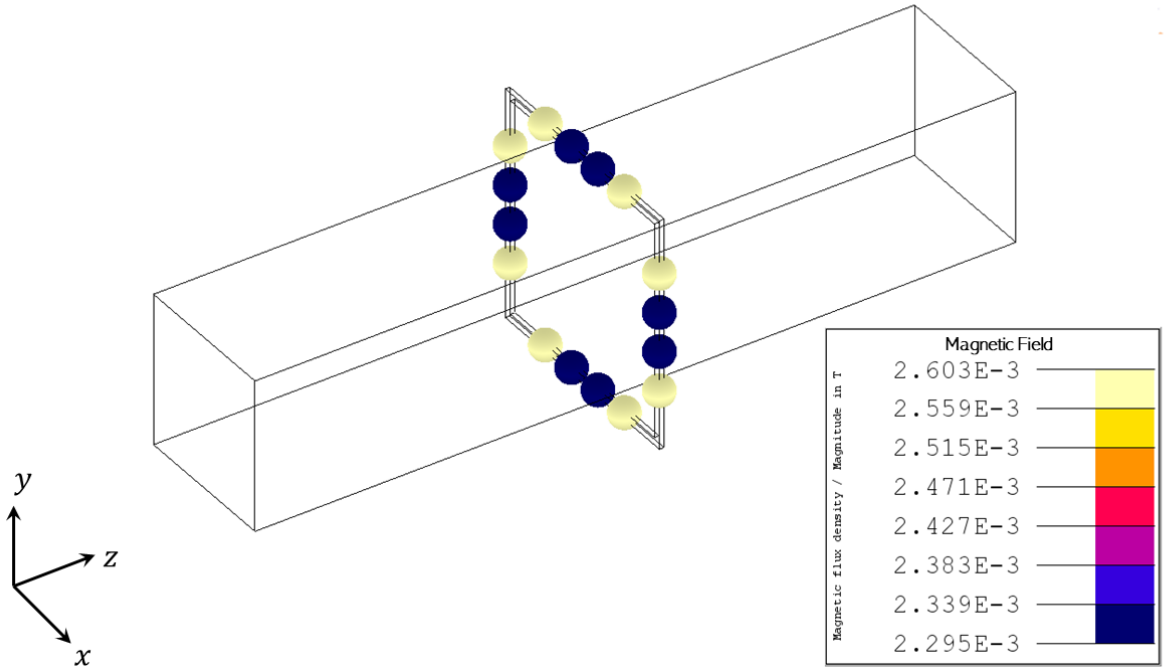

(a)

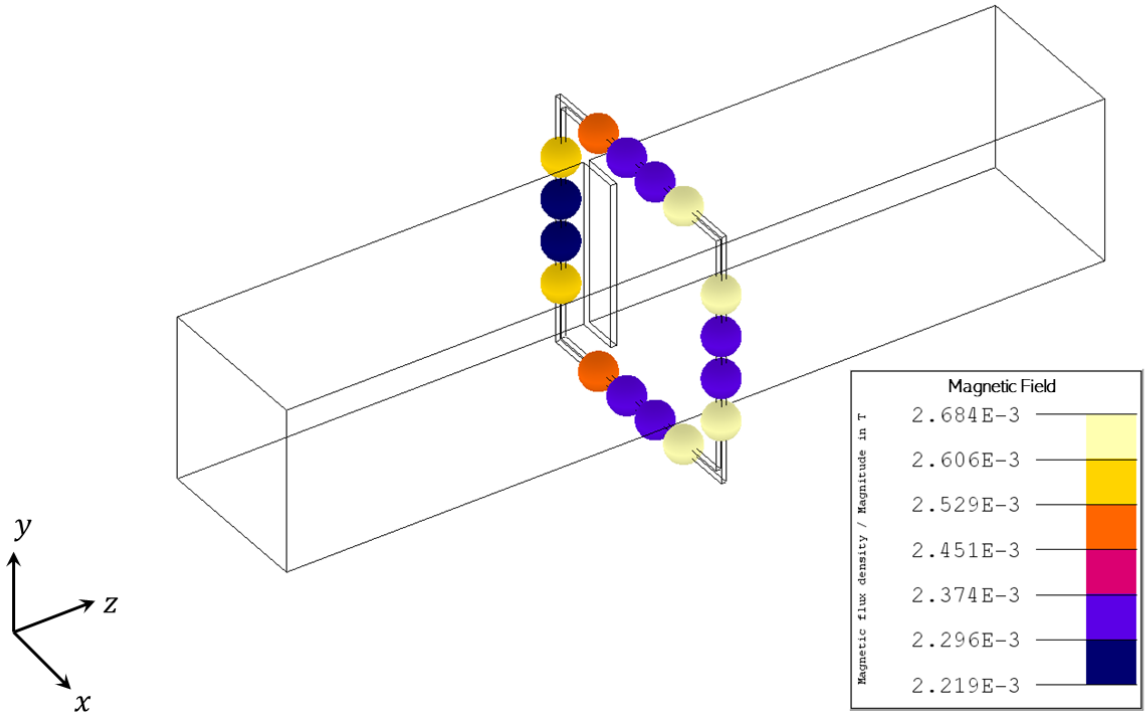

(b)

Figure 2.28: FES aluminium bar external magnetic field in (a) normal, and (b) faulty operation conditions of the stack emulator around the fault level.

Based on the model operation conditions, the external magnetic field and the produced Δ_B at the level of the fault Fig(2.26b) was obtained using the square design see Fig(2.29a) and Fig(2.29b). The lower Δ_B amplitude compared to the Δ_B results obtained in 2D emulator is the current flow deviation across the main axis around the fault position.

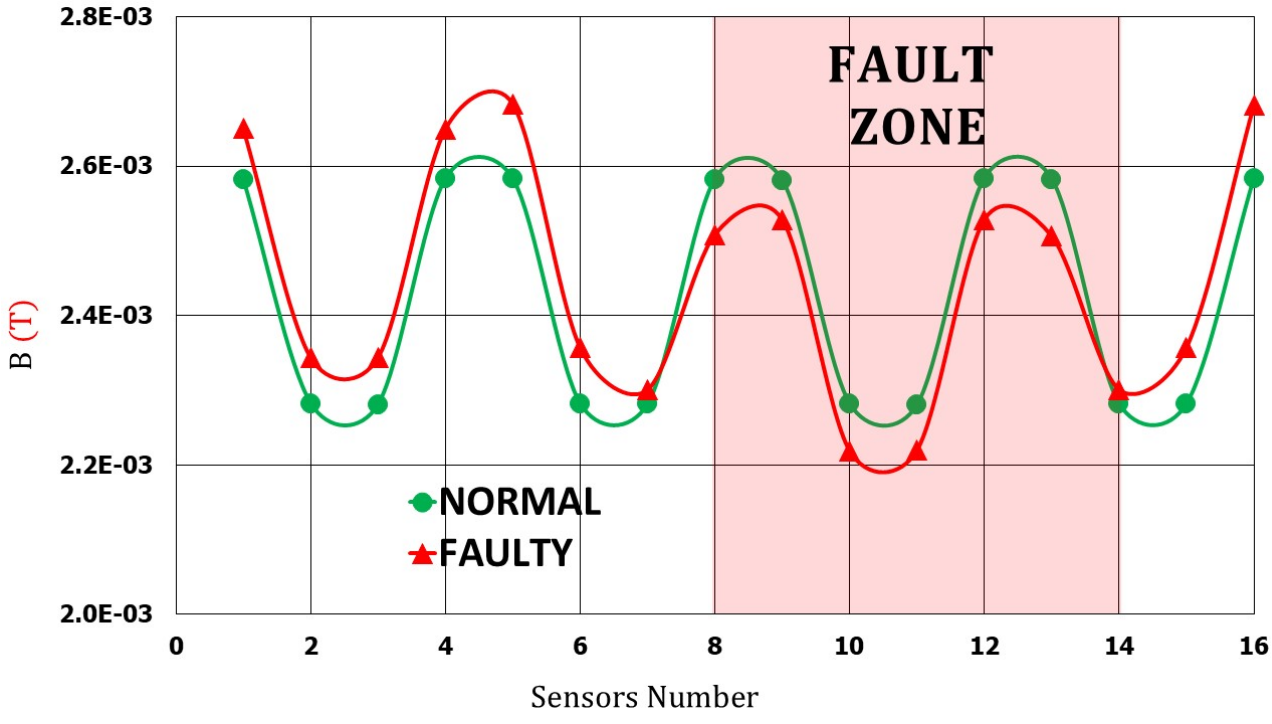

(a)

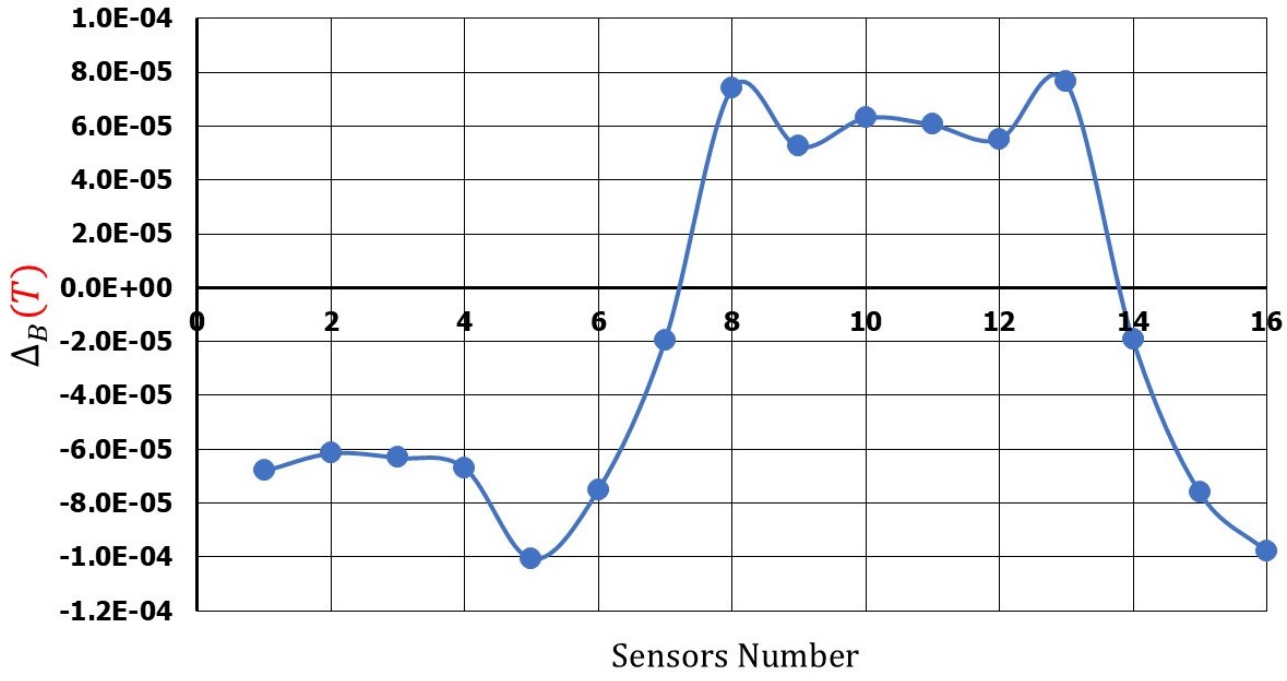

(b)

Figure 2.29: Aluminium bar external magnetic field (a) normal and faulty conditions with the (b) produced Δ_B using the default square design.

On another hand, the measurement of the external magnetic field at different positions of the default square analyzer around the stack model is explained as a 3D fault position detection. To prove the effectiveness of this method in detecting the position of the fault along the length of the stack, Fig(2.30a) shows the 9 different positions of the circuit analyzer with respect to the faulty stack model presented in Fig (2.26b).

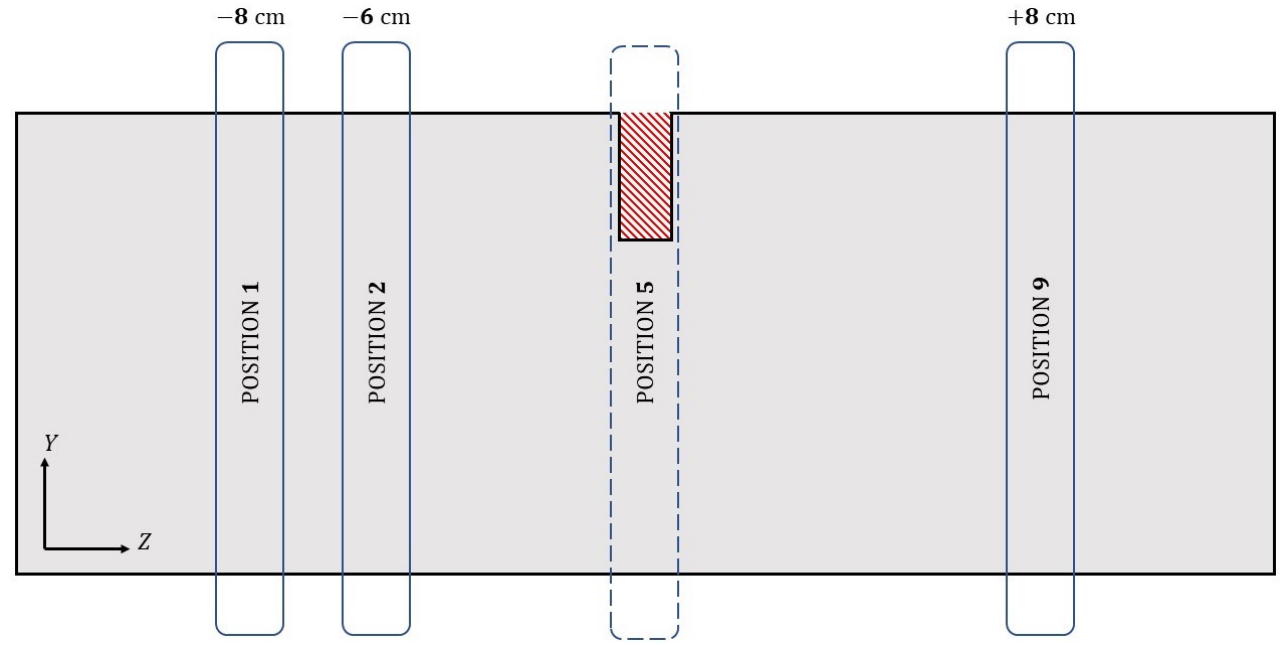

(a)

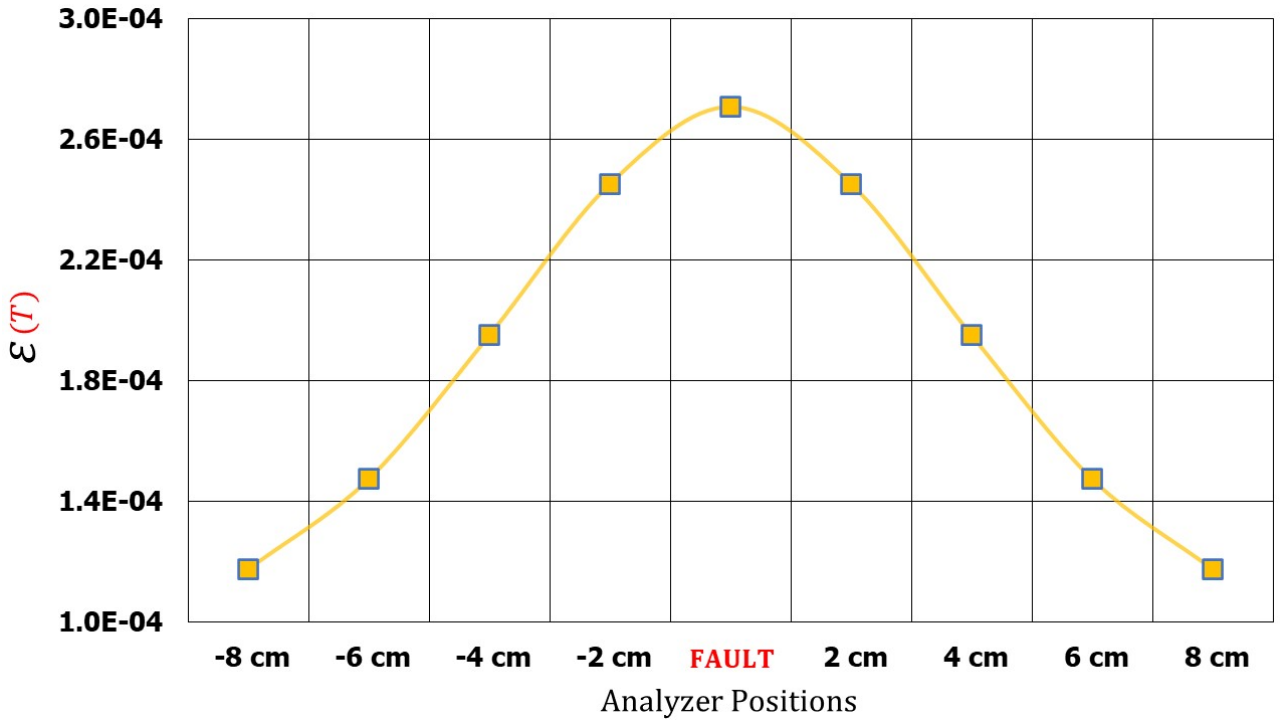

(b)

Figure 2.30: Aluminium stack model of (a) different Analyzer positions around PEMFC stack model, and (b) $\mathcal{E}$ of different positions.

In addition, Fig(2.30b) illustrates the 3D magnetic field fault detection for $\mathcal{E}$. The high $\mathcal{E}$ amplitude at **Position 5** is due to the maximum external magnetic field variation (Δ_B) when the circuit analyzer is positioned at the fault level around the stack model.

2.6 Conclusion

After presenting the electrical representation of the 2D and 3D current flow distribution inside our emulator and how this emulator behaves similarly to the behavior of a real FC, this chapter explains the methodologies used to study a 2D and 3D fault detection based on a set of external magnetic field measurements around the 16 bars, passivated FC, and the aluminium bar emulators. The objective of this work was to develop the FC noninvasive diagnostic methodology based on the measurement of the external magnetic field surrounding the stack. After a literature review on FC diagnostic and on FC current distribution assessment, an improved magnetic analyzer has been proposed. This analyzer amplifies the magnetic field around the cell to perform an accurate detection of the fault position. The main contribution of this work was the concept of an innovative fuel cell magnetic field emulator especially designed to duplicate current density distribution and the produced magnetic field of a real FC stack. The sensitivity of our diagnostic tool is based on three main categories characteristics: conductive fault, Δ_B, and ferromagnetic analyzer. First, the conduction fault is generated to explain the 2D and 3D heterogeneity current distribution inside the FC. Second, the circuit analyzer is used to amplify the external magnetic field to give a higher external magnetic field amplitude at the sensors level. Third, the measured value at each FC state of health are subtracted from the normal state to produce Δ_B. The fabricated Δ_B decreases the influence of the environmental effect on the magnetic sensors. This phenomenon is only possible when the normal and faulty FC states are measured in the same environment.

CHAPTER 3

DIAGNOSIS FOR PEMFC BASED ON AN ORTHOGONAL ARRAY DATA-DRIVEN APPROACH

This chapter discusses an off-line fault diagnosis of the PEMFC. The input data for the diagnostic approach were extracted from the external magnetic field difference Δ_B of PEMFC in the presence of the ferromagnetic circuit analyzer as shown in Fig(3.1). For each state, an initial current distribution will model the state of health of the FC. If for the normal operation, this current density is considered homogeneous, in a fault case, this current distribution will model the magnitude and the position of the fault. In order to obtain a higher statistical relevance, with a reduced number of experiments, for each state from the initial current distribution J, an experimental design will generate a list of variations around this initial current distribution. The obtained data-set is then used as input parameters in both experimental emulator and the numerical Finite Element Simulation (FES) model. For each experiment, the vector containing the values of the magnetic field analyzer will be labeled with the considered state of health of the FC, and added to the experimental training dataset. Similarly, a training dataset based on the FES model is obtained by computing the magnetic field.

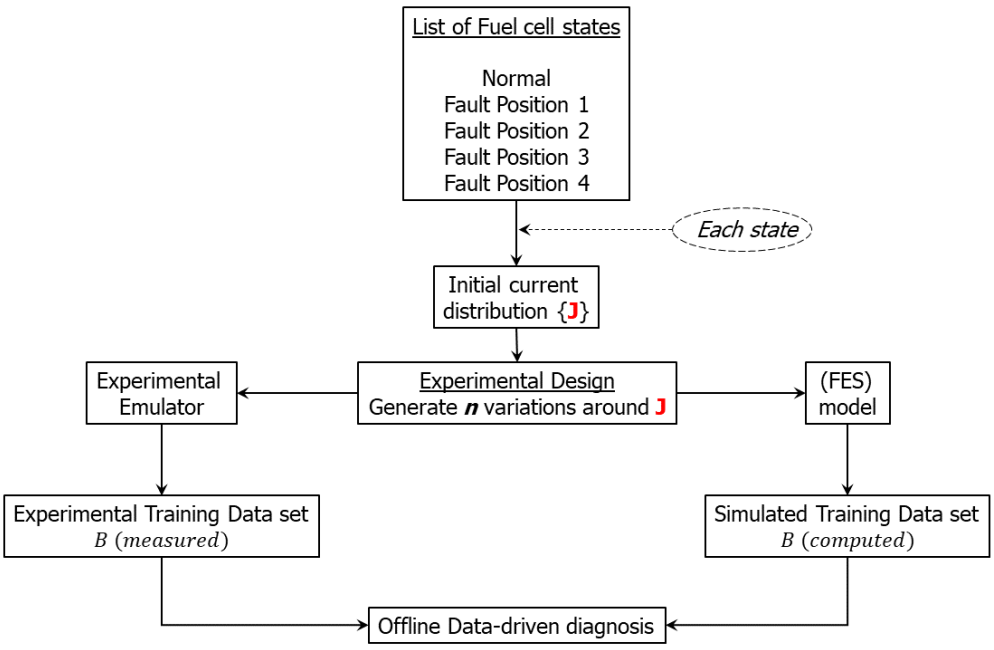

Figure 3.1: Methodology used

This dataset was used as training data for classification and feature extraction learning algorithms. Principal component analysis (PCA), Kernel Principle Component Analysis (KPCA) and Linear Discriminant Analysis (LDA) are used to reduce the dimension of the constructed vector Δ_B and extract features useful for the classification. Support vector machine (SVM), k Nearest Neighbor (kNN) and Decision Tree (DT) are used to classify the data into classes based on the labeled data.

The rest of this Chapter is organized as follows. Section 1, explains the diagnosis principle and how the data-driven array is build based on an orthogonal experimental design. Section 2, addresses the diagnosis strategy by presenting the feature extraction and classification machine learning methods. Section 3 is devoted to present the diagnosis accuracy when the training dataset is generated by the experimental stack emulator or by numerical model. Section 4 discussed the graphical representation of the diagnosis accuracy. Finally, a conclusion is drawn in Section 5.

3.1 Diagnosis principles

The proposed diagnostic procedure requires two internal stages: Labeling the training data and training the diagnostic algorithm. These two stages can be realized offline, preparing and training the diagnostic algorithm. Based on the labeled data section, the training data set can be labeled into k classes, where k describes the normal and different faults behaviors of the emulator. Once trained, the diagnostic algorithm is tested on new random data to predict the accuracy of the algorithm in detecting FC emulator operating conditions.

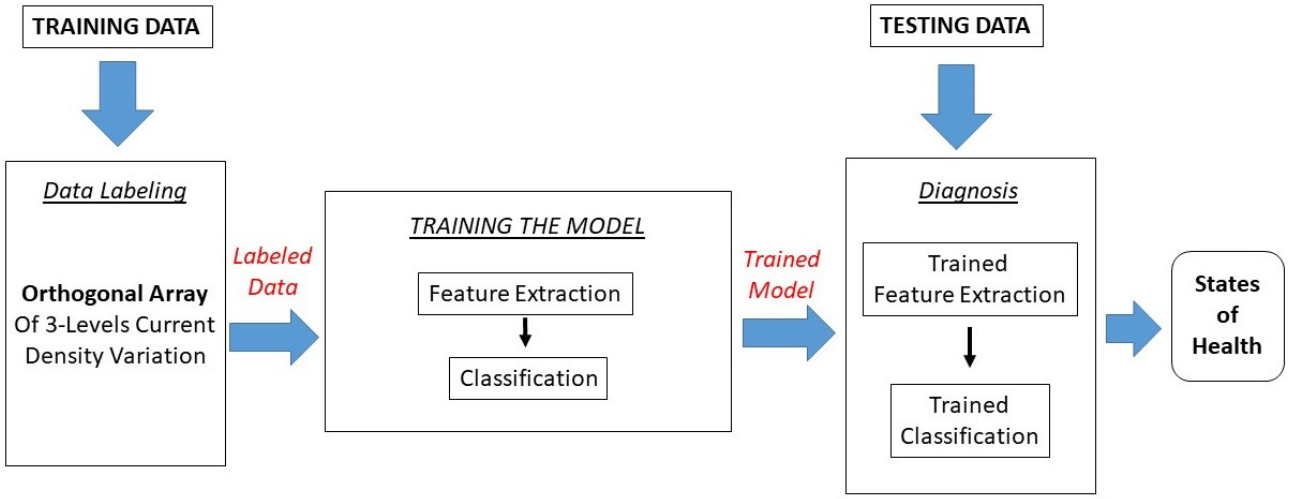

Figure 3.2: Diagnosis process

3.1.1 *Data labeling*

This classification methodology considers the normal operation and several examples of faulty operations. The different faulty classes are identified based on the size and the shape of each fault. Considering the 2D fuel cell emulator, the size is explained by the number of affected bars while the position is identified by the position of each faulty bar in the emulator. Fig(3.3) explains the normal operation and the different faulty operations that were considered in our study. In addition, Tab(3.1) illustrates the percentage of the affected area of the active surface.

Table 3.1: Fault area with respect to the emulator active surface

Fault	**Percentage *(%)***
F2B	12.5
F3B	18.75
F4B	25

In the normal operation, the current density is considered constant in the whole FC active surface, faulty operation is modeled by a heterogeneous current distribution. In this chapter, the 2D emulator presented in section 2.1 is used to study the influence of the current heterogeneity on the measured external magnetic field.

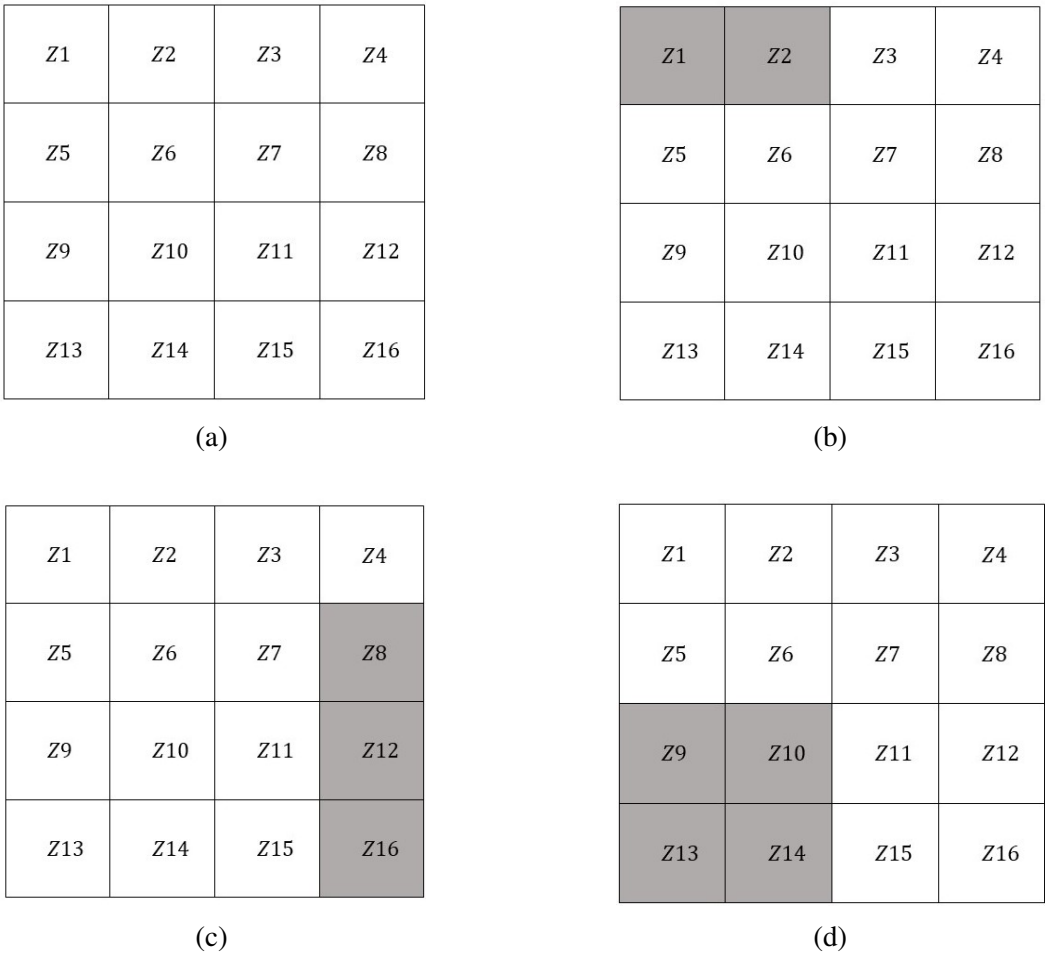

Figure 3.3: Different emulator stack operations, (a) Normal, (b) F2B, (c) F3B, and (d) F4B

3.1.1.1 Normal Behavior

The current density in the active area of the FC is assumed to be **gussy** homogeneous in the case of healthy operation due to the slight fluctuations in current flow that can occur at the electrolyte membrane level, inside the cells of the stack [49]. This homogeneous current distribution in the 2D emulator is reproduced by a given value I_N in each bar of the emulator. This current is explained by

3 level variations as following:

$$I_N = \begin{cases} I_N^+ = I_N + \Delta_I, \\ I_N = I_T/n_s \\ I_N^- = I_N - \Delta_I \end{cases}$$

Where $I_T = 70$ A, n_s the number of sensors, and Δ_I is the level of variation of current flow equivalent to 10% of I_N.

3.1.1.2 Faulty Behavior

Due to the conservative overall current phenomenon, the current drop in the faulty region will increase the current in the rest of the conductive part of the fuel cell. Then, the current drop I_F explains the fault current within the affected bar as following:

$$I_F = \begin{cases} I_F^+ = 2\Delta_I \\ I_F = \Delta_I \\ I_F^- = 0 \end{cases}$$

Furthermore, I_{NR} in Eq(3.1) presents for every sample, the current within each bar in the remaining unaffected region.

$$I_{NR} = \frac{\sum_{i=1}^{n_s} I_i}{b_N} \tag{3.1}$$

Where b_N is the number of unaffected bars and I_i could be I_N and I_F in there 3 levels of variation.

3.2 Statistical analysis used for diagnostic of PEMFC

Statistical methodologies for diagnosis are considered as one of the most relevant. Using these analysis, data based diagnostic requires a large labeled data base, to adopt and elaborate the diagnostic algorithms. For example, in [54] an inverse model of PEMFC stack and single cell voltages measurements is used to label the different flooding conditions inside the data base. Moreover, in [1] the diagnosis process is based on a real-time cell voltage which are sampled and represented in vectors. This data set is labeled into three different classes (Normal, flooding, and drying) by combining the pressure drop model with the statistical analysis.
In this approach, the labels of each experiment are associated with the considered FC states: the faults explained in Tab(3.1) and the normal emulator states. For each considered FC state, labeled experiments are generated by dropping the current flow inside the affected bars using a set of current sources at each emulator bar, see Fig(3.4).

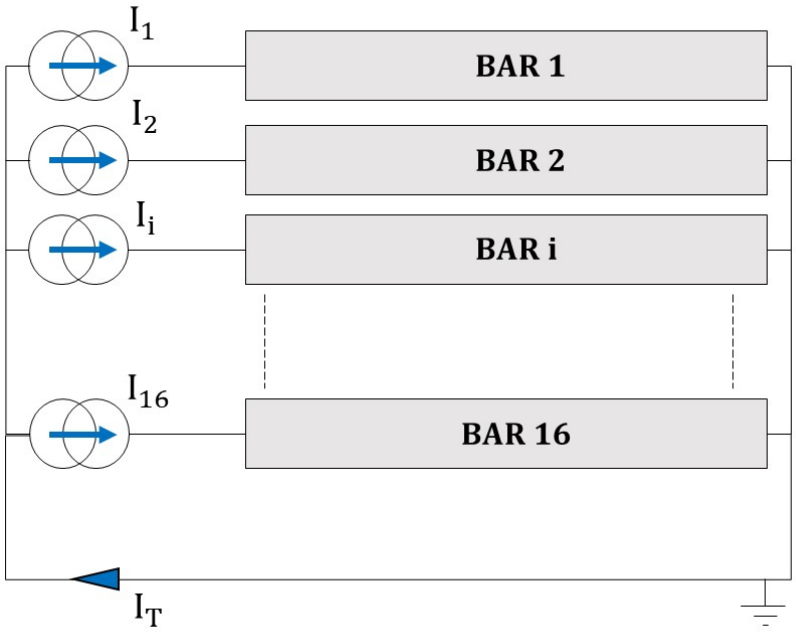

Figure 3.4: Current sources supply for each emulator bar

Moreover, Fig(3.5) demonstrate the current distribution in each bar of the emulator at one of the OA experiments in different model operation conditions.

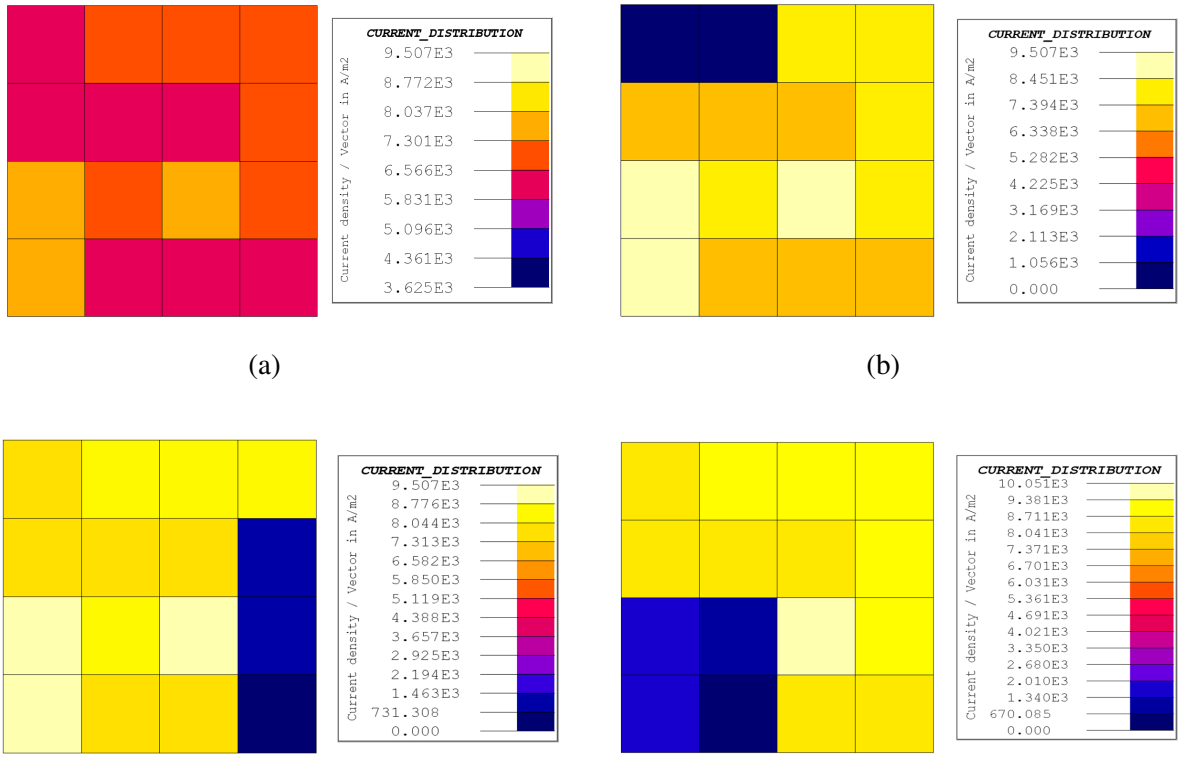

Figure 3.5: Current distribution inside the emulator in, (a) Normal, (b) F2B, (c) F3B, and (d) F4B

3.3 Importance of using experimental design in statistical analysis

Many research topic which carried out in the academic environment [55] are based on the orthogonal experimental designs introduced by Fisher in 1920s [56]. In 1986 Taguchi [57] went further by inventing a new concept of experimental designs based on two optimization problems categories called $Signal - to - Noise$ ratios. The overall design objective is to collect of the important data to identify which factors most affect the data set quality with minimum amount of experiments instead of testing all the possible combinations.
In this study, the current variation ($3\ levels$) supplied by the current sources to the emulator in the normal and faulty bars will produce a massive database of current flow variations between the bars (3^Q), where $Q = 16$ is the bars number inside the proposed emulator. Therefore, Taguchi design in the experimental orthogonal array was used to reduce number of experiments in the produced database.

3.4 Training Data Based on Experimental Design

The pattern classification method used belong to supervised ones. In these methods, the training experiments should be labeled before the training procedure. Each experiment is labeled based on the initial current distribution J which identify each state, see Fig(3.1). In the labeling stage, the training dataset is labeled and identified into four classes, the normal behavior and the three considered faults expressed in Tab(3.1).

3.4.1 *Normal Operation*

Regardless of the level of current variation between the bars, the SUM (S) of each sample in the orthogonal matrix should be equal to $I_T = 70\ A$.To obtain the equivalence between I_T and S, the coefficient (C) in Eq.(3.2) is multiplied by each experiment of the OA.

$$C_i = \frac{I_T}{S_i} \quad where \quad 1 \leq i \leq 81 \tag{3.2}$$

3.4.2 *Faulty Operation*

After applying the levels of the drop current I_F inside the default bars Fig(3.3), the total sum of each experiment will be dropped ($S_F < S_N$), where S_N and S_F are the sum produced by each each experiment in both, normal and faulty operation conditions. Tab(3.2) shows the orthogonal array (OA) levels used relative to the normal and faulty levels of the current variation.

Table 3.2: Orthogonal Array (OA) levels used relative to the normal and faulty levels of the current variation

OA	I_N	I_F
A	I_N^-	I_F^-
B	I_N	I_F
C	I_N^+	I_F^+

As for a similar FC current, the value of I_T is conservative, then the current drop in the affected region will cause an increase of the current value in the remaining part to increase. In order to adapt S_F in each sample to become equal to I_T, Five steps were considered as following:

① The sum of each experiment in normal behavior is subtracted from the sum of each experiment in the faulty behavior Eq.(3.3).

$$k_i = S_N - S_F \tag{3.3}$$

② k_i is divided by the remaining normal bars (b_n), see Eq.(3.4).

$$U_i = \frac{k_i}{b_n} \tag{3.4}$$

③ U_i is added to the current value of b_n Eq.(3.5).

$$I_{b_n}(New) = I_{b_n} + U_i \tag{3.5}$$

④ In this step the new sum S_F of each sample is equivalent to S_N.

⑤ Then C_i in Eq.(3.2) is computed and multiplied by each sample.

3.4.3 *Orthogonal Array*

The approach is based on an orthogonal array model presented in [58]. This design variables of 81 experiments (Exp) is based on the variation of the current flow between the bars of the emulator from $Z1$ to $Z16$. Thereby, the considered orthogonal design is presented in Tab(3.3).

Table 3.3: The used Orthogonal Array

Exp	Z1	Z2	Z3	Z4	Z5	Z6	Z7	Z8	Z9	Z10	Z11	Z12	Z13	Z14	Z15	Z16
1	A	A	A	A	A	A	A	A	A	A	A	A	A	A	A	A
2	A	A	A	A	A	A	A	A	A	A	A	A	A	B	B	B
3	A	A	A	A	A	A	A	A	A	A	A	A	A	C	C	C
4	A	A	A	A	B	B	B	B	B	B	B	B	B	A	A	A
5	A	A	A	A	B	B	B	B	B	B	B	B	B	B	B	B
6	A	A	A	A	B	B	B	B	B	B	B	B	B	C	C	C
7	A	A	A	A	C	C	C	C	C	C	C	C	C	A	A	A
8	A	A	A	A	C	C	C	C	C	C	C	C	C	B	B	B
9	A	A	A	A	C	C	C	C	C	C	C	C	C	C	C	C
10	A	B	B	B	A	A	A	B	C	B	C	B	C	A	A	A
.	.	.	.	.	.	.	.	.	.	.	.	.	.	.	.	.
.	.	.	.	.	.	.	.	.	.	.	.	.	.	.	.	.
.	.	.	.	.	.	.	.	.	.	.	.	.	.	.	.	.
80	C	C	B	A	C	B	A	B	A	A	B	C	C	B	A	C
81	C	C	B	A	C	B	A	B	A	A	B	C	C	C	B	A

3.5 Diagnosis Strategy

The results of section 2.1.5.1 and 2.1.5.2 depicts the accuracy of the proposed method for diagnosing the position of the fault inside 2D emulator. After labeling the dataset, the training and testing datasets is expressed by a 3-level of current variation, which is imposed as shown in Fig(3.6). As a

consequence of imposing the training and testing data for normal and faulty emulator operation conditions, the new dataset at the output level, where denoted by Δ_B at the magnetic sensors level. The new dataset is used to train and test feature extraction and classification machine learning algorithm used in this chapter.

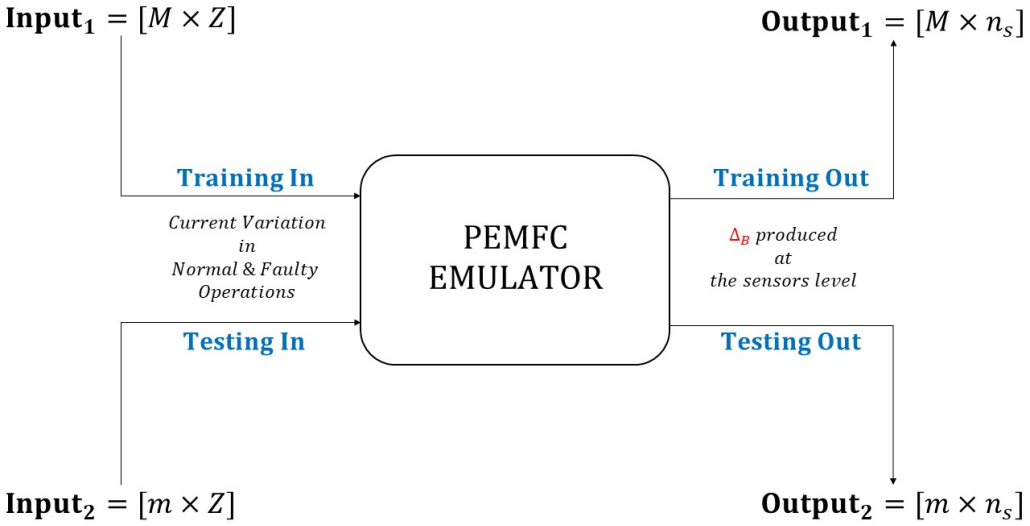

Figure 3.6: Input current variation and the output Δ_B at the sensors level datasets, were M= 81 and m= 24

3.5.1 *Feature Extraction*

Feature discriminant analysis is responsible for data dimensional reduction from n_s dimensions to a lower number dimensions u. Feature discriminant analysis in the training model can be explained as following:

The H (M*(k)) training samples $s_1, s_2, \ldots, s_H \in R^{n_s}$, these samples are distributed in C classes $c_1, c_2, \ldots, c_C$. Sample s_n is a vector constructed by n_s of the differences between the external magnetic field Δ_B in both emulator operations.

$$s_n = [s_n 1, s_n 1, ..., s_n n_s]^T$$

Dimensional reduction process is based on the unit projection vector $[p_1, p_2, \ldots, p_u]$. The projection vector of the s sample is as following:

$$w = [{p_1}^T s, {p_2}^T s, \ldots, {p_u}^T s]^T$$

3.5.1.1 Principle Component Analysis (PCA)

PCA is an unsupervised dimensional reduction and feature extraction technique [1]. This method identifies the eigenvectors and eigenvalues of the data set covariance matrix after decreasing the variance of the initial variables in order to compute the Principal Components (PCs) which are responsible for data lower dimension space projection.

Algorithm 1 *PCA*

Performing

1. Calculate the mean of every dimension of the whole dataset.

$$Dataset = [\frac{\sum_{n=1}^{H} s_n 1}{H}, \frac{\sum_{n=1}^{H} s_n 2}{H}, ..., \frac{\sum_{n=1}^{H} s_n n_s}{H}]^T$$

2. Compute the square dimensional covariance matrix of the whole data set.

$$\frac{1}{H}\sum_{n=1}^{H}(s_n - \overline{s})(s_n - \overline{s})^T$$

   where $\overline{s}$ is the mean for each variable n_s in the dataset.

3. Calculate the eigenvectors v and corresponding eigen values λ.

$$det(Dataset - \lambda I) = 0$$

   where I is the indentity matrix.

4. Arrange λ in descending order and take the f highest values for PCs.
5. Project the samples on the new subspace using the projection vector w

3.5.1.2 Linear Discriminant Analysis (LDA)

Linear Discriminant Analysis is a supervised linear algorithm that computes the direction of the axis which maximize the separation between multiple classes and make the data within the same class concentrated [59]. Furthermore, the Eigenvectors computation is computed between and within the classes of the labeled dataset.

Algorithm 2 *LDA*

Performing

1. Calculate the mean of each class μ_i.
2. Calculate the total mean of the whole dataset μ.
3. Calculate between-class matrix S_B

$$S_B = \sum_{i=1}^{C} H_i(\mu_i - \mu)(\mu_i - \mu)^T$$

4. Calculate within-class matrix S_W

$$S_W = \sum_{i=1}^{C}\sum_{n\in u_i} H_i(\mu_n - \mu_i)(\mu_n - \mu_i)^T$$

5. Calculate the eigenvalues of the eigenvector.
6. Sort the Eigenvectors in descending order based on their Eigenvalues.
7. Use the first u Eigenvectors for lower dimension space

3.5.1.3 Kernel Principle Component Analysis (KPCA)

Kernel principal component analysis is a continuation of PCA, which is mostly used for the non-linear correlated data sets. In fact, there are two main steps that can be performed in this dimensionality reduction process, the first is to map the dataset into a higher dimensional space in which they vary linearly via a nonlinear mapping [60], the second step is to apply the PCA procedure on the new space.

3.5.2 *Classification*

This process comes after the feature extraction of the original data set. The new variables projected to the new subspace and each group of samples belong to a specific class index. The classification method can be explained as follow: H samples $l_1, l_2, \ldots, l_H \in R^{n_s}$ distributed on C classes $z_1, z_2, \ldots, z_C$, the class index of z_n are distributed in C classes.

3.5.2.1 Support Vector Machine (SVM)

Support Vector Machine (SVM) is a learning algorithm developed by V.Vapnik [61] for a supervised data set used for classification and regression problems. This classifier can be applied on a linear and non-linear data set. In the linear space, the original data set is mapped to a higher dimensional space in order to find a one-dimension hyperplane that has the maximum margin from the data to separate the linear variables . In addition of finding the hyper plane, SVM creates two parallel lines on both sides of the hyperplane points, that passes through the nearest support vectors called "$large\ margin\ classification$". On another hand, in non-linear data set SVM uses some tricks like increasing the data features subspace or use some kernels like, (Polynomial, Gaussian RBF) so that the non-linear data distribution will be linearly separable. The algorithm of SVM is applied in [1].

3.5.2.2 k Nearest Neighbors (kNN)

The k nearest neighbors is a type of supervised machine learning algorithm which considered one of the oldest classification methods used for pattern classification. This method is defined as a lazy learning algorithm since it does not have a training phase and uses all the data in classification. Moreover, it is a non parametric learning algorithm because it does not assume anything about the underlying data. The k-nearest neighbors classify the new unlabeled sample with the majority of labeled samples in the training dataset based on the k-nearest neighbors. The k-nearest neighbors use a simple Euclidean metric [62] to measure the distance between the new sample and the set of training samples between classes in the dataset.

Algorithm 3 *kNN*

Performing

1. Collect the labeled samples $l_1, l_2, \ldots, l_H$.
2. For the new sample l, calculate its Euclidean distance from $l_1, l_2, \ldots, l_H$.
3. Find the k nearest neighbors of l which gives the minimum Euclidean distance.
4. Assign the l to C class to which most of the neighbors belong.

3.5.2.3 Decision Tree

The decision tree is a classification model that uses a tree structure to classify data [63]. This classifier consists of three main nodes: decision nodes are nodes that have two or more branches, leaf nodes represent the decision, and root nodes are also decision nodes but at the highest level, see Fig(3.7).

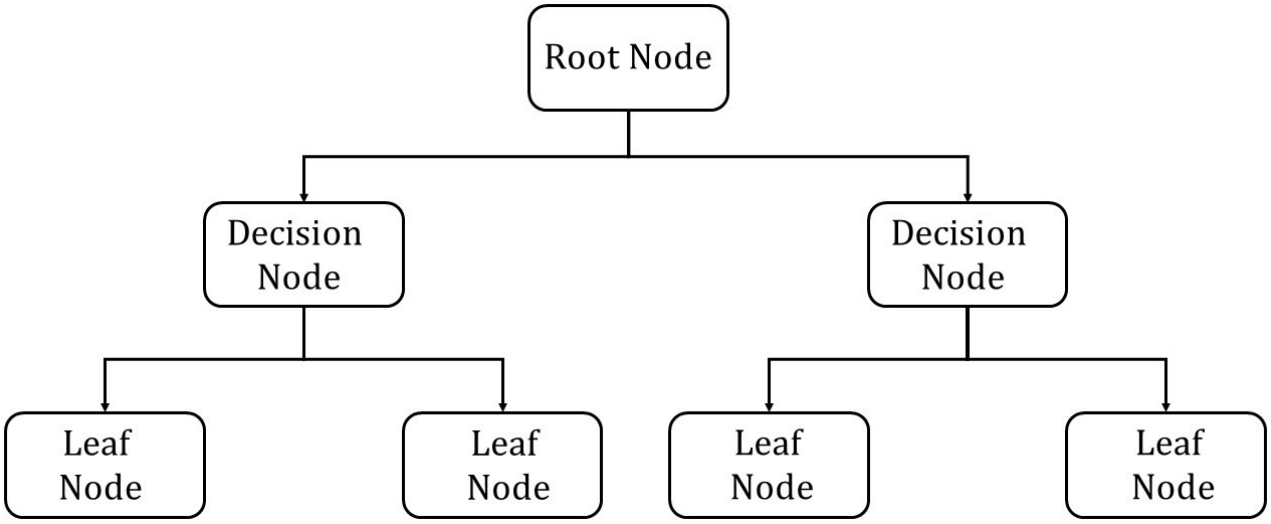

Figure 3.7: Diagnosis process

The distribution of data among the nodes is based on a kind of 'Divide and Conquer' algorithm. Each path from the root of a decision tree to one of its leaves can be transformed into a rule simply by conjoining the tests along the path to form the antecedent part, and taking the leaf's class prediction as the class value. Then if the subsets are pure, meaning that all samples are true or false, we stop to get the leaf node, if the subsets are not pure, then the node is a divider node and must be continued. In the split node, the algorithm considers other attributes of the data set to split the data, the classifier continues until all nodes in the tree become leaf nodes.

3.6 Datasets used for training and testing the diagnostic

By considering the experimental emulator and the FES model, the 3-level OA is imposed to the 16 current sources to supply the emulator. For each experiment, the vector containing the values of the magnetic field analyzer will be labeled with the considered state of health of the FC, and added to the experimental training dataset. Moreover, a training dataset based on the numerical FES model is obtained by computing the magnetic field. In addition, testing data is similarly explained using random experiments to the current sources, see Fig(3.8). Therefore, due to the small variation between simulation and experimental results, the machine learning data analysis methods were trained and tested based on different training and test datasets as follows:

- Experimental training and Experimental testing datasets
- Numerical training and Experimental testing datasets

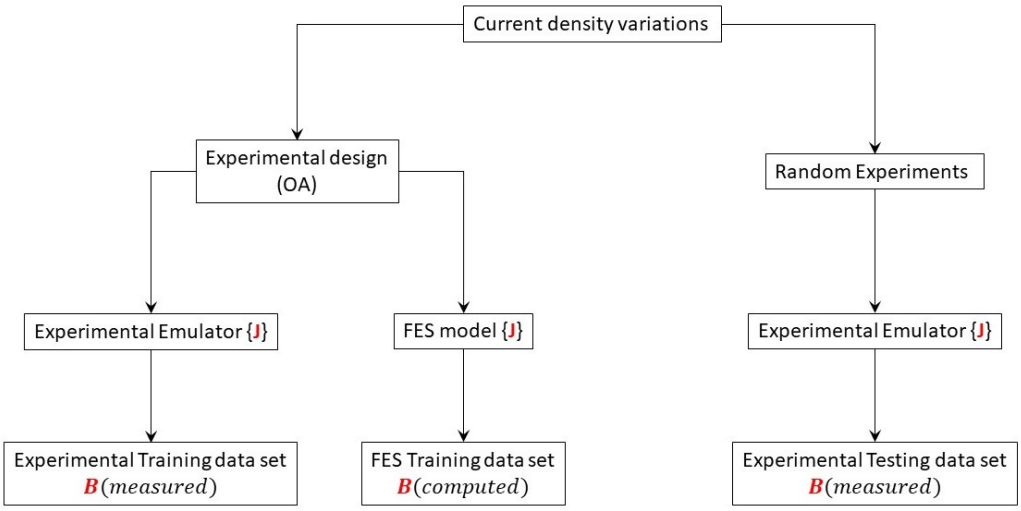

Figure 3.8: Experimental emulator and FES model training and testing datasets.

3.6.1 *Experimental emulator training dataset*

To obtain a current distribution of the FC active surface, the 2D PEMFC model expressed in chapter 2 has been used. Each rod is connected at both end to a DC current supply so that each rod act as a load. By controlling each sub-volume individually, we can easily control the current distributions across the section and therefore replicate a wide variety of default, see Fig(3.9).

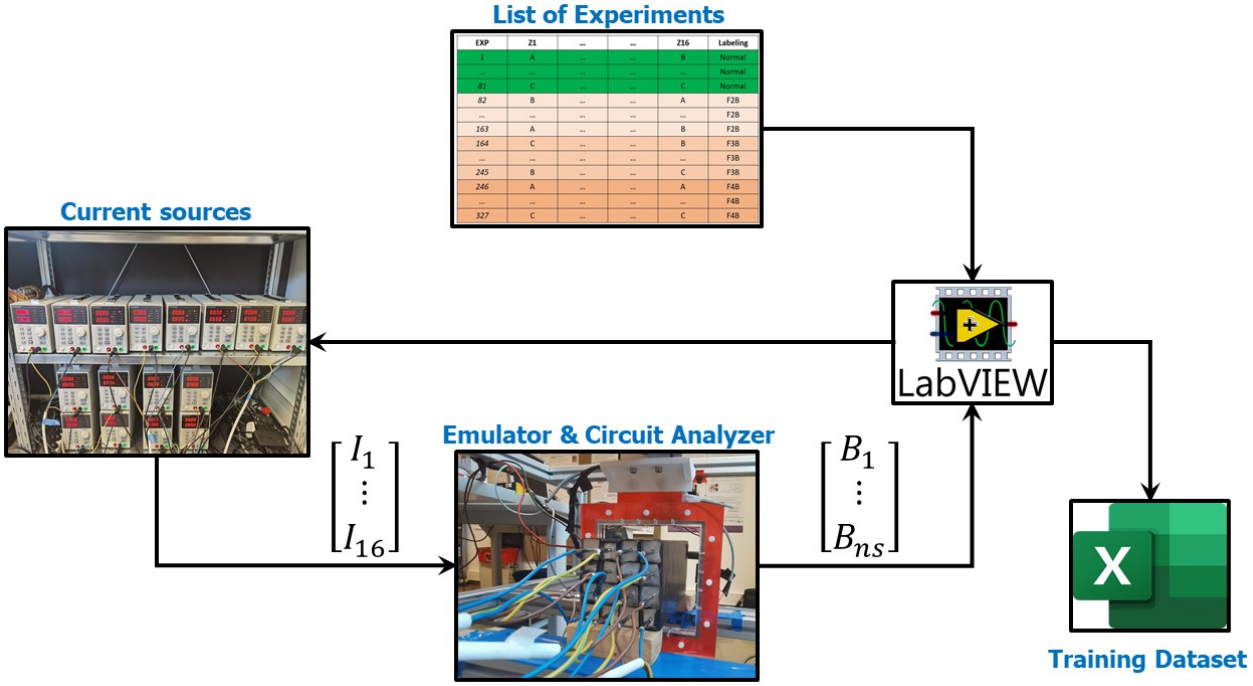

Figure 3.9: Steps used to obtain the experimental training and testing datasets.

The magnetic field generated by the current inside the emulator is then measured by a surrounding $160 \times 160\ mm$ ferromagnetic magnetic analyzer.The 16 sensors have linear behavior with a high sensitivity of $25mV/G$ and an output voltage of $4V$ at zero magnetic flux density. The output voltages are connected to a NI-9205 data acquisition system bound to a LabVIEW program. This setup allows

us to get a set of 16 magnetic field $B = [B1; B2; \ldots; B16]$ from a set of current $I = [I1; I2; \ldots; I16]$. Control of the values of DC current sources is achieved by the Lab VIEW program by first extracting the set of 16 current set points from the OA and then sending the references to the sources. The sources are connected to the PC through USB hub and interface USB/RS232. To each set I corresponds a set B, collected in a result matrix. Magnetic field measurements are performed in normal as well as various fault behaviors. Fault behaviors are characterized by 2, 3 and 4 non-conducting rods located in different regions of the active surface and named **F2B** bars, **F3B** bars and **F4B** bars respectively, see Fig(3.3) and Tab(3.1). To assess the change in the current density, we should study the set of $\Delta_B = B_{normal} \breve{} B_{Fault}$. A positive Δ_B means the current density in normal mode is higher than in fault mode and thus that nearby surface is not conducting. In Fig(3.10a), Fig(3.10b), Fig(3.10c) and Fig(3.10d) the generated Δ_B of the training experimental dataset have been presented. In the normal behavior, the Δ_B produced is obtained by subtracting the magnetic field produced in the perfect normal, when there is no current variation between the bars, from the magnetic field obtained in the 3-level current variation.

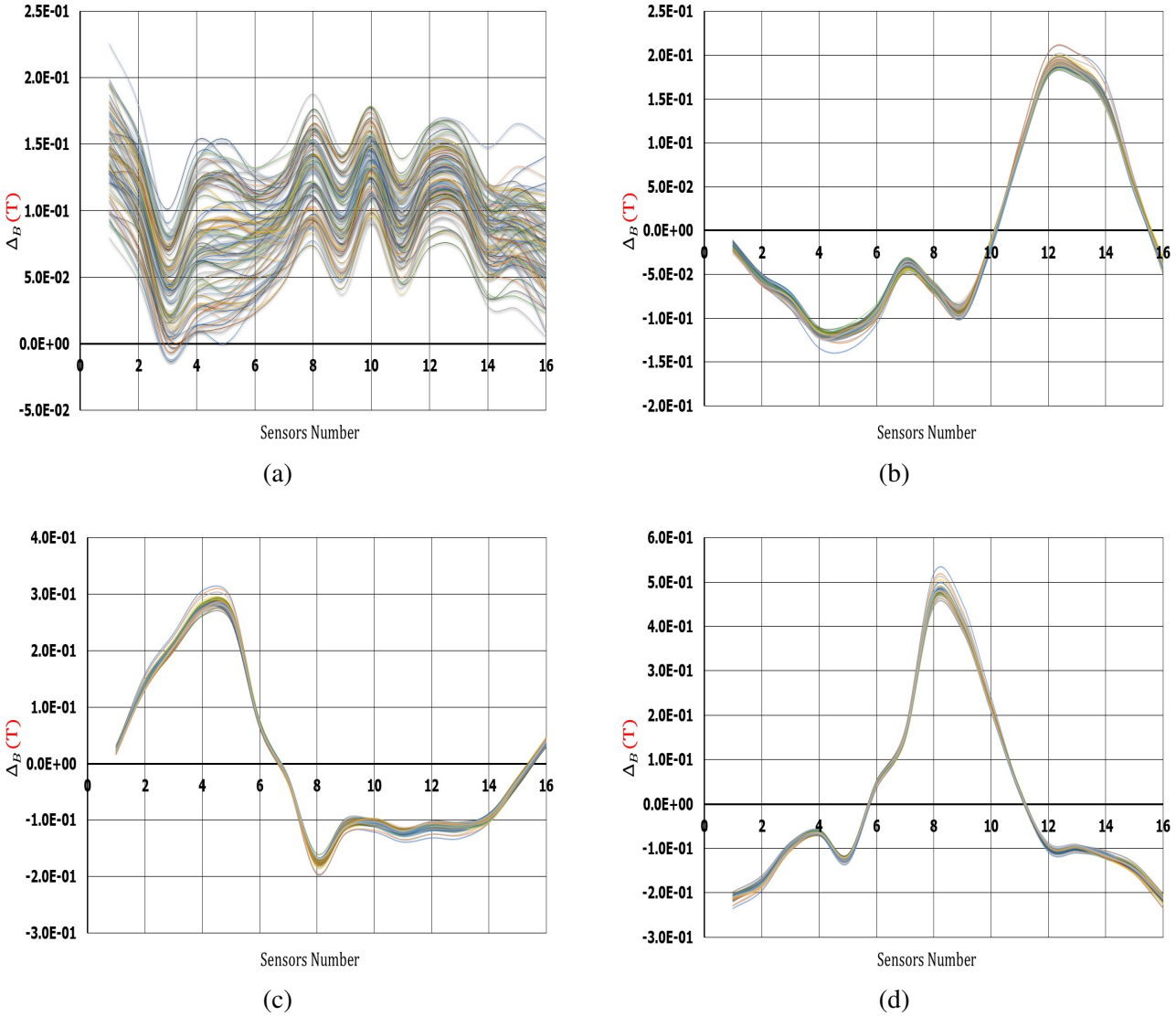

Figure 3.10: Δ_B variation of experimental emulator training data set, (a) Normal, (b) F2B ,(c) F3B and (d) F4B

3.6.2 *Finite Element Simulation (FES) model Training data set*

This model is based on the magnetostatic problems of [49] solved using Altair flux software [64]. The generated training datasets were estimated based on $n_s = 16$ sensor positions within the air gaps of the ferromagnetic analyzer, see Fig(2.21d). To obtain the Δ_B dataset used for training, the magnetic field of the normal behavior matrix was subtracted from the perfect normal without variation, Fig(3.11a) shows the numerical testing Δ_B dataset. On the other hand, the faulty Δ_B is calculated by subtracting the faulty magnetic field matrix from the normal value to create a variable Δ_B, see Fig(3.11b), Fig(3.11c) and Fig(3.11d) . Therefore, the final dataset for training is based on the the fabricated Δ_B matrix for the normal positions and the different defective positions for the emulator operating conditions.

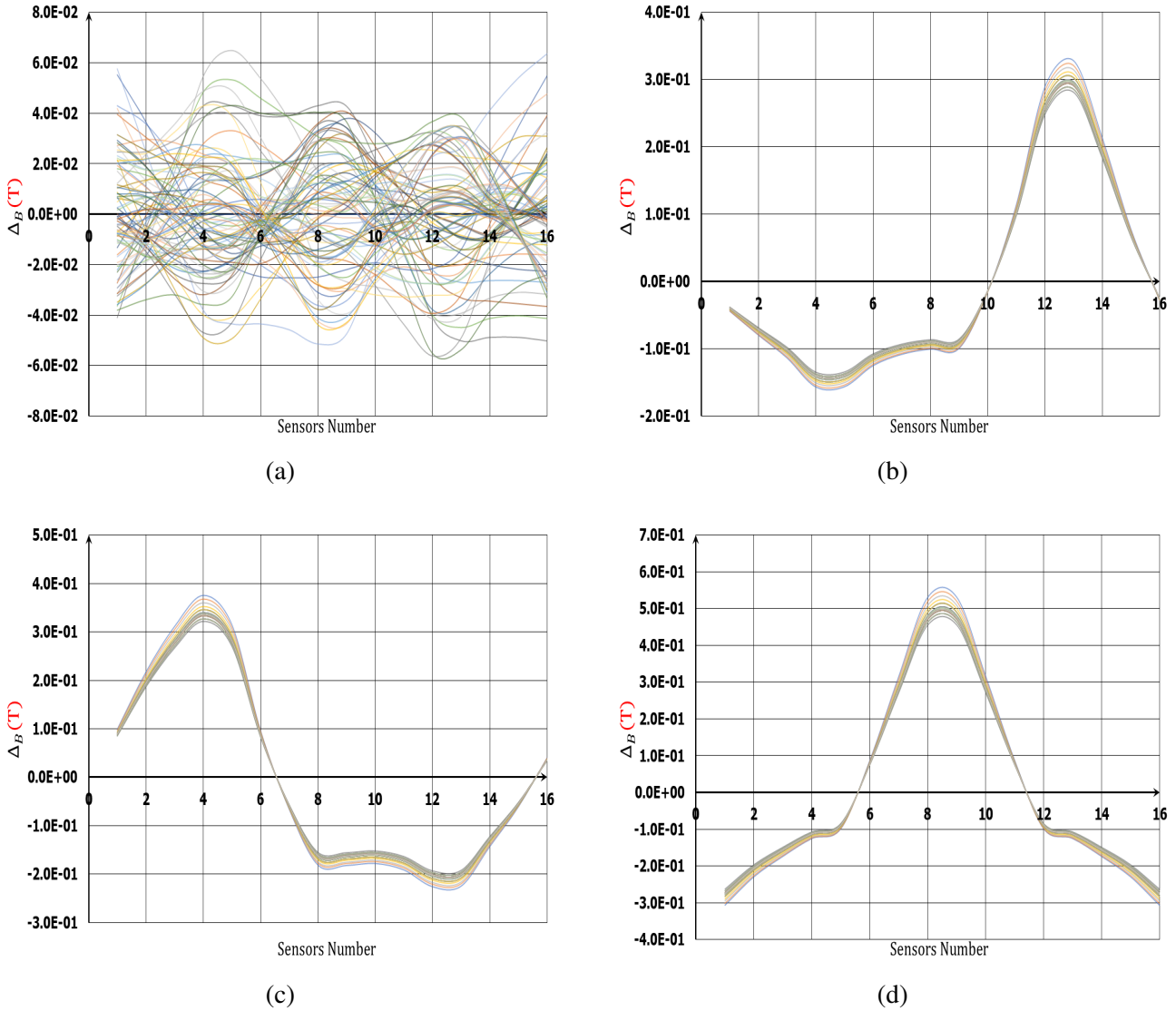

Figure 3.11: Δ_B variation of FES model training data set , (a) Normal, (b) F2B ,(c) F3B and (d) F4B

3.7 Testing Data Based on 3-levels Q Variation Table

This data was created from a 3-level $Q = 16$ variation table which contains 3^Q experiments, see Tab(3.4). A random number of $m = 24$ experiments was chosen from Tab(3.4). In a normal operation, m was randomly chosen from the experiments which have S_N in each experiment is equal to $I_T =$

$70A$. Moreover, in the faulty condition, the 24 experiments were randomly selected, and then the steps in the previous section were applied to obtain $I_T = 70A$ for each experiment in the faulty condition.

Table 3.4: 3-levels variation for a 16 variables

Exp	Z1	.	.	.	.	.	.	.	.	Z16	SUM
1	A	.	.	.	.	.	.	.	.	A	I_1
2	A	.	.	.	.	.	.	.	.	B	I_2
.	A	.	.	.	.	.	.	.	.	C	.
.	A	.	.	.	.	.	.	.	.	A	.
3^{15}	A	.	.	.	.	.	.	.	.	B	.
$3^{15}+1$	B	.	.	.	.	.	.	.	.	C	.
.	B	.	.	.	.	.	.	.	.	A	.
.	B	.	.	.	.	.	.	.	.	B	.
.	B	.	.	.	.	.	.	.	.	C	.
2×3^{15}	B	.	.	.	.	.	.	.	.	A	.
$2 \times 3^{15}+1$	C	.	.	.	.	.	.	.	.	B	.
.	C	.	.	.	.	.	.	.	.	C	.
.	C	.	.	.	.	.	.	.	.	A	.
.	C	.	.	.	.	.	.	.	.	B	.
3^{16}	C	.	.	.	.	.	.	.	.	C	$I_{3^{16}}$

3.8 Results and Discussion

3.8.1 *Results*

The experimental training dataset is used to train the data-driven diagnosis methodology. As explained in section 3.5, the diagnostic strategy involves two steps: feature extraction and classification. For the first time, the experimental data set has been used to train the feature extraction and classification. All the feature extraction methods presented in section 3.6 (PCA, KPCA, LDA) and the classification methods (SVM, kNN, DT) were trained using the simulation dataset. Thereby, this procedure was validated using an experimental dataset and the results are shown in Fig(3.12).
We observe that the data points using LDA in Fig(3.12g,3.12h,3.12i) disperse over the whole scale, whereas the overlap regions between the data normal and other three fault states are large. In contrast, as for the results of PCA and KPCA (see respectively Fig(3.12a,3.12b,3.12c,3.12d,3.12e,3.12f)), the points in the same class are more concentrated, and the amount of overlapping point are zero, which means points in different classes are decentralized. Classification methods, SVM, kNN, and DT were carried out in the different feature spaces. For instance, Fig(3.12) shows the visualization results of SVM, kNN, and DT classifications in PCA, KPCA, and LDA feature spaces respectively. It can be seen clearly in PCA and KPCA that the feature space is divided into four zones, which denote different states, and the boundaries determined by different classifiers are different. On another hand, these classifiers boundaries are difficult to determine the different states obtained in LDA feature domain due to the overlapped regions between he different states.
In addition, the experimental data set has been used to train the feature extraction and classification. All the feature extraction and classification methods are trained. Again, the procedure is then validated using the experimental dataset and the results are shown in Fig(3.13). The visualized results once again shows the ability of PCA and KPCA in concentrating the points within the same class inside feature space. This will facilitates to determine the boundaries by the different classifiers used.

On another hand, using the numerical dataset as a training set improves the accuracy of the different classifiers due to the better points distribution of the four different classes in LDA feature space.

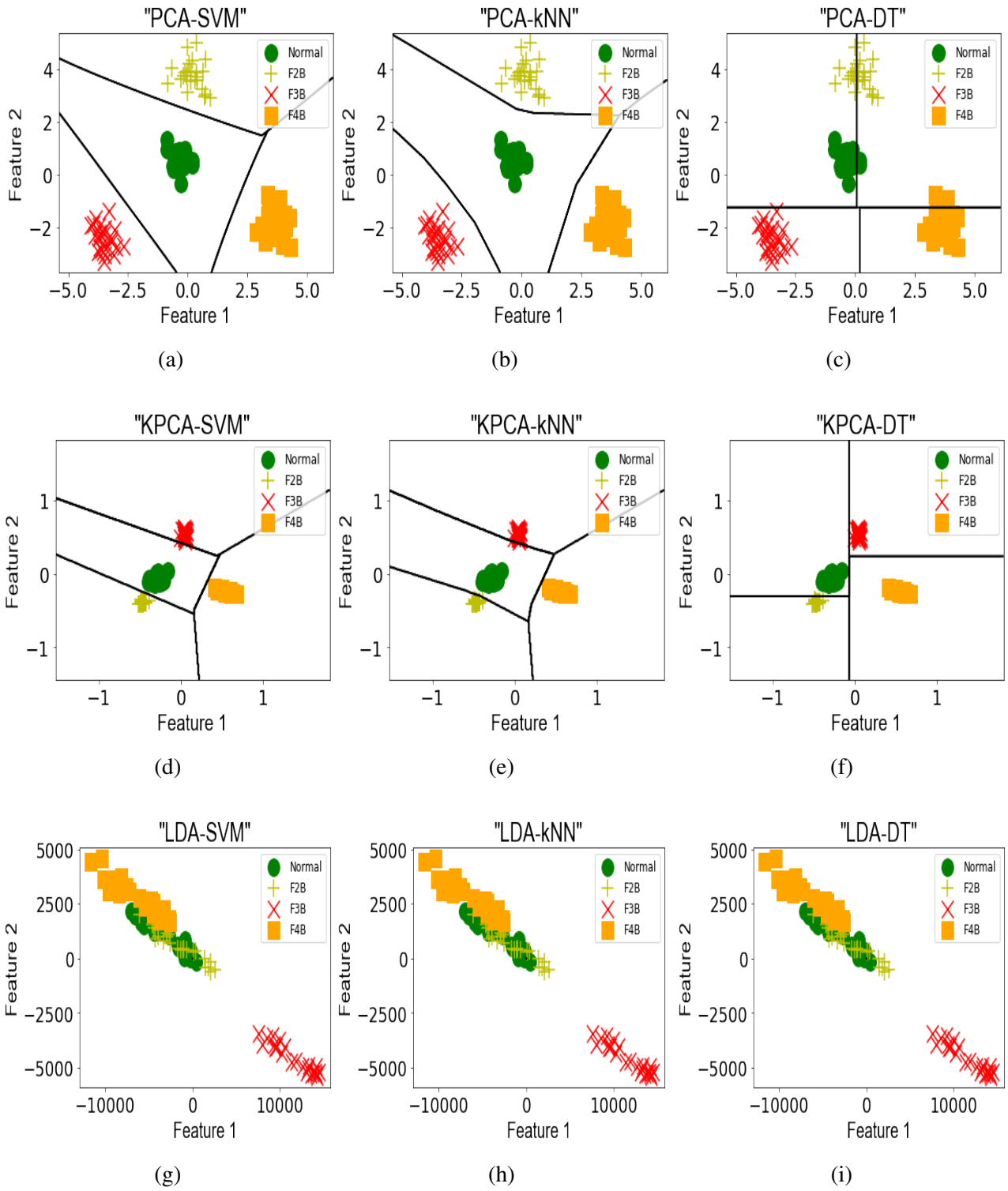

Figure 3.12: Simulation training and experimental testing datasets applied on (a) PCA-SVM, (b) PCA-KNN, (c) PCA-DT, (d) KPCA-SVM, (e) KPCA-KNN, (f) KPCA-DT, (g) LDA-SVM, (h) LDA-KNN, (i) LDA-DT

.

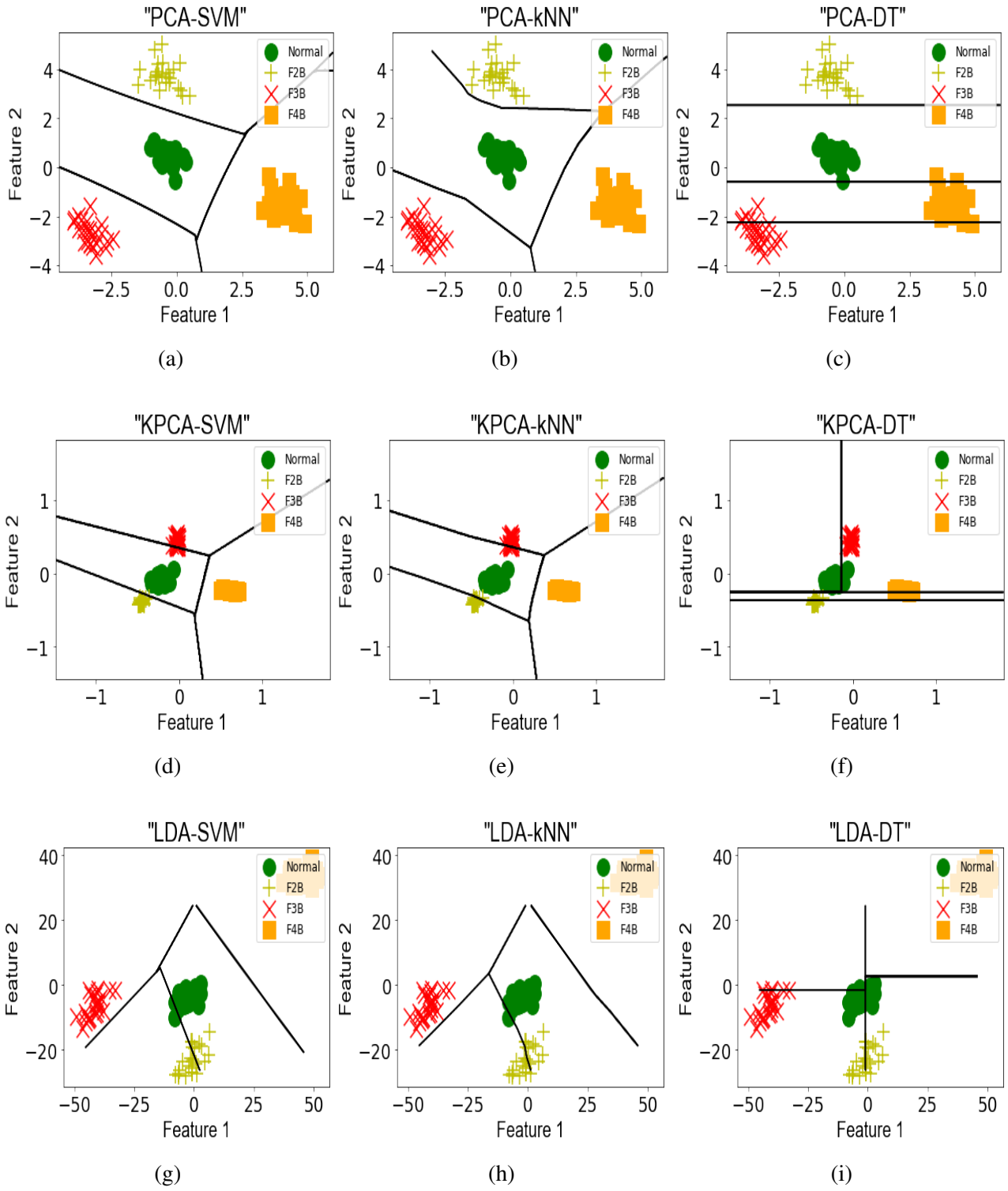

Figure 3.13: Experimental training and experimental testing datasets applied on (a) PCA-SVM, (b) PCA-KNN, (c) PCA-DT, (d) KPCA-SVM, (e) KPCA-KNN, (f) KPCA-DT, (g) LDA-SVM, (h) LDA-KNN, (i) LDA-DT

.

3.8.2 *Discussion*

This section is based on a set of testing data applied to the trained data analysis methods to identify the diagnosis accuracy detected by the algorithm.
Based on Tab.(3.5) using numerical training and experimental testing data sets gives a better coupling for data analysis prediction methods due to high accuracy prediction between most of the feature extraction and classification.

Table 3.5: Training and testing datasets

DATA ANALYSIS METHODS			TRAINING					
			NUMERICAL			EXPERIMENTAL		
			SVM	KNN	DT	SVM	KNN	DT
Testing	EXPERIMENTAL	PCA	100%	100%	90%	100%	100%	97%
		KPCA	95%	100%	92%	100%	100%	73%
		LDA	0%	0%	0%	89%	90%	66%

Furthermore, the choice of the best algorithmic data analysis method is based on the computational time versus the accuracy obtained. The processor used for this computation is *Intel(R)Core(TM) i9-10900K CPU @ 3.70GHz(20 CPUs), ∼3.7GHz*, Tab(3.6) . Therefore, using KPCA with SVM in the simulated training and experimental testing datasets will produce the best diagnostic analysis for the 2D PEMFC model behavior.

Table 3.6: Time computation needed by each data analysis method

Time in ***ms***			TRAINING					
			NUMERICAL			EXPERIMENTAL		
			SVM	KNN	DT	SVM	KNN	DT
Testing	EXPERIMENTAL	PCA	830	14794	435	809	16320	449
		KPCA	405	1985	351	402	2032	360
		LDA	28900	718478	5378	19266	637999	4875

3.9 Conclusion

In order to obtain a higher statistical relevance, with a reduced number of experiments, in this chapter a Taguchi experimental design is presented to generate a 3-levels of variations around the initial current distribution J. Using the variation in current density in each bar of the FC emulator, the dataset is labeled into normal and faulty behaviors that can occur at different locations in the active FC area. This dataset is used as an input for experimental emulator and FES model to obtain a new dataset of external magnetic field dependency. Then a strategy based on pattern recognition tools for the diagnosis of 2D conduction faults in PEM fuel cells is used. This approach is achieved by classifying the features extracted from the vectors constructed OA training dataset. Representative feature extraction methods: PCA, KPCA, DT and classification methods: SVM, kNN, and LDA are then validated using a random experimental dataset. The obtained results depicts a significant accuracy for data analysis methods by using both, experimental and numerical training datasets. Moreover, the test results show that the use of KPCA and SVM in numerical training dataset performs better with shorter time. Therefore, from the obtained results two assumptions can be drawn. First, the fabricated external Δ_B from the current distribution variation can be considered as one of the fuel cell original variables which can identify the fault position. Second, using OA in numerical models can be used as a training dataset for the data-driven diagnosis methodology.

CHAPTER 4

EFFECT OF THE FERROMAGNETIC CIRCUIT ANALYZER GEOMETRY ON THE EXTERNAL MAGNETIC FIELD

In this chapter, a new circuit analyzer design is presented to investigate the impact of the magnetic sensor distribution on the external magnetic field measurements. As a result of the numerical findings in Sections 2.1.5.1 and 2.5.2.1, these consequences were repeated using the new analyzer format. In addition, various geometric parameters of the new and square model, such as air gap width, analyzer dimensions, and number of sensors, are optimized with respect to the external magnetic field generated by the 2D emulator model. This model was selected for the optimization process due to its simple homogeneous and heterogeneous current flow generating a non-complex external magnetic field around the model which can be easily detected by the analyzers. Therefore, based on the obtained results and experimental limitations, the conclusion reached clarifies the importance of using the square design in our passivated stack model. It also suggests a new 3D fault detection technique to be numerically applied and experimentally validated on the test bench.

4.1 New design

This geometry is considered as new design with respect to sensor distribution and analyzer format. The sensors are evenly distributed in the air gaps of $2\ mm$ over the circular format of the ferromagnetic analyzer of radius $R = 80\ mm$ and $L = 30\ mm$, see Fig(4.1). The advantage of this new design is that the ferromagnetic material parts of the circuit analyzer are equally positioned at a distance L between the sensors. These changes will clearly affect the external magnetic field measured in Sections 4.2.1 and 4.2.2 when the new design is applied to the 2D and 3D aluminum bar emulators. The variation in magnetic amplitude between sensors will be smaller due to the homogeneous distribution of ferromagnetic parts.

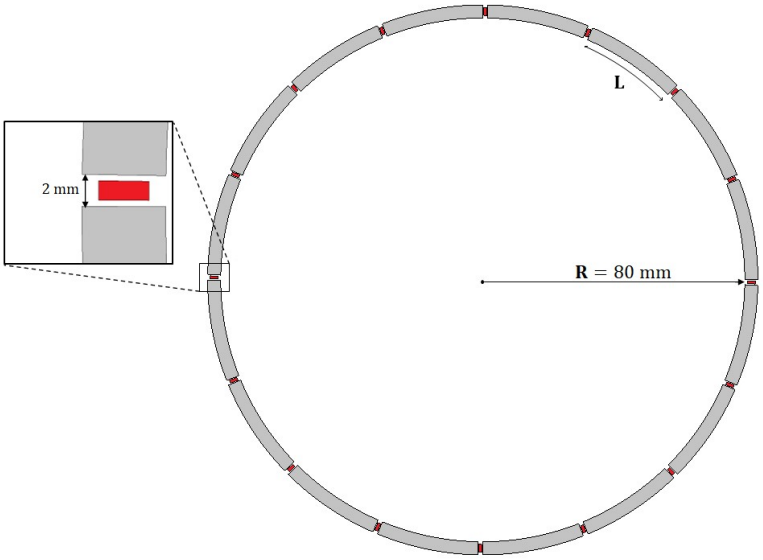

Figure 4.1: Circular analyzer dimensions and sensors distribution

4.2 Effect of the circuit analyzer design on the external magnetic field measurements

Before analyzing the external magnetic field obtained by the new design, Fig(4.2) depicts the distribution of sensors in the two analyzer geometries with respect to the PEMFC emulator models. Then, using Finite Element Simulation (FES), the external magnetic field produced by the 2D emulator and the 3D aluminum emulator models were measured using both analyzers geometries (square and circular).

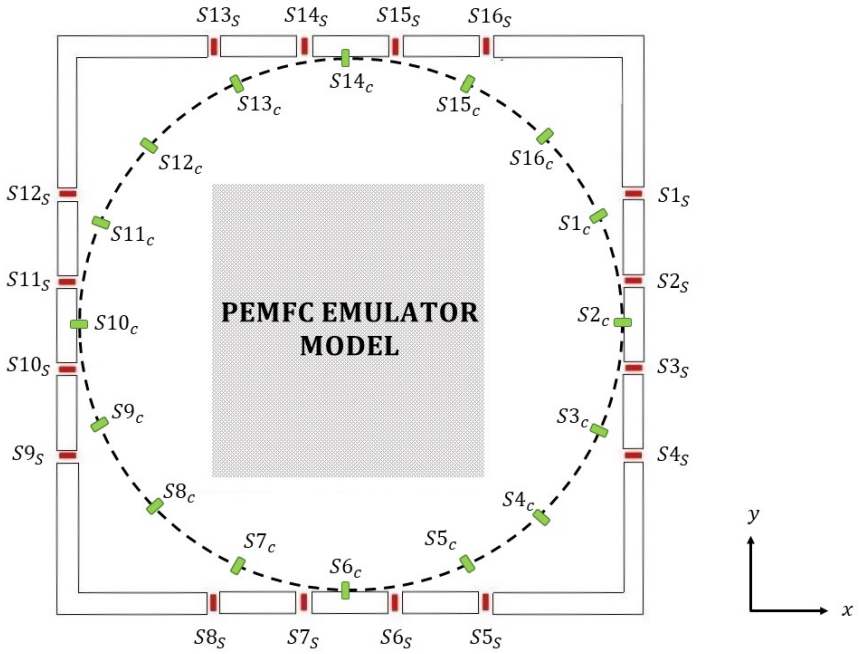

Figure 4.2: Distribution of sensors with respect to PEMFC emulator models in both analyzer geometries.

4.2.1 *2D emulator result*

By considering the normal and faulty behaviors of this emulator presented in section Fig(4.3), Fig(4.4a) shows the produced external magnetic field using the circular analyzer design.

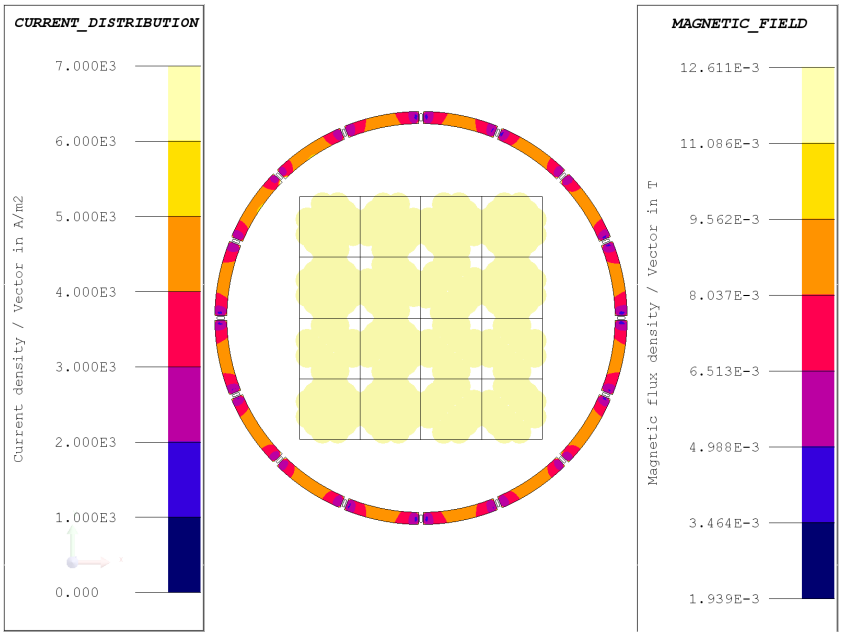

(a)

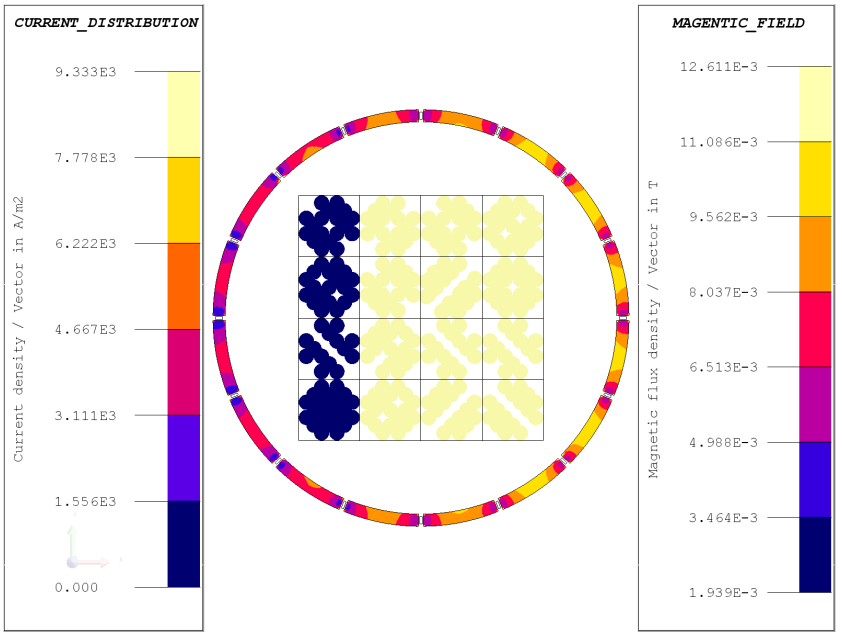

(b)

Figure 4.3: Finite element simulation 2D emulator external magnetic field in (a) Normal and (b) faulty states using the circular design and.

The smooth variation of the external magnetic field between the sensors can be attributed to two main factors. First, the uniform distribution of the sensors at a fixed distance ($R = 80$ mm) around the emulator. Second, the homogeneous distribution of ferromagnetic parts between these sensors. Moreover, the fabricated Δ_B amplitude indicates a modest improvement compared to the produced Δ_B by the square analyzer design, see Fig(4.4b).

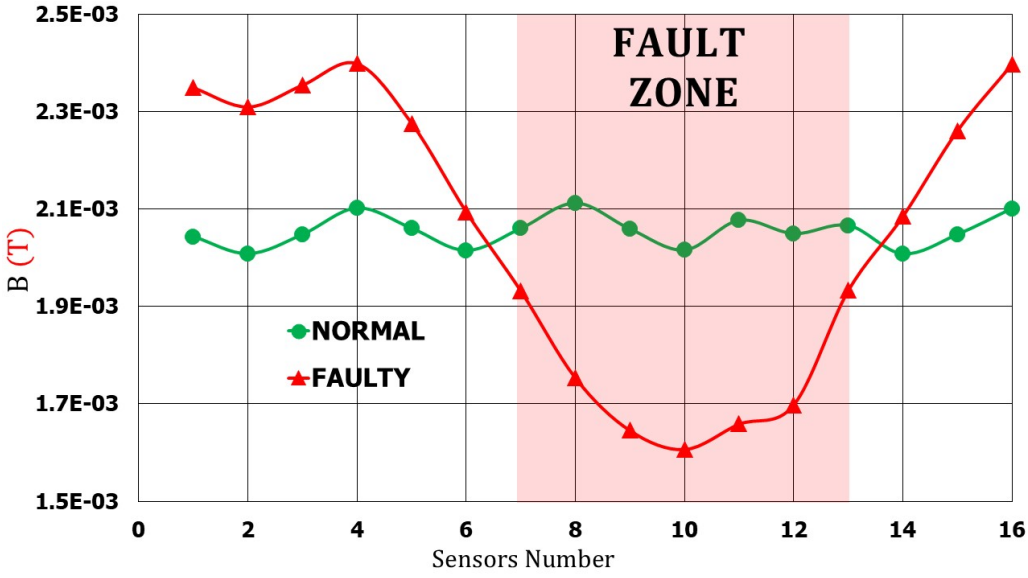

(a)

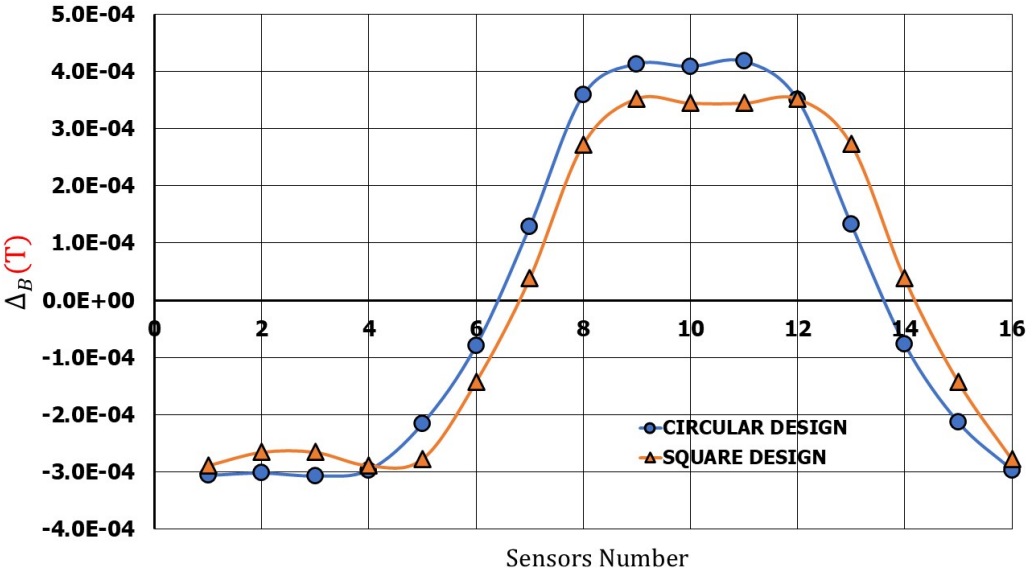

(b)

Figure 4.4: 2D emulator external magnetic field (a) Normal and faulty using the circular design and (b) the fabricated Δ_B compared with the one obtained in square analyzer design.

4.2.2 *3D Aluminium bar*

Comparing the two analyzers geometries by measuring the external magnetic field produced by the 2D model is not sufficient. The current flow inside a real FC is not uniform, especially under faulty operating conditions, the current can deviate at the fault, resulting in a more complex external magnetic field variation. Therefore, the comparison of the two analyzer designs is repeated again using the 3D aluminum bar explained by more realistic current flow at the fault, see Fig(2.27). The new design is tested and compared in both fault detection (2D and 3D).

4.2.2.1 2D fault detection

This kind of detection was explained by locating the circular design around the fault level, see Fig(4.5). Moreover, to validate that the current will not flow in the affected region, this fault was described by an airgap at the left of the aluminium bar of 3 mm thickness and 25 mm width.

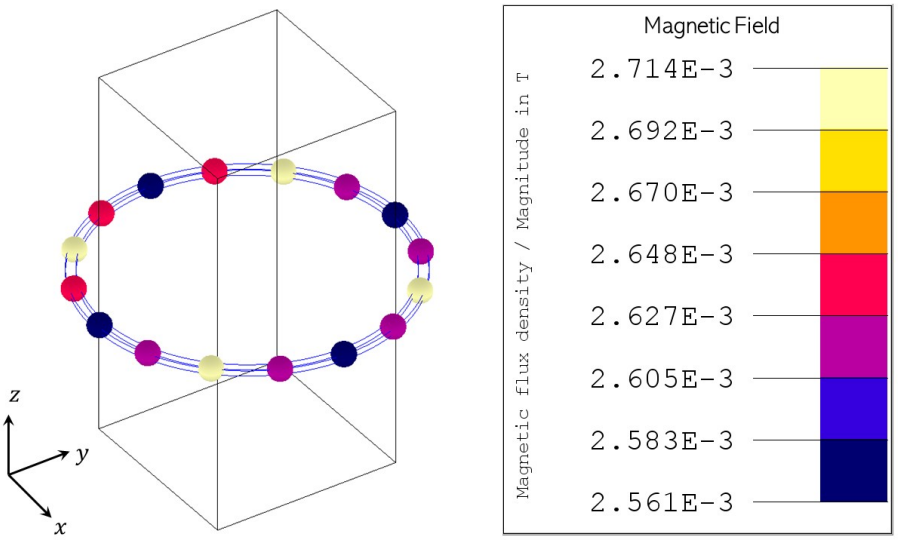

(a)

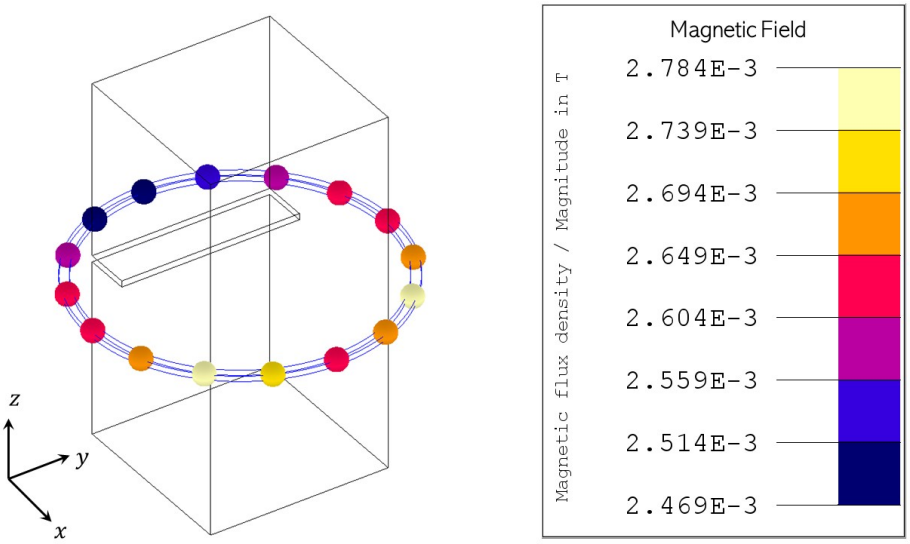

(b)

Figure 4.5: 3D Aluminium bar emulator external magnetic field in (a) Normal and (b) faulty operation conditions.

Consequently, the produced external magnetic field measured by the circular design in different emulator operations is illustrated by Fig(4.6). Furthermore, the magnetic field amplitude variation between the sensors demonstrates the current flow deviation around the affected region across z-axis. In addition, these deviations will also drops the magnetic field amplitude which affects the fabricated Δ_B in Fig(4.7) compared to the obtained Δ_B by the 2D emulator in Fig(4.4b). Again, the circular analyzer design sows a slight improvements in Δ_B which is used to diagnose the fault position inside the FC.

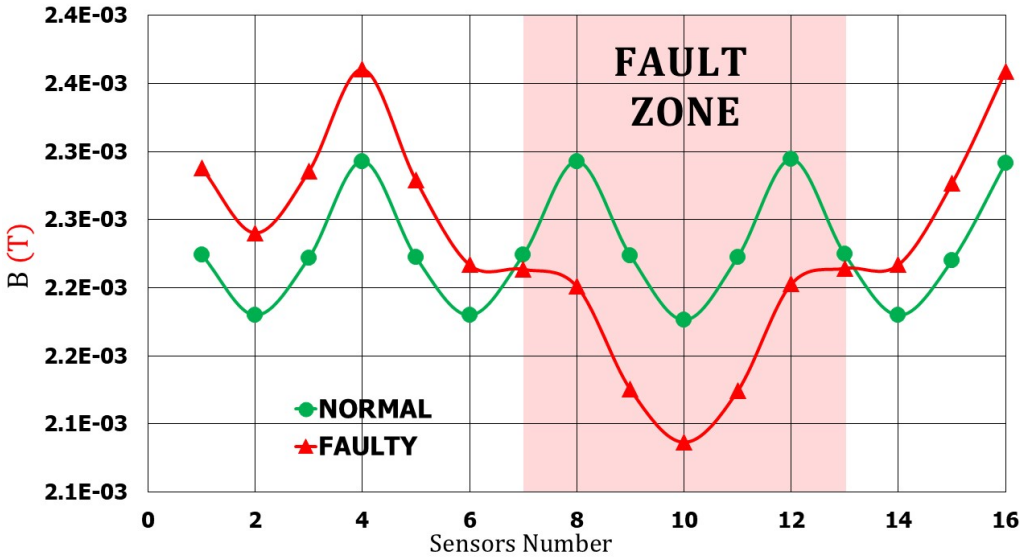

Figure 4.6: 3D emulator external magnetic field Normal and faulty using the circular design

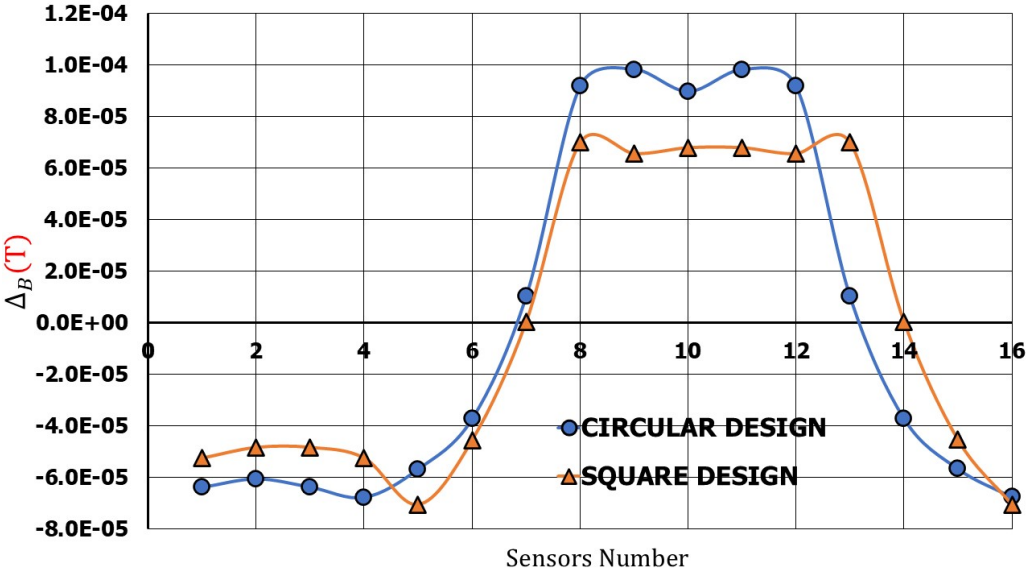

Figure 4.7: 3D emulator produced Δ_B compared with the one obtained in square analyzer design.

4.2.2.2 3D fault detection

In the 3D detection, a step forward was taken to detect the current flow deviation around the fault through measuring the generated external magnetic field. Then, in both analyzer designs, a set of magnetic measurements were done at different analyzers positions, see Fig(2.30a) . Moreover, Fig(4.8) illustrates the fabricated $\mathcal{E}$ at each position of the analyzers geometries (circular and square). Therefore, using the circular analyzer design improves the average $\mathcal{E}$ (3D fault detection) over the analyzer sensors by 12.8 %

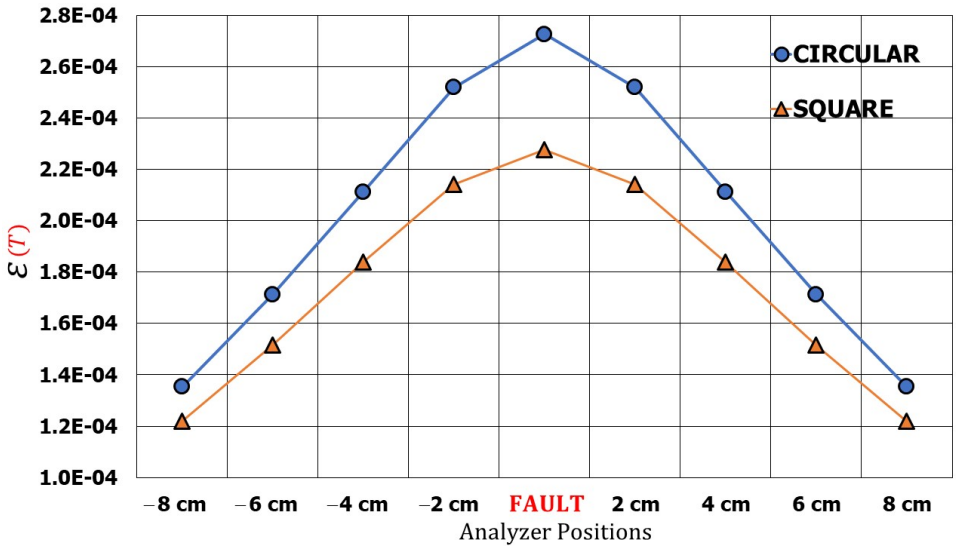

Figure 4.8: Aluminium bar 3D fault detection using square and circular analyzers designs

4.3 Circuit analyzer parametric characterization

Varying the geometric parameters of the ferromagnetic analyzer can affect the external magnetic field at the sensor levels in both analyzer designs, the main variations in geometric parameters were considered as following:

- Variation of the sensors air gaps width
- Variation of the circuit analyzer dimension
- Variation of the number of sensors inside the analyzer

These analyses are performed on the 2D PEMFC emulator Fig (2.1) that explains a non-complex current density distribution which can be easily detected by the magnetic sensors inside the circuit analyzer. The use of the 2D model helps to detect the optimal geometrical parameters needed to obtain the best magnetic field reading by the magnetic sensors. The optimization of the geometry of the circuit analyzer was studied based on the variations of the geometrical parameters with respect to $\overline{\Delta_B}$ in Eq(4.1) produced by the magnetic sensors inside the circuit analyzer, where n_s is the sensor number inside the analyzer and Δ_B is the external magnetic field difference.

$$\overline{\Delta_B} = \frac{1}{n_s} \sum_{i=1}^{n_s} |\Delta B_i| \tag{4.1}$$

From Eq.(4.1), the higher $\overline{\Delta_B}$ value with respect to the variation of geometrical parameters explains a better fault detection by the magnetic sensors. This is due to the increase of Δ_B amplitude between the normal and the faulty PEMFC stack operation. To test the efficiency of Eq.(4.1), the standard variation equation is applied on Δ_B produced by each sensor at each parametric variation of the analyzers. The obtained results shows the same graph format but with lower amplitude.
Before varying the analyzers geometric parameters (airgap width and number of sensors), it is important to fix the sensors at equivalent distance from the 2D emulator in both analyzers geometries. Since the presented 2D emulator results in $chapter\ 2$ and $chapter\ 3$ is applied on $160 \times 160\ mm$, the new geometry of the new circular analyzer is presented with $R = 80\ mm$. Tab(4.1) presents the default geometric parameters used for both analyzer models (square and circular).

Table 4.1: Default geometric parameters of the analyzer models

	Square	*Circular*
Air Gap (mm)	2	2
Thickness (mm)	3	3
Number of Sensors	16	16
Analyzer Dimensions (mm)	160x160	R = 80

4.3.1 *Variation of sensors air gap width*

The high permeability of ferromagnetic materials amplifies the magnetic field reading within the volume of the material. In addition, measuring the external magnetic field near this material will also be amplified compared to the default magnetic value distributed in air. To analyze the ferromagnetic material effect on sensor measurements, the air gap of the sensors of the circuit analyzer varies between $1.1\ mm$ and $3\ mm$. Fig(4.9) show simulations results of the $\overline{\Delta_B}$ of the 16 sensors inside the square and circular ferromagnetic circuit analyzer with respect to the air gap variation. The effect of varying the sensor air gap width is inversely proportional to the $\overline{\Delta_B}$ measurements of the 16 sensors in both analyzer models. Therefore, the circular design has a smoother variation due to the homogeneous distribution of the ferromagnetic parts between the sensors.

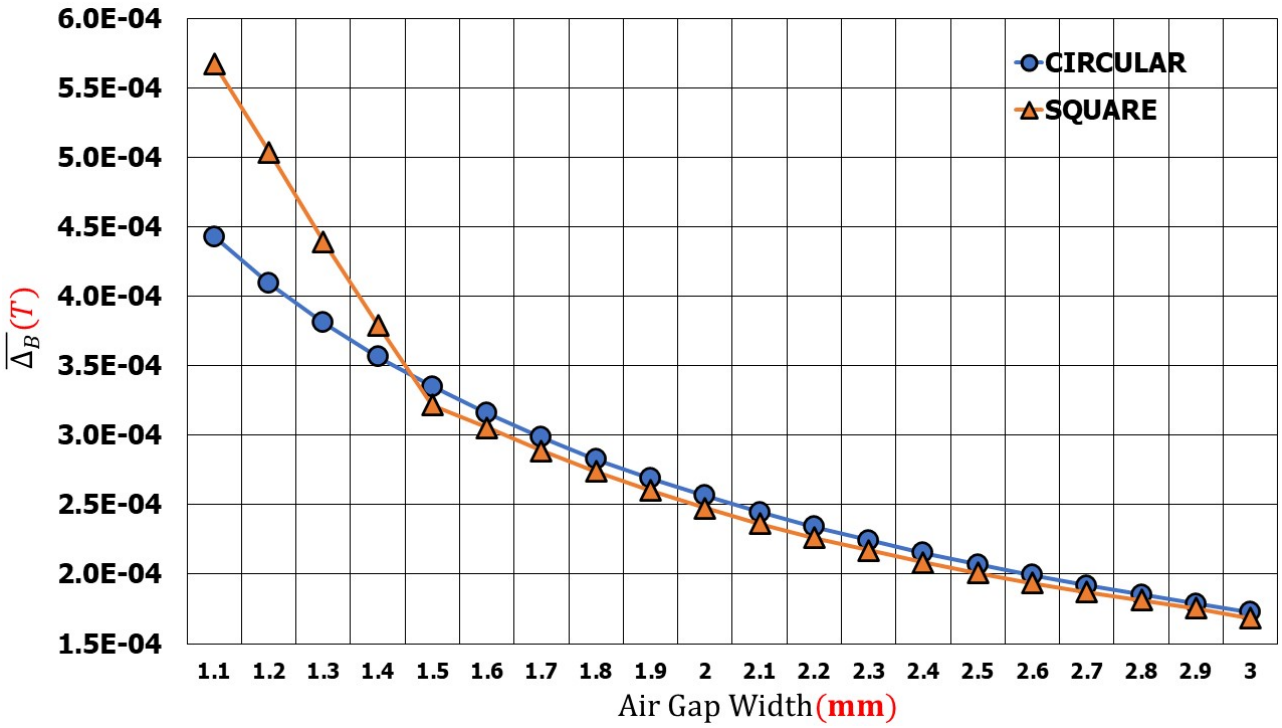

Figure 4.9: Air gap variation of the square and circular analyzer

4.3.2 *Variation in analyzers dimensions*

A variety of tests are done on varying the analyzers dimensions to analyze the effect of these variations on the produced magnetic field at the sensors level between the ferromagnetic analyzer parts. These

tests are done by varying the distance between emulator center and the circuit analyzer sides from 80 mm up to 100 mm each 1 mm in both analyzers designs.

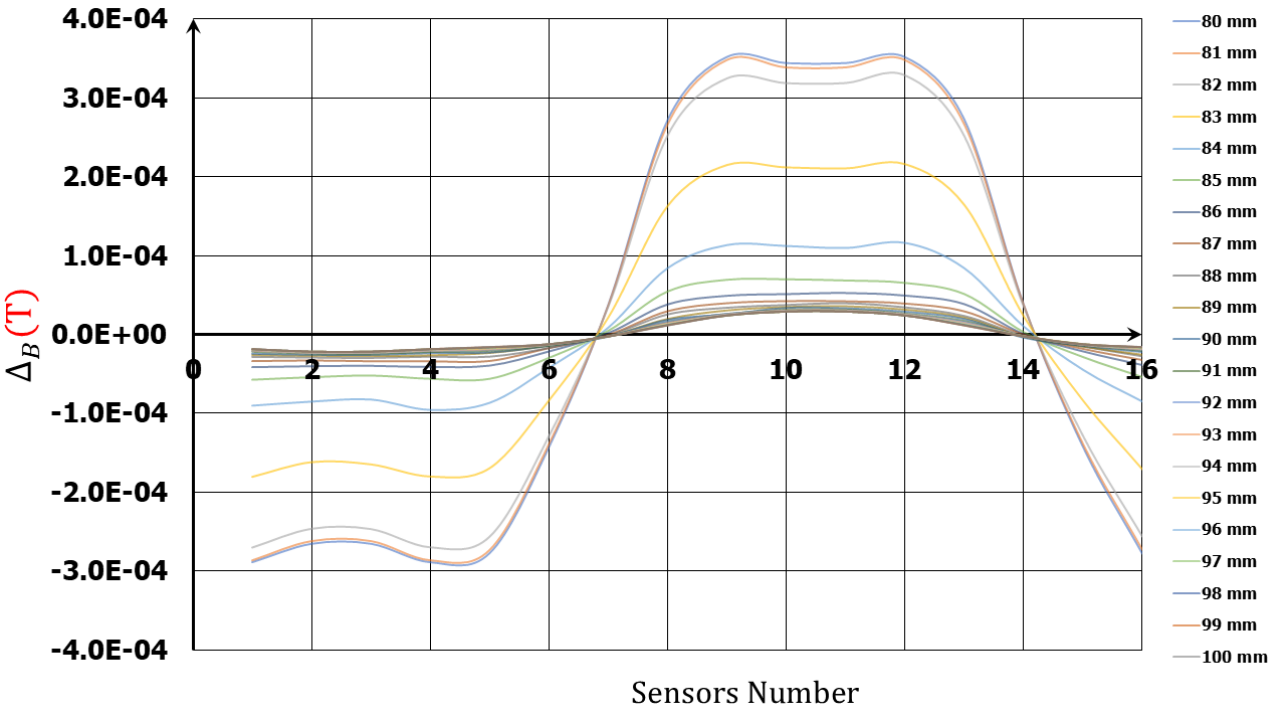

(a)

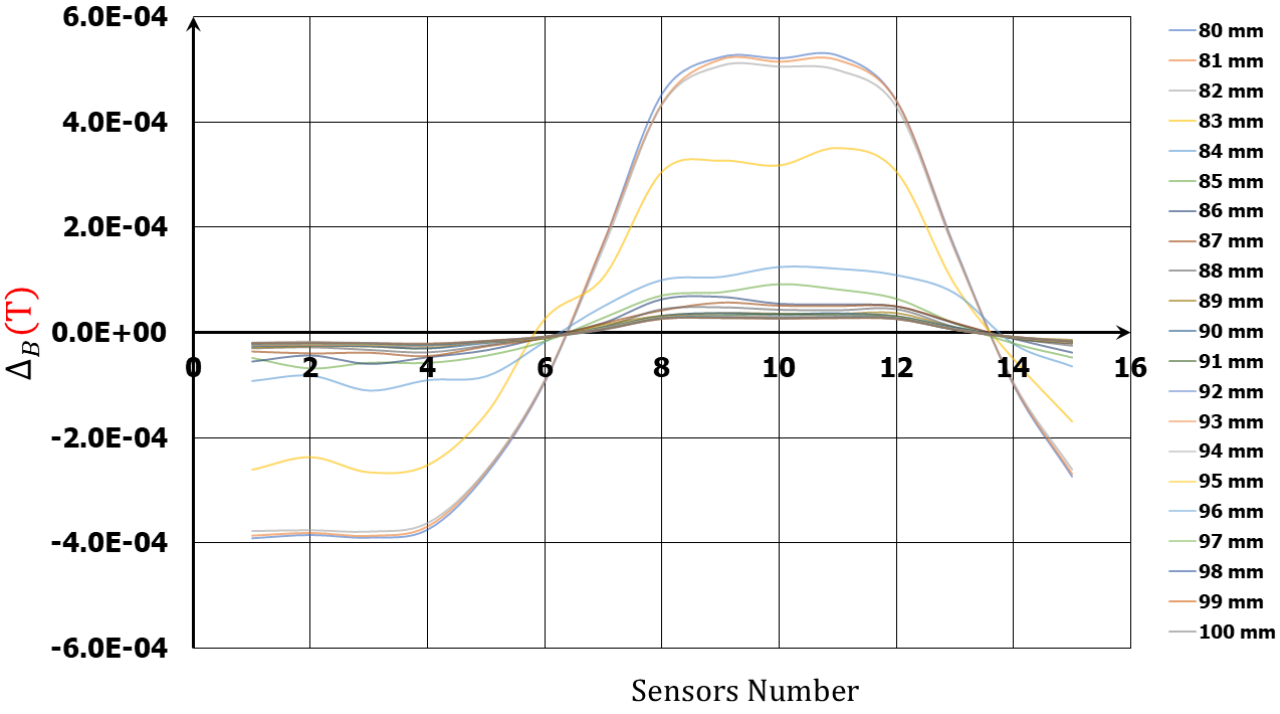

(b)

Figure 4.10: Produced Δ_B at different dimensions of (a) Square, and (b) Circular analyzers designs.

Fig(4.10) depicts the obtained Δ_B at each analyzer position for both geometries. Moreover, Fig(4.11,4.10) illustrates that using the circular design for $80\ mm \leq R \leq 83\ mm$ enhance the magnetic field measurements by 12.8 % compared to the obtained measurements in the square design.

Moreover, the influence of the distance demonstrates that for $R \geq 85\ mm$ the effect of the analyzer geometry on the measured external magnetic field produced by the emulator will be negligible.

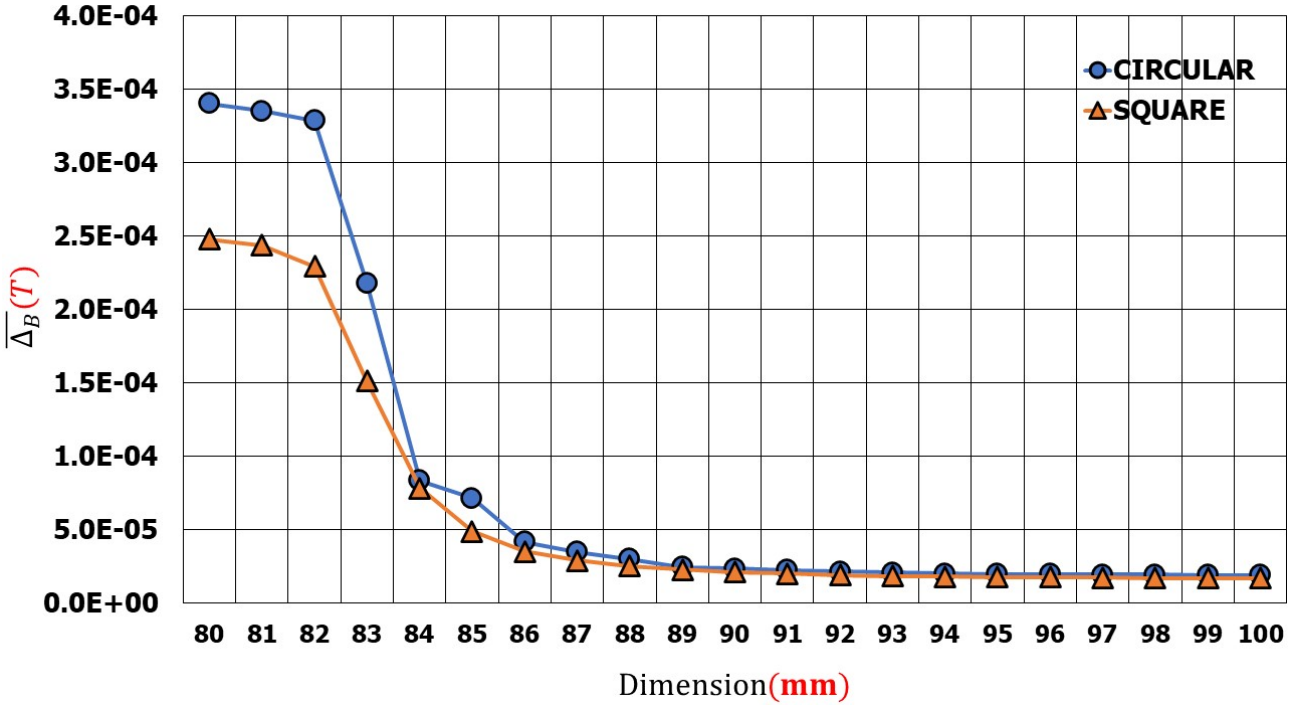

Figure 4.11: Analyzer dimension variation of the square and circular analyzer

4.3.3 *Varying sensors number*

After studying the effect of variations in sensor air gap and circuit analyzers dimensions, improving external magnetic measurements by decreasing the number of sensors inside these analyzers would also be interesting to analyze. The results given in Figs(4.9,4.11) explains the lower sensor air gaps width and smaller analyzers dimension produces a better diagnostic signal for Δ_B. But due to experimental limitations of the 2D emulator regarding the implementation of sensors inside air gaps and the better results given by the smaller analyzers dimension, in this section, these two parameters were considered as those presented in Table (4.1).

4.3.3.1 8 sensors

In order to study the impact of the number of magnetic sensors in the circuit analyzer on the external magnetic field measurements of the FC stack, the number of magnetic sensors was reduced from $ns = 16$ to $n_s = 8$ in both circuit analyzer models. In addition, having the same position of sensors when $n_s = 16$ and $n_s = 8$ in both circuit analyzer designs. Fig(4.12) depicts the distribution of the 8 sensors in the two circuit analyzer models. These sensors were arranged in the same $(clockwise)$ order of the 16 sensors. In the circular design, the odd sensors were considered while, in the square analyzer, the two center sensors on each side were removed. Farther more, decreasing the number of sensors inside the circuit analyzer will increase the volume of the ferromagnetic parts of the circuit analyzer between the magnetic sensors, which amplifies the external magnetic field around the FC stack, leading to higher detection of Δ_B in both circuit analyzer designs.

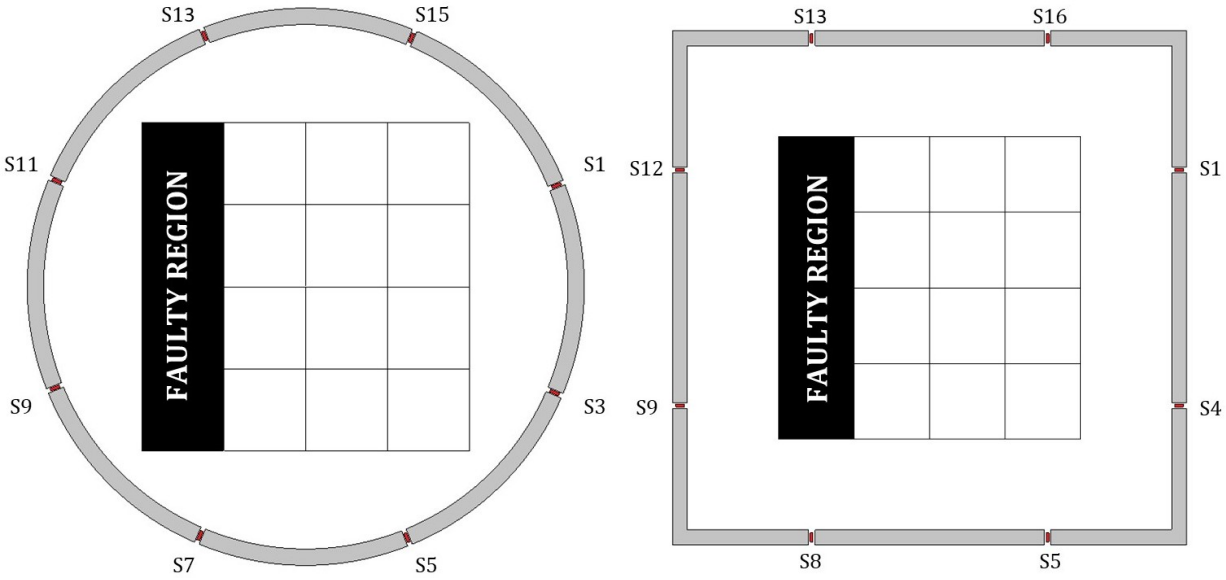

(a) (b)

Figure 4.12: 8 sensors distribution with respect to the fault position in (a) circular ($R = 80\ mm$, and (b) square analyzer ($160 \times 160\ mm$) designs.

The higher magnetic field distribution inside the square analyzer using 8 sensors in both normal Fig(4.13) and faulty Fig(4.14) operation conditions is due to the greater ferromagnetic parts distribution between the sensors compared to the 16 sensors distribution, see Fig(2.4). Hence, the amplitude of the fabricated Δ_B will increase, see Fig(4.15).

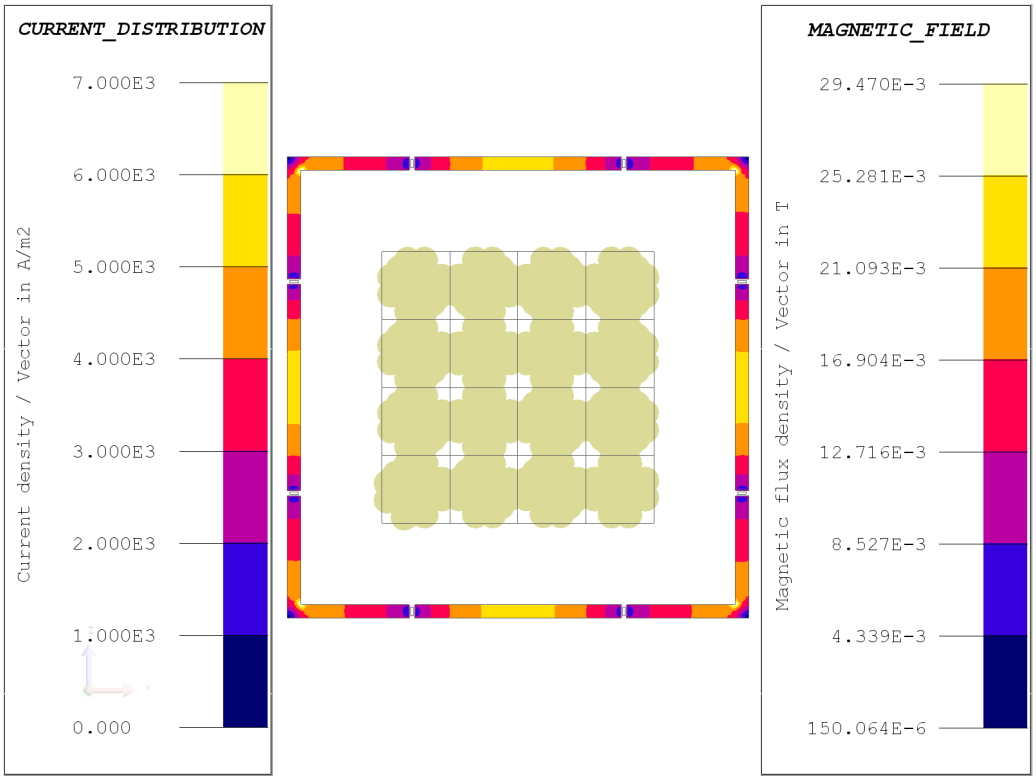

Figure 4.13: Finite element simulation 8 sensors distribution with respect to the square analyzer in normal 2D emulator operation conditions.

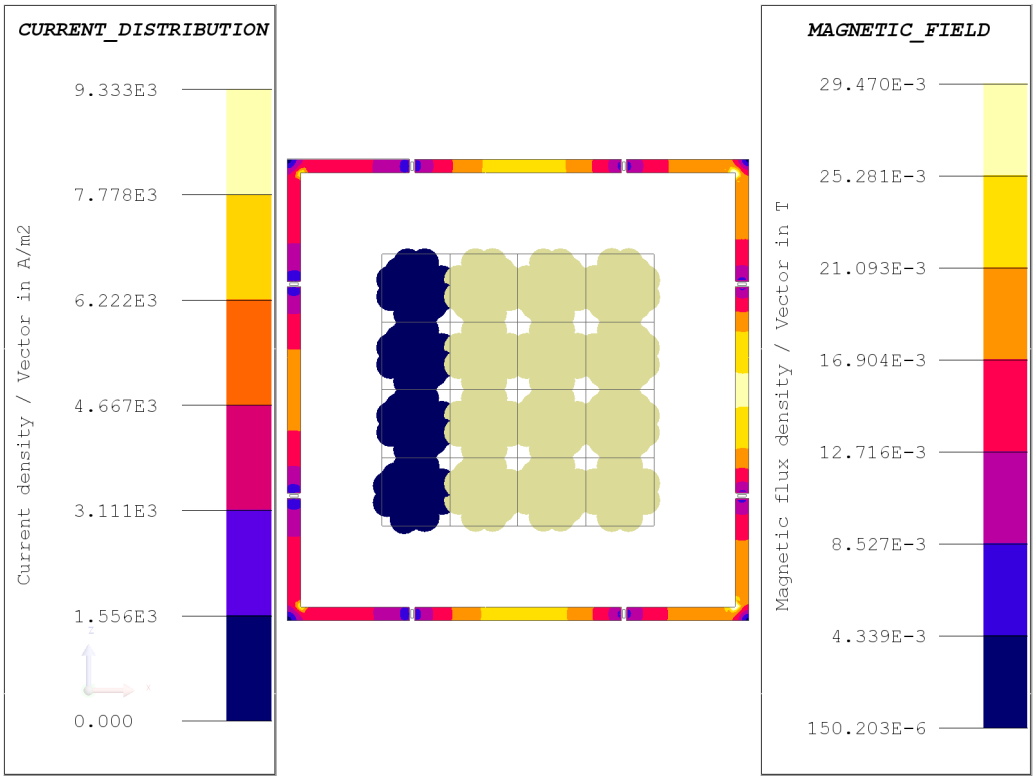

Figure 4.14: Finite element simulation 8 sensors distribution with respect to the square analyzer in faulty 2D emulator operation conditions.

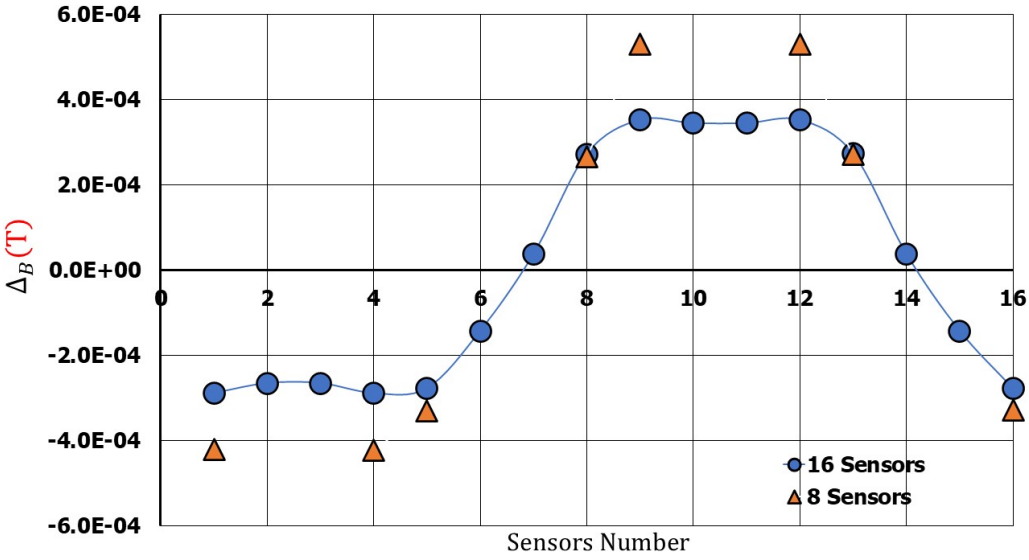

Figure 4.15: Δ_B for 8 sensors and 16 sensors configurations of the square analyser.

Similarly, Fig(4.16) and Fig(4.17) demonstrates the amplified magnetic field distribution inside the circular analyzer design in both normal and faulty emulator conditions. This amplification is explained by the linear relation between the magnetic sensors measurements and the ferromagnetic material volume between the air gaps of the circuit analyzer designs. Thereby, Fig(4.18) illustrated the produced Δ_B in comparison with the Δ_B fabricated from Fig(4.3).

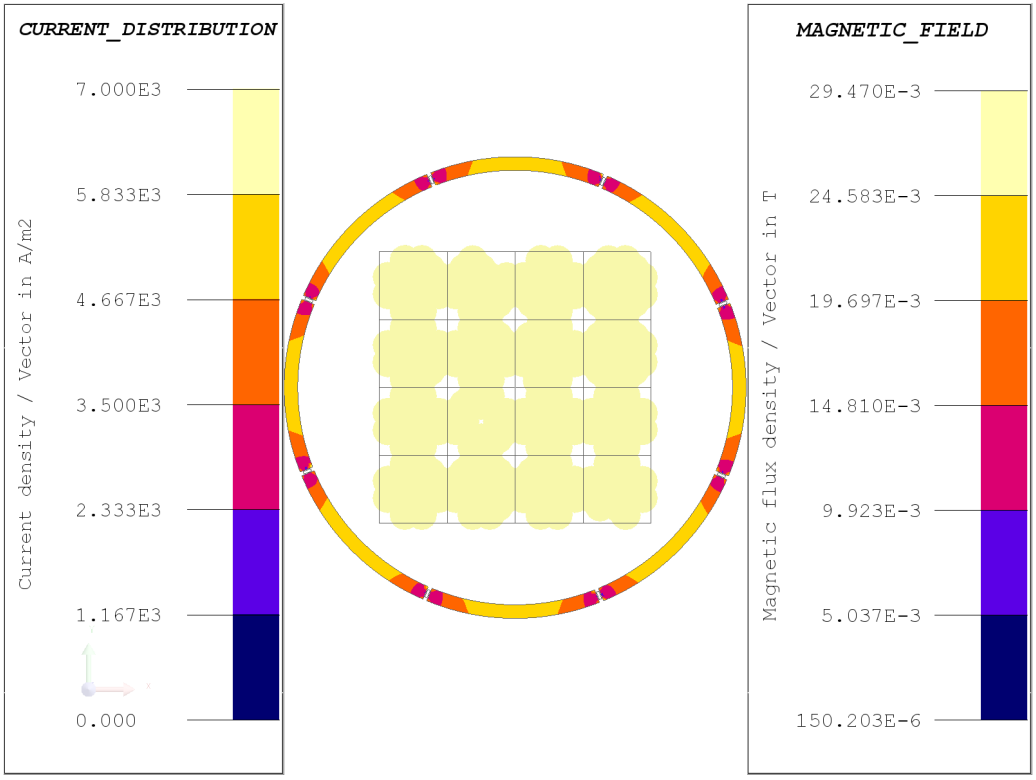

Figure 4.16: Finite element simulation 8 sensors distribution with respect to the square analyzer in normal 2D emulator operation conditions.

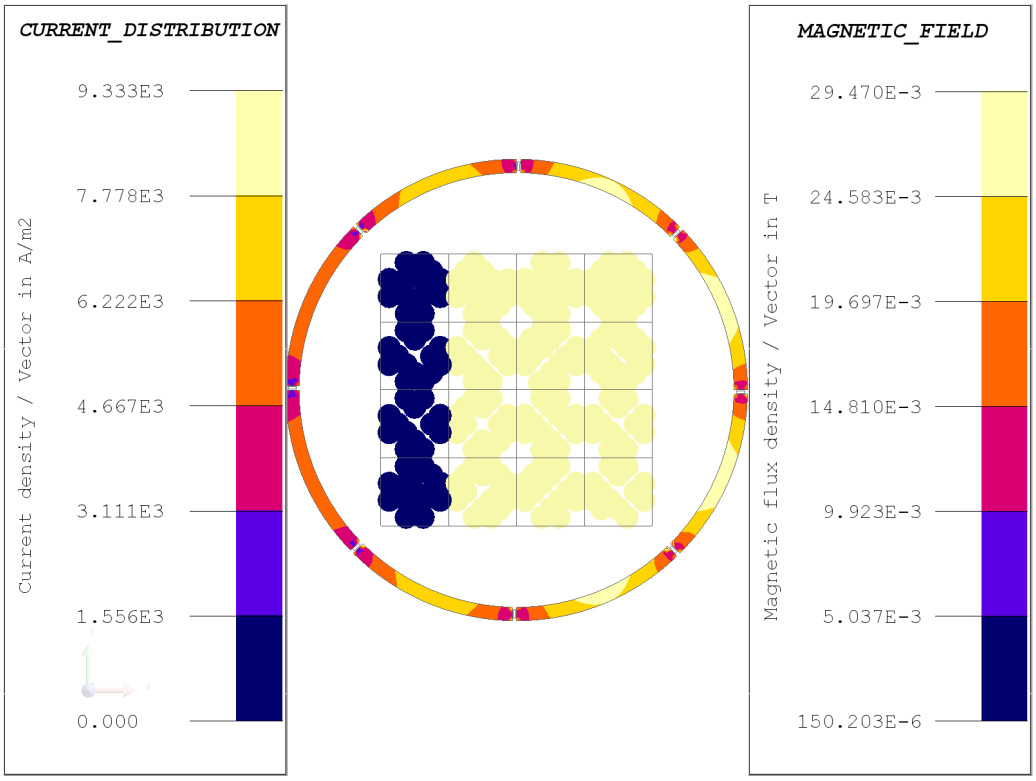

Figure 4.17: Finite element simulation 8 sensors distribution with respect to the square analyzer in faulty 2D emulator operation conditions.

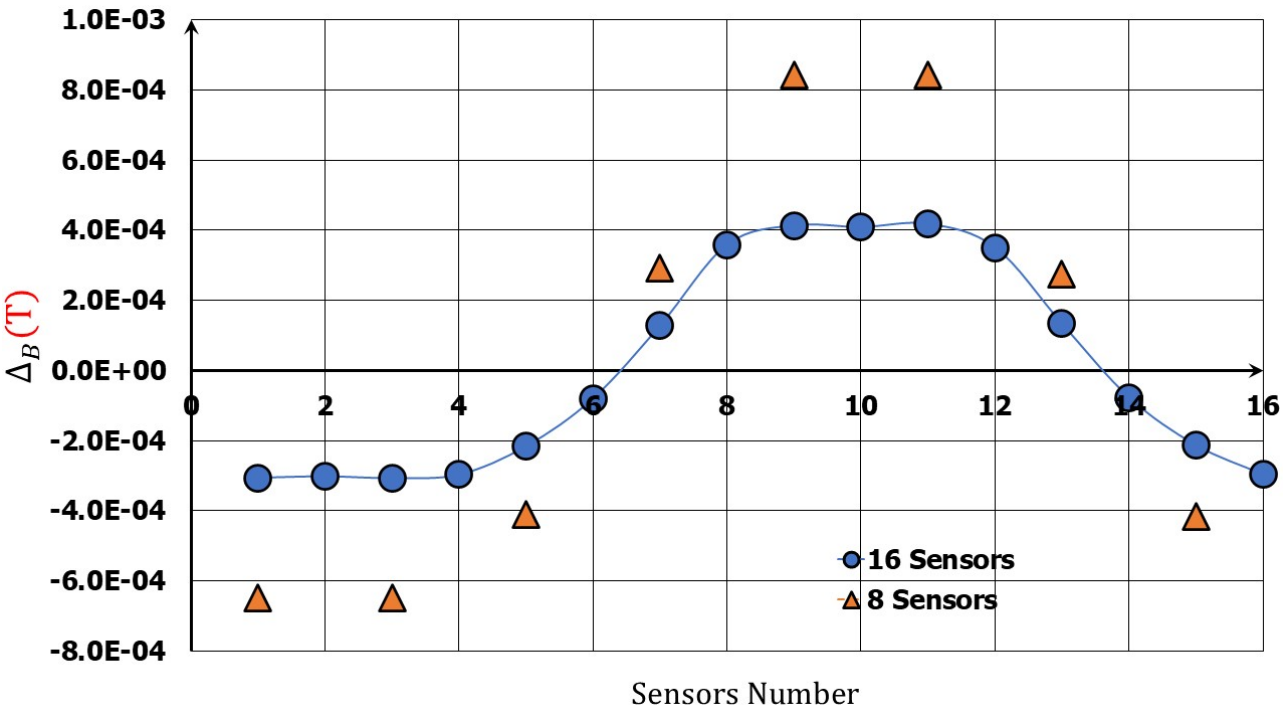

Figure 4.18: Δ_B for 8 sensors and 16 sensors configurations of the circular analyser.

4.3.3.2 One rotating sensor

The results obtained by varying the size of the analyzer and decreasing the number of sensors show that using the circular analyzer for $R \leq 83$ mm is more efficient than the square design. This is due to the higher amplitude of Δ_B produced by the circular analyzer. Therefore, using the circular design for $R = 80$ mm, the single sensor were implemented in the circuit analyzer to rotates in a clock wise direction around the FC emulator, see Fig(4.19). This sensor rotates at 16 different positions equivalent to the sensors distribution presented in Fig(4.2) $(Circular\ design)$.

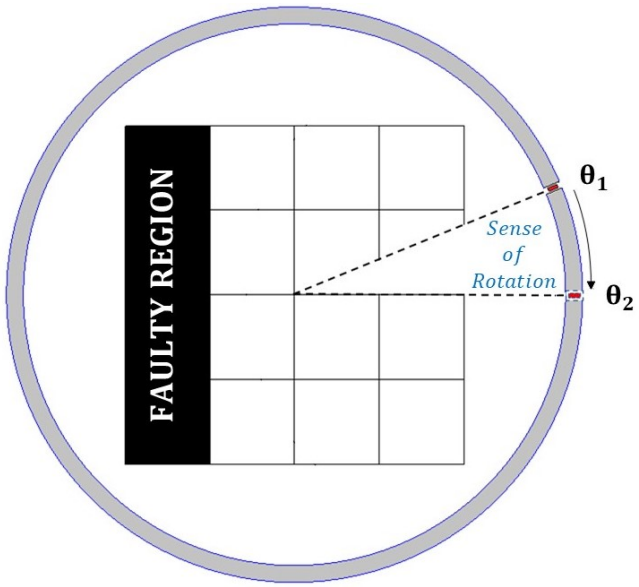

Figure 4.19: Circular analyzer design single sensor rotation

Fig(4.20a) illustrates the external magnetic field measured in both emulator operating conditions. Moreover, the Δ_B fabricated in Fig(4.18) reveals that the larger the ferromagnetic volume, the higher the amplitude of the Δ_B obtained.

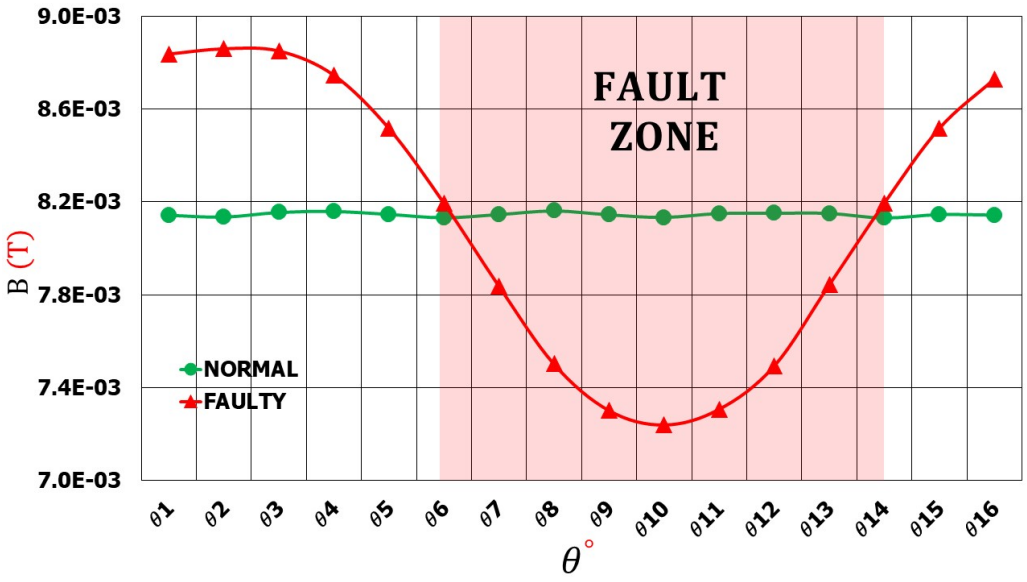

(a)

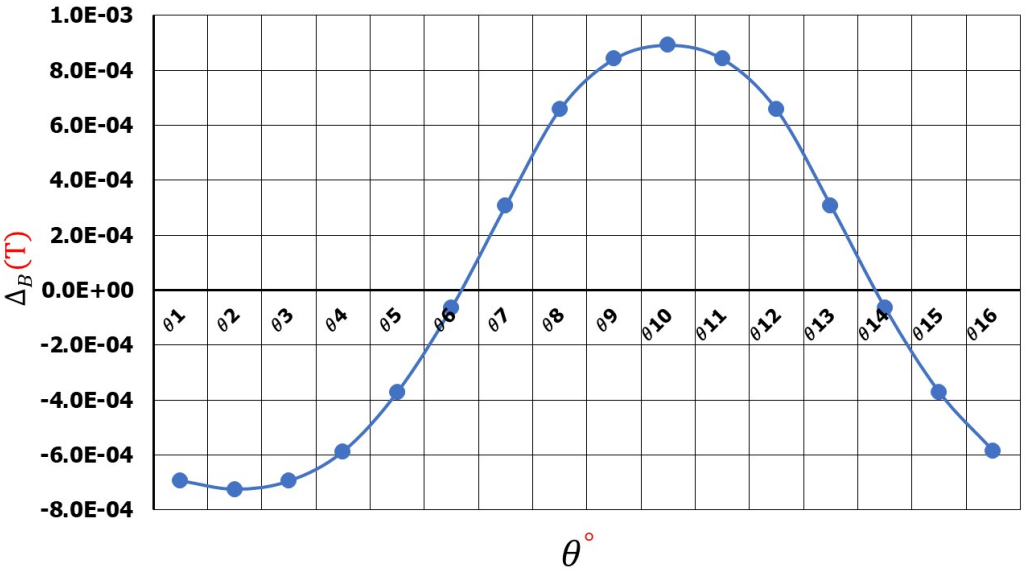

(b)

Figure 4.20: The measured (a) external magnetic field in normal and faulty emulator operation with (b) the produced Δ_B using a single rotating sensor.

The usage of a single sensor clearly improves the external magnetic field produced by the current flow inside the FC stack. Comparing the magnetic field measured for different numbers of sensors, the single sensor gives the largest magnetic field amplitude in both emulator operation conditions, see Fig(4.21). This is due to the homogeneous distribution of the external magnetic field inside the ferromagnetic circuit analyzer, which amplifies the measurements as the sensor air gaps decrease.

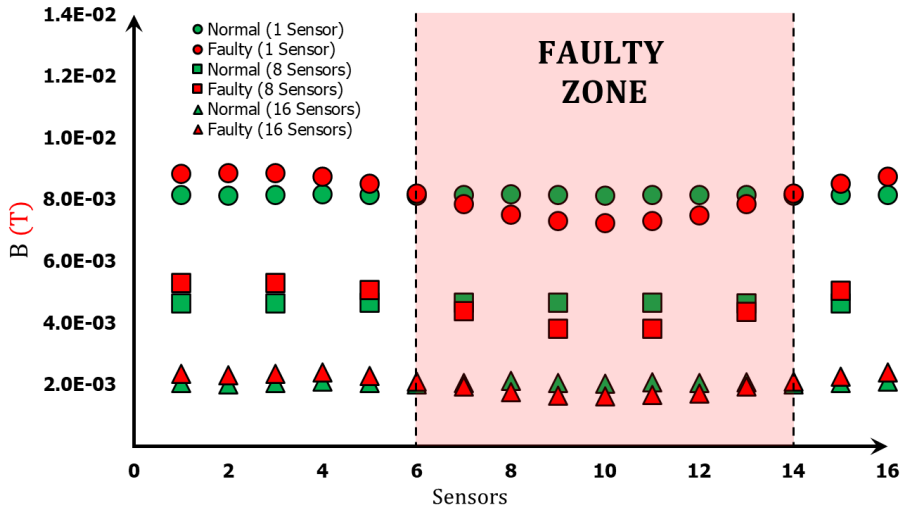

Figure 4.21: Produced magnetic field in both emulator operation conditions for different number of sensors

As an illustration, Fig(4.22) shows the Δ_B made with different numbers of sensors. The use of 16 sensors indicates the lowest amplitude of Δ_B, which is explained by the larger number of air gaps that leads to a magnetic drop inside the analyzer. On the other hand, the Δ_B produced using 1 sensor and 8 sensors are overlapped. In addition, another test was performed by rotating the single sensor in 8 different positions to study the influence of the analyzer air gaps on the amplification of the measurements. This test shows the Δ_B is equivalent to that produced using 8 sensors. Therefore, this phenomenon illustrates that the magnetic amplification inside the circuit analyzer has some limitations regarding the volume of ferromagnetic material next to the magnetic sensor air gap.

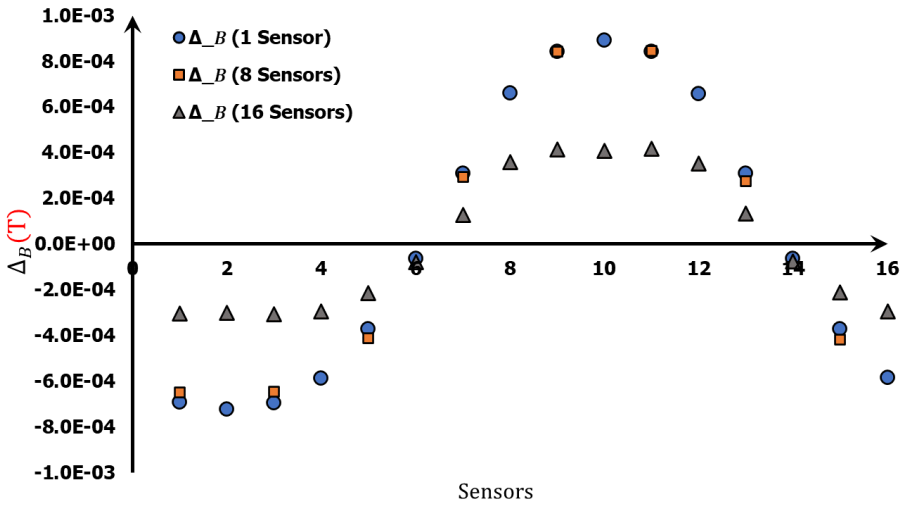

Figure 4.22: Fabricated Δ_B for different number of sensors.

As a result, the use of a single sensor still has an advantage over the others, since the same amplitude of the Δ_B was calculated using 8 sensors, but with fewer sensors, which reduces the cost. However a single sensor analyser would need to be coupled to an actuator ensuring its rotation. This type of measurement gives a better representation of the fault position that can be expected within the FC.

4.4 Analyzers representation with respect to real FC dimensions

In Fig(4.11), the $\overline{\Delta_B}$ analyzed at the sensors is calculated using the 2D emulator of $100\ mm$. These dimensions express the active area of the FC where the current is flowing. In fact, the use of the circular analyzer for $80\ mm \leq R \leq 83\ mm$ is not applicable around the FC due to the actual dimensions of the FC.

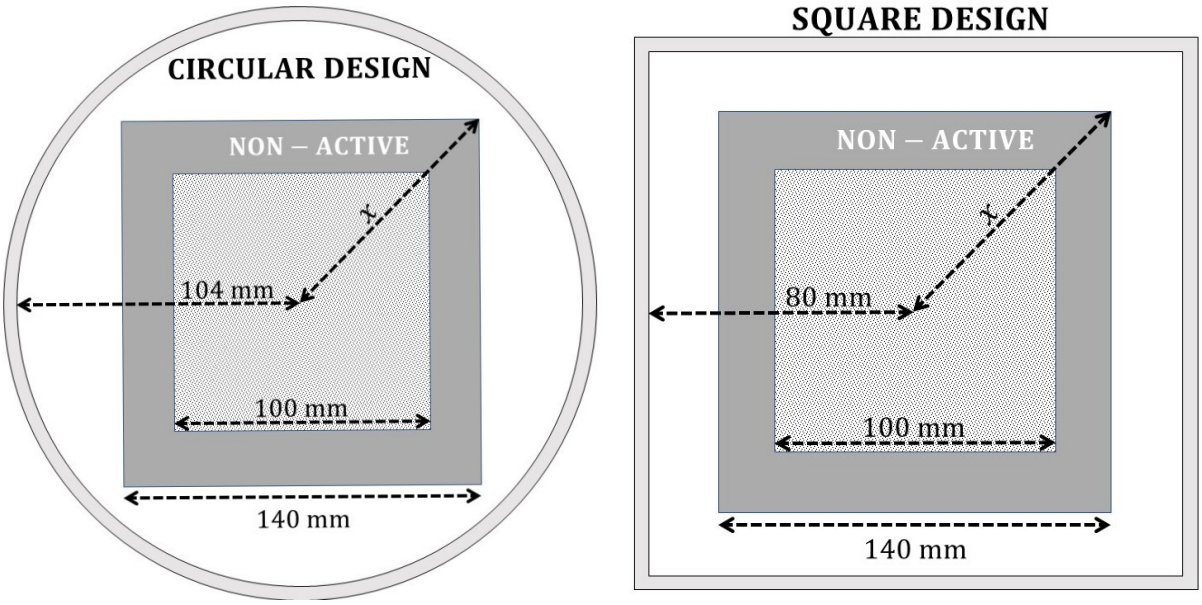

(a) (b)

Figure 4.23: FC dimensions used in experimental test bench with respect to (a) Circular and (b) Square circuit analyzers.

To avoid the intersection of the analyzer with the edges of the FC, Fig(4.23) illustrates the accessible dimensions for the analyzers around the FC used in our experimental test bench. Consequently, by using this geometry of the FC with the square analyzer, the sensors are located at a distance equivalent to half the analyzer width ($160\ mm$) from the FC center. Hence, the placement of the sensor in the circular design is located for $R \geq 104\ mm$. The placement of these sensors at a shorter distance allows for a better Δ_B amplitude needed to diagnose the position of the defect within the FC. Fig(4.24) demonstrate the fabricated Δ_B of the 2D emulator using the single rotating sensor of ($R = 104\ mm$) and the $160 \times 160\ mm$ square design of 8 and 16 sensors. The results obtained explains depicts that the distance of the sensor from the FC has more effect than the effect of the ferromagnetic material volume near the sensor. The produced Δ_B in the single rotating sensor of ($R = 104\ mm$) and the 8 sensors in the square design have a similar magnitude. Therefore, the advantage of distance over the effect of the ferromagnetic material becomes clear when the Δ_B amplitude produced by the single rotating sensor is compared to that of the 8-sensor representation in a $160 \times 160\ mm$ design.

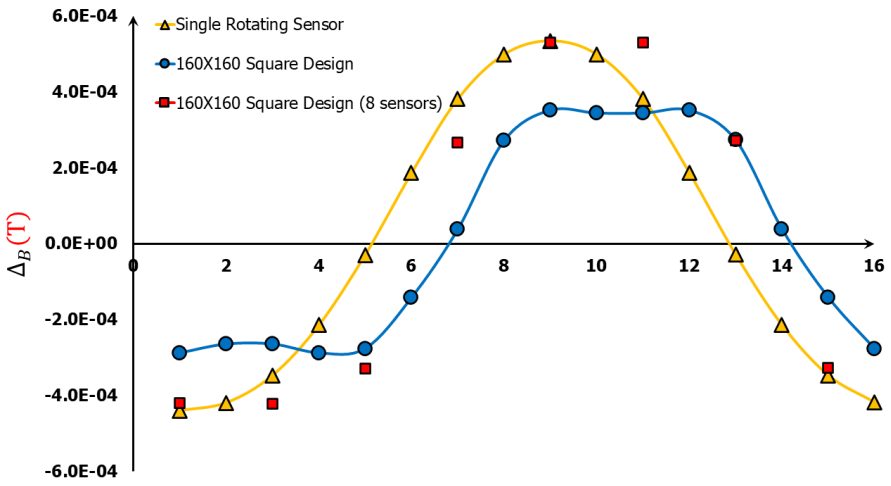

Figure 4.24: Fabricated Δ_B using the single rotating sensor of ($R = 104\ mm$) and the 160×160 mm square design of 8 and 16 sensors.

4.5 Conclusion

In this chapter, a new circuit analyzer design has been proposed. This design was applied on the aluminum bar emulator and compared with the results obtained by the square design to test the effectiveness of the new design in detecting the 3D current flow distortion. The results obtained indicate a 12.8% improvement in the proposed method for 3D fault detection. In addition, both analyzer geometries were applied on the 16-bar emulator, which explains the homogeneous and heterogeneous 2D current flow inside the active FC area.
Based on the results obtained by varying the dimensions of the analyzers using 16 sensors, the circular analyzer geometry shows a slight improvement over the square analyzer geometry. This improvement was seen at a close distance between $80\ mm$ and $83\ mm$ from the position of the sensors and the center of the emulator. When this distance exceeds $83\ mm$, the effect of the analyzer geometry is negligible. On the contrary, considering the real geometry of the PEMFC ($140 \times 140\ mm$) stack applied in our study, the use of the square design is more effective and applicable due to the position of the sensors around the stack. In the circular analyzer, the sensors should be positioned $104\ mm$ away from the center of the FC active area to avoid the intersection of the ferromagnetic circuit analyzer with the edges of the PEMFC stack. On the other hand, using the square design of the circuit analyzer, the sensors are positioned at $80\ mm$ to obtain the default circuit analyzer used in our study (160×160 mm). Therefore, with respect to the analyzed results of the dimensions of the analyzer using 16 sensors, using the square design of the analyzer around a real FC will fabricate a better amplitude of Δ_B. This chapter also presents the variation in the number of sensors in the two analyzer designs. The analysis shows that, up to a specific limitation, decreasing the number of sensors will improve the Δ_B produced in both geometric designs, but the circular analyzer still has the advantage over the square design by applying a rotating sensor around a small FC model, for example $10 \times 10\ cm$ dimensions. On the contrary, due the square design of the real industrial fuel cells and based on the results illustrated in Fig(), implementing 8 sensors in a square ferromagnetic analyzer design near the FC will improve Δ_B amplitude used to diagnose fault position.

Finally, based on the results obtained from the measurements of a single rotating sensor and the square design of 8 sensors, the 160×160 model with 8 sensors would be interesting to test in the 2D and 3D fault diagnosis of our passivated FC emulator.

GENERAL CONCLUSION AND PERSPECTIVES

This work presents an innovative method for the identification of the fault position inside the fuel cell. This method is based on measuring the external magnetic field produced by the fuel cell during operation. This methodology use a magnetic field analyzer, which associates the magnetic sensors with a ferromagnetic circuit, which is essentially different in comparison with other methodologies proposed until now. The main advantage of this process is its ¨non-invasive¨ nature. The magnetic field at the sensor levels is amplified which enables a more accurate analysis to diagnose the position of the fault. Moreover, the used circuit analyzer limits the number of measurements: about sixteen which are less than the already existing techniques. The magnetic field analyzer is designed to be placed around the stack and moved along its longitudinal axis in order to detect any internal defects. This system is then build and installed around the 3D current density emulator of a PEMFC, which represents the main contribution of this work.

To achieve our goal, which is the experimental validation of the method, we followed several steps:

The first step is demonstrating the advantage of using the fuel cell modelling in general and PEMFC in specific. Then, the mechanisms of PEMFC operation are presented taking into consideration the various faults that can affect it. The most significant point we focus on is the relationship between the current distribution inside the fuel cell and the faults affecting it.
We have also presented the several diagnosis methods proposed until now. These methods discuss local and global faults based on the current distribution inside the fuel cell. The invasive method directly measures the current value and then identifies the local fault. The non-invasive method identifies local and global faults by mapping the current flow from the fuel cell's external magnetic field. In addition, some studies have applied data-driven diagnostic methods based on the original key variables of the fuel cell to classify the type of fault. We therefore focus the study on the diagnosis of a 3D current density emulator of a PEMFC by measuring the external magnetic field difference Δ_B at different analyzer positions, which is a non-invasive method to give the local fault position.

In the second step, the ferromagnetic analyzer used is described with respect to its geometry and the distribution of the magnetic sensors inside. This circuit analyzer is therefore applied on the 3D emulator to simulate the magnetic signature of several emulated defects. The demonstration of this emulator is based on the multi physical modeling of a FC involving couplings between electrochemical, electrical and magnetostatic models. In addition, this emulator is modeled using finite element simulation (FES) and experimentally validated under normal and faulty operating conditions. This emulator is specially designed to reproduce the electrical behavior like that in a real fuel cell (without the influence of the auxiliaries and the electrochemical considerations). The emulator was powered by a current source to ensure an overall stack current of 70 A. A measurement of the external magnetic field is then obtained for different fuel cell operating states. The heterogeneity of the current density distribution explained by a fault in the electrical conductivity is observed by the variation of the external magnetic field as a function of the health of the proposed emulator.

We were able to validate our technique in two steps:

- On FES model:

A 3D FES formulation based on magnetic scalar potential, that is included in Altair Flux software, has been chosen to solve the coupled electric conduction and magnetic equations. The fault is considered as an insulator to block the current flow through the affected part of the active area. This application is based on the strong coupling between the electrical conduction application that solves the current density flow inside the fuel cell emulator and the magnetic application that computes the internal and external magnetic field generated from the internal current density flow in the emulator domain.

- On Experimental emulator:

In order to obtain a current distribution comparable to that inside the FC volume, a test bench is created in order to hold the ferromagnetic analyzer around the passivated fuel cell emulator, which have a similar geometry and structure as an actual fuel cell stack.

In both experimental and numerical models, the current distribution shows a clear deviation around the faulty region in the affected cell. This is clearly observed on the external magnetic field signature of the proposed emulator. To identify the local current deviation around the conduction fault, a new 3D fault detection method is proposed in our study. Two steps explain this method:

1. In the first step, the external magnetic field is measured at different positions of the circuit analyzer in both emulator operations. Then the Euclidean distance between the sensors Δ_B is computed at each position of the analyzer. The maximum value of the computed Euclidean distance indicates that the analyzer is around the affected cell.

2. Second, after indicating the affected cell, the Δ_B graph obtained by the analyzer position will indicates the fault position inside the affected cell. The positive Δ_B is explained by the drop of the magnetic field for the sensors located close to the conduction fault in which the current is dropped and the negative Δ_B values are obtained for the sensors close to the normal part of the active zone. This phenomenon is due to the conservative global current density, which leads to a current drop at the faulty part and increases in the rest of the conductive part of the emulator.

This work also discusses an off-line fault diagnosis of the PEMFC. The input data for the diagnostic approach were extracted from the external magnetic field difference Δ_B of PEMFC in the presence of the ferromagnetic circuit analyzer. In this first diagnostic validation, a 2D current distribution model and experimental emulator were been used. For each state, an initial current distribution will model the state of health of the FC. If for the normal operation, this current density is considered homogeneous, in a fault case, this current distribution will model the magnitude and the position of the fault. In order to obtain a higher statistical relevance, with a reduced number of experiments, for each state from the initial current distribution, an experimental design will generate a list of variations around the initial current distribution. The obtained dataset is then used as input parameters for training of a decision algorithm. Data are generated from both the experimental emulator and the numerical Finite Element Simulation (FES). This approach clarifies the ability of applying the numerical analysis as a training data-set for the data-driven diagnosis technique using orthogonal arrays designs.

We then propose a new circuit analyzer design is presented to investigate the impact of the magnetic sensor distribution on the external magnetic field measurements of the 2D emulator. In addition,

various geometric parameters of the proposed analyzers, such as air gap width, dimensions, and number of sensors, are modified and refined based on the external magnetic field generated by the 2D emulator model. Therefore, based on the obtained results and experimental limitations, the conclusion reached clarifies the importance of using the square design in our passivated stack model.

Perspectives

As the diagnostic algorithm seems to be effective by using training data from simulation model, a natural following step is to produce a training data by the 3D multi physical fuel cell emulator. Even though the employed magnetic sensors are highly sensitive to the magnetic noise, the proposed method provides a significant efficiency in detecting the 2D and 3D conductive faults, and also can be used as an original variable for data-driven diagnostic methodologies. Therefore, it would be interesting to apply our proposed data analysis methodology on a real FC system by considering the normal and faulty (flooding, drying, air stoichiometry) operation conditions.

BIBLIOGRAPHY

[1] Z. Li, "Data-driven fault diagnosis for pemfc systems," Ph.D. dissertation, Aix-Marseille, 2014.

[2] M. L. Perry and T. F. Fuller, "A historical perspective of fuel cell technology in the 20th century," *Journal of the electrochemical society*, vol. 149, no. 7, S59, 2002.

[3] P. Mock and S. A. Schmid, "Fuel cells for automotive powertrains—a techno-economic assessment," *Journal of Power Sources*, vol. 190, no. 1, pp. 133–140, 2009.

[4] O. B. Inal and C. Deniz, "Assessment of fuel cell types for ships: Based on multi-criteria decision analysis," *Journal of Cleaner Production*, vol. 265, p. 121 734, 2020.

[5] J. Larminie, A. Dicks, and M. S. McDonald, *Fuel cell systems explained*. J. Wiley Chichester, UK, 2003, vol. 2.

[6] P. Lin, P. Zhou, and C. Wu, "A high efficient assembly technique for large pemfc stacks: Part i. theory," *Journal of power sources*, vol. 194, no. 1, pp. 381–390, 2009.

[7] P. Corbo, F. Migliardini, and O. Veneri, *Hydrogen fuel cells for road vehicles*. Springer Science & Business Media, 2011.

[8] S. Toghyani, E. Afshari, and E. Baniasadi, "A parametric comparison of three fuel recirculation system in the closed loop fuel supply system of pem fuel cell," *International Journal of Hydrogen Energy*, vol. 44, no. 14, pp. 7518–7530, 2019.

[9] T. Matsuura, J. Chen, J. B. Siegel, and A. G. Stefanopoulou, "Degradation phenomena in pem fuel cell with dead-ended anode," *international journal of hydrogen energy*, vol. 38, no. 26, pp. 11 346–11 356, 2013.

[10] K. Nikiforow, H. Karimäki, T. Keränen, and J. Ihonen, "Optimization study of purge cycle in proton exchange membrane fuel cell system," *Journal of power sources*, vol. 238, pp. 336–344, 2013.

[11] R. Ahluwalia and X. Wang, "Buildup of nitrogen in direct hydrogen polymer-electrolyte fuel cell stacks," *Journal of Power Sources*, vol. 171, no. 1, pp. 63–71, 2007.

[12] O. Himanen, T. Hottinen, and S. Tuurala, "Operation of a planar free-breathing pemfc in a dead-end mode," *Electrochemistry communications*, vol. 9, no. 5, pp. 891–894, 2007.

[13] D. Jiang, R. Zeng, S. Wang, L. Jiang, and J. R. Varcoe, "Paradox phenomena of proton exchange membrane fuel cells operating under dead-end anode mode," *Journal of Power Sources*, vol. 265, pp. 45–49, 2014.

[14] F.-B. Weng, A. Su, and C.-Y. Hsu, "The study of the effect of gas stoichiometric flow rate on the channel flooding and performance in a transparent fuel cell," *International journal of hydrogen energy*, vol. 32, no. 6, pp. 666–676, 2007.

[15] J. Baschuk and X. Li, "Modelling of polymer electrolyte membrane fuel cells with variable degrees of water flooding," *Journal of power sources*, vol. 86, no. 1-2, pp. 181–196, 2000.

[16] N. Rajalakshmi, P. Sridhar, and K. Dhathathreyan, "Identification and characterization of parameters for external humidification used in polymer electrolyte membrane fuel cells," *Journal of Power Sources*, vol. 109, no. 2, pp. 452–457, 2002.

[17] D. Hyun and J. Kim, "Study of external humidification method in proton exchange membrane fuel cell," *Journal of Power Sources*, vol. 126, no. 1-2, pp. 98–103, 2004.

[18] S. Iyuke, A. Mohamad, and W. Daud, "Estimation of humidification load from humidifier column by convective heat transfer in water–air–vapour system," *Chemical engineering science*, vol. 56, no. 16, pp. 4949–4956, 2001.

[19] S. Yoshioka, A. Yoshimura, H. Fukumoto, O. Hiroi, and H. Yoshiyasu, "Development of a pefc under low humidified conditions," *Journal of power sources*, vol. 144, no. 1, pp. 146–151, 2005.

[20] S. Shimei and Z. Liqiu, "Study on feasibility of heat pipe technology for fuel cell thermal management system," in *2011 International Conference on Materials for Renewable Energy & Environment*, IEEE, vol. 1, 2011, pp. 717–720.

[21] N. Vanderborgh, J. Hedstrom, and J. Huff, "Thermal management of advanced fuel cell power systems," in *Intersociety Energy Conversion Engineering Conference*, 1990.

[22] A. Kirubakaran, S. Jain, and R. Nema, "A review on fuel cell technologies and power electronic interface," *Renewable and sustainable energy reviews*, vol. 13, no. 9, pp. 2430–2440, 2009.

[23] K. Agbossou, A. Bilodeau, and M. Doumbia, "Development of a control method for a renewable energy system with fuel cell," in *AFRICON 2009*, IEEE, 2009, pp. 1–5.

[24] T.-W. Lee, S.-H. Kim, Y.-H. Yoon, S.-J. Jang, and C.-Y. Won, "A 3 kw fuel cell generation system using the fuel cell simulator," in *2004 IEEE International Symposium on Industrial Electronics*, IEEE, vol. 2, 2004, pp. 833–837.

[25] N. Yousfi-Steiner, P. Moçotéguy, D. Candusso, D. Hissel, A. Hernandez, and A. Aslanides, "A review on pem voltage degradation associated with water management: Impacts, influent factors and characterization," *Journal of power sources*, vol. 183, no. 1, pp. 260–274, 2008.

[26] P. W. Voorhees, "The theory of ostwald ripening," *Journal of Statistical Physics*, vol. 38, no. 1, pp. 231–252, 1985.

[27] W. Bi, G. E. Gray, and T. F. Fuller, "Pem fuel cell pt/ c dissolution and deposition in nafion electrolyte," *Electrochemical and Solid-State Letters*, vol. 10, no. 5, B101, 2007.

[28] G. Chen, H. Zhang, H. Ma, and H. Zhong, "Electrochemical durability of gas diffusion layer under simulated proton exchange membrane fuel cell conditions," *international journal of hydrogen energy*, vol. 34, no. 19, pp. 8185–8192, 2009.

[29] F. De Bruijn, V. Dam, and G. Janssen, "Durability and degradation issues of pem fuel cell components," *Fuel cells*, vol. 8, no. 1, pp. 3–22, 2008.

[30] Z. Liu, Z. Mao, B. Wu, L. Wang, and V. M. Schmidt, "Current density distribution in pefc," *Journal of Power Sources*, vol. 141, no. 2, pp. 205–210, 2005.

[31] R. Eckl, R. Grinzinger, and W. Lehnert, "Current distribution mapping in polymer electrolyte fuel cells—a finite element analysis of measurement uncertainty imposed by lateral currents," *Journal of power sources*, vol. 154, no. 1, pp. 171–179, 2006.

[32] I. Alaefour, G. Karimi, K. Jiao, and X. Li, "Measurement of current distribution in a proton exchange membrane fuel cell with various flow arrangements–a parametric study," *Applied Energy*, vol. 93, pp. 80–89, 2012.

[33] R. Lin, Y. Weng, X. Lin, and F. Xiong, "Rapid cold start of proton exchange membrane fuel cells by the printed circuit board technology," *International journal of hydrogen energy*, vol. 39, no. 32, pp. 18 369–18 378, 2014.

[34] J. Shan, R. Lin, X. Chen, and X. Diao, "Eis and local resolved current density distribution analysis on effects of mpl on pemfc performance at varied humidification," *International Journal of Heat and Mass Transfer*, vol. 127, pp. 1076–1083, 2018.

[35] M. Heuer, P. A. Bernstein, M. Wenske, and Z. A. Styczynski, "Results of current density distribution mapping in pem fuel cells dependent on operation parameters," *Energies*, vol. 6, no. 8, pp. 3841–3858, 2013.

[36] T. Nasu, Y. Matsushita, J. Okano, and K. Okajima, "Study of current distribution in pemfc stack using magnetic sensor probe," *Journal of International Council on Electrical Engineering*, vol. 2, no. 4, pp. 391–396, 2012.

[37] K.-H. Hauer, R. Potthast, T. Wüster, and D. Stolten, "Magnetotomography—a new method for analysing fuel cell performance and quality," *Journal of Power Sources*, vol. 143, no. 1-2, pp. 67–74, 2005.

[38] R. Yamanashi, Y. Gotoh, M. Izumi, and T. Nara, "Evaluation of generation current inside membrane electrode assembly in polymer electrolyte fuel cell using static magnetic field around fuel cell," *ECS Transactions*, vol. 65, no. 1, p. 219, 2015.

[39] M. Izumi, Y. Gotoh, and T. Yamanaka, "Verification of measurement method of current distribution in polymer electrolyte fuel cells," *ECS Transactions*, vol. 17, no. 1, p. 401, 2009.

[40] L. Ifrek, G. Cauffet, O. Chadebec, Y. Bultel, S. Rosini, and L. Rouveyre, "2d and 3d fault basis for fuel cell diagnosis by external magnetic field measurements," *The European Physical Journal Applied Physics*, vol. 79, no. 2, p. 20 901, 2017.

[41] M. Le Ny, O. Chadebec, G. Cauffet, *et al.*, "Current distribution identification in fuel cell stacks from external magnetic field measurements," *IEEE transactions on magnetics*, vol. 49, no. 5, pp. 1925–1928, 2013.

[42] L. Ifrek, O. Chadebec, S. Rosini, G. Cauffet, Y. Bultel, and B. Bannwarth, "Fault identification on a fuel cell by 3-d current density reconstruction from external magnetic field measurements," *IEEE Transactions on Magnetics*, vol. 55, no. 6, pp. 1–5, 2019.

[43] M. Le Ny, O. Chadebec, G. Cauffet, S. Rosini, and Y. Bultel, "Pemfc stack diagnosis based on external magnetic field measurements," *Journal of Applied Electrochemistry*, vol. 45, no. 7, pp. 667–677, 2015.

[44] M. Le Ny, O. Chadebec, G. Cauffet, J.-M. Dedulle, and Y. Bultel, "A three dimensional electrical model of pemfc stack," *Fuel Cells*, vol. 12, no. 2, pp. 225–238, 2012.

[45] L. Ifrek, O. Chadebec, G. Cauffet, Y. Bultel, S. Rosini, and L. Rouveyre, "Spatial harmonic current density basis for faults identification in fuel cell stack from external magnetic field measurements," in *2017 International Applied Computational Electromagnetics Society Symposium-Italy (ACES)*, IEEE, 2017, pp. 1–2.

[46] Y.-G. Yoon, W.-Y. Lee, T.-H. Yang, G.-G. Park, and C.-S. Kim, "Current distribution in a single cell of pemfc," *Journal of Power Sources*, vol. 118, no. 1-2, pp. 193–199, 2003.

[47] X. Yuan, H. Wang, J. C. Sun, and J. Zhang, "Ac impedance technique in pem fuel cell diagnosis—a review," *International Journal of Hydrogen Energy*, vol. 32, no. 17, pp. 4365–4380, 2007.

[48] S. Wasterlain, D. Candusso, F. Harel, D. Hissel, and X. Francois, "Development of new test instruments and protocols for the diagnostic of fuel cell stacks," *Journal of Power Sources*, vol. 196, no. 12, pp. 5325–5333, 2011.

[49] A. Plait, S. Giurgea, D. Hissel, and C. Espanet, "New magnetic field analyzer device dedicated for polymer electrolyte fuel cells noninvasive diagnostic," *International Journal of Hydrogen Energy*, vol. 45, no. 27, pp. 14 071–14 082, 2020.

[50] G. Meunier, Y. Le Floch, and C. Guérin, "A nonlinear circuit coupled tt/sub 0/-/spl phi/formulation for solid conductors," *IEEE Transactions on Magnetics*, vol. 39, no. 3, pp. 1729–1732, 2003.

[51] H. Görgün, M. Arcak, and F. Barbir, "An algorithm for estimation of membrane water content in pem fuel cells," *Journal of power sources*, vol. 157, no. 1, pp. 389–394, 2006.

[52] F. H. DeLand, *Crc handbook of chemistry and physics: Rc west, mj astle, wh beyer, eds. boca raton, florida, crc press, inc., 1983, 2386 pp*, 1984.

[53] J. M. Coey, *Magnetism and magnetic materials*. Cambridge university press, 2010.

[54] S. Giurgea, R. Tirnovan, D. Hissel, and R. Outbib, "An analysis of fluidic voltage statistical correlation for a diagnosis of pem fuel cell flooding," *International Journal of Hydrogen Energy*, vol. 38, no. 11, pp. 4689–4696, 2013.

[55] R. Fisher, *Statistical methods for researcher workers; oliver and boyd: London, uk, 1925. 4. ranjit, kr design of experiments using the taguchi approach: 16 steps to product and process improvement*, 2001.

[56] E. Heaton and J. B. Robinson, *Heaton's Commercial Handbook of Canada...* Heaton Publishing Company, 1925, vol. 21.

[57] G. Taguchi, "Introduction to quality engineering: Designing quality into products and processes," Tech. Rep., 1986.

[58] Y.-W. Leung and Y. Wang, "An orthogonal genetic algorithm with quantization for global numerical optimization," *IEEE Transactions on Evolutionary computation*, vol. 5, no. 1, pp. 41–53, 2001.

[59] P. Xanthopoulos, P. M. Pardalos, and T. B. Trafalis, "Linear discriminant analysis," in *Robust data mining*, Springer, 2013, pp. 27–33.

[60] T. M. Cover, "Geometrical and statistical properties of systems of linear inequalities with applications in pattern recognition," *IEEE transactions on electronic computers*, no. 3, pp. 326–334, 1965.

[61] J. Platt, "Sequential minimal optimization: A fast algorithm for training support vector machines," 1998.

[62] S. Sun and R. Huang, "An adaptive k-nearest neighbor algorithm," in *2010 seventh international conference on fuzzy systems and knowledge discovery*, IEEE, vol. 1, 2010, pp. 91–94.

[63] L. Rokach and O. Maimon, "Decision trees," in *Data mining and knowledge discovery handbook*, Springer, 2005, pp. 165–192.

[64] *User guide flux 12.3 volume 3*, English, version Version 2.2.x, Altair Flux 2020, 10 pp., April 06, 2017.